Theory of topological superconductivity in doped IV-VI semiconductors

Zhe Li,[1,2] Shengshan Qin,[3,*] Jie Ren,[1,2] Zhida Song,[4] Dexi Shao,[1,5] and Chen Fang[1,6,3,†]

[1]*Beijing National Laboratory for Condensed Matter Physics and Institute of Physics, Chinese Academy of Sciences, Beijing 100190, China*
[2]*University of Chinese Academy of Sciences, Beijing 100049, China*
[3]*Kavli Institute for Theoretical Sciences, Chinese Academy of Sciences, Beijing 100190, China*
[4]*International Center for Quantum Materials, School of Physics, Peking University, Beijing 100871, China*
[5]*Department of Physics, Hangzhou Normal University, Hangzhou 311121, China*
[6]*Songshan Lake Materials Laboratory, Dongguan, Guangdong 523808, China*

(Received 11 January 2022; revised 18 March 2022; accepted 13 April 2022; published 22 April 2022)

We theoretically study potential unconventional superconductivity in doped *AB*-type IV-VI semiconductors, based on a minimal effective model with interaction up to the next-nearest neighbors. According to the experimental implications, we focus on the spin-triplet channels and obtain the superconducting phase diagram with respect to the anisotropy of the Fermi surfaces and the interaction strength. Abundant nodal and nodeless states with different symmetry breaking appear in the phase diagram, and all the states are time-reversal invariant and topologically nontrivial. Specifically, the various nodal superconducting ground states, dubbed as the topological Dirac superconductors, are featured by Dirac nodes in the bulk and Majorana arcs on the surface; among the full-gap states, there exist a mirror-symmetry-protected second-order topological superconductor state favoring helical Majorana hinge cones, and different first-order topological superconductor states supporting four surface Majorana cones. The experimental verification of the different kinds of superconducting ground states is also discussed.

DOI: 10.1103/PhysRevB.105.134517

I. INTRODUCTION

Since the discovery of topological insulators [1–3], the study of topological phases in condensed matter systems has been rapidly developing. After efforts of a decade, numerous novel topological phases have been proposed [4–7] and a large number of topological materials identified experimentally [8–21]. In recent years, topological superconductors (TSCs), which are the superconducting analogy of the topological insulators, have become the research frontier [22–38]. The TSCs are expected to host the Majorana modes which are believed to play an essential role in fault-tolerant topological quantum computing [39–41]. In the pursuit of topological superconductivity, one proposal is to introduce superconductivity into the surface Dirac cone of a topological insulator, such that each superconducting vortex is expected to bind a single Majorana zero mode [42]. Evidences for the vortex bound Majorana zero modes have been observed in the $Bi_2Te_3/NbSe_2$ heterostructure [29,43], β-Bi_2Pd [44], the transition metal dichalcogenide 2*M* WS_2 [45,46], and some iron-based superconductors [31,47–55].

In the above proposal the topological defect, i.e., the vortex, plays an essential role in realizing the Majorana modes, considering that the Majorana modes cannot appear in the absence of the vortex. Different from the vortex proposal, the Majorana modes exist on the natural physical boundary in the intrinsic TSCs. In the intrinsic TSCs, exotic pairing structures, such as the *p*-wave and $(p+ip)$-wave pairing on the Fermi surfaces, are vital. For instance, the Majorana modes were predicted to emerge at the ends of 1D *p*-wave SCs [56]; the chiral superconductivity and chiral Majorana modes have been discussed a lot in the heavy-fermion SCs [57–60] and the superconducting quantum Hall systems [61]; the Rashba semiconductors in proximity to conventional superconductors applied with an external magnetic field have also been predicted to host Majorana modes [62–65]. The recently discovered doped superconducting topological materials [6,66] provide another chance. Among them the most famous may be Bi_2Se_3 [67–70], which has been confirmed to be superconducting [71–75] when doped with Tm = Cu, Sr, Nb, Tl. Moreover, experimental measurements, such as thermodynamic [76], nuclear magnetic resonance [77], scanning tunneling microscopy [78] (STM), etc. [79–81], reveal that the superconductivity is nematic, suggesting $Tm_xBi_2Se_3$ (Tm = Cu, Sr, Nb) an odd-parity SC [82,83]. While further experimental evidences are still needed, the progress in $Tm_xBi_2Se_3$ stimulates more enthusiasms in the doped superconducting topological materials.

Here, we turn our attention to the *AB*-type IV-VI semiconductors, typified by SnTe which is well known as the first topological crystalline insulator [11,84]. Different from the topological insulators, even number of Dirac cones exist on the (001) surface in SnTe [84], which are protected by the mirror symmetry. With carrier doping, superconductivity has been confirmed in the series of materials experimentally [85,86]. Recent soft point-contact spectroscopy

*qinshengshan@iphy.ac.cn
†cfang@iphy.ac.cn

measurements reveal a sharp zero-bias peak in superconducting $Sn_{1-x}In_xTe$ [87]. High-resolution scanning tunneling microscopy provides more evidences for the gapless excitations on the surface of superconducting $Pb_{1-x}Sn_xTe$ [88]. These experiments indicate possible unconventional superconductivity in the doped IV-VI semiconductors.

In this paper, motivated by the experimental progress we perform a theoretical study on the superconductivity in underdoped *AB*-type IV-VI semiconductors. Our analyses are carried out based on an effective model capturing the Fermi surfaces in the strong spin-orbit coupling condition, and we consider the density-density interaction restricted up to the next-nearest neighbors. We first classify the superconducting orders according to the irreducible representations (irreps) of the symmetry group, i.e., the point group O_h. It turns out that the leading-order spin-singlet pairings are always topologically trivial without excitations in superconducting gaps. Therefore, we focus on the spin-triplet channels according to the experimental implications [87,88]. We obtain the superconducting phase diagram by calculating the free energy on the mean-field level, with respect to the anisotropy of the Fermi surfaces and different interaction strength. We find that the superconductivity belonging to the A_{1u}, A_{2u}, E_u, T_{1u}, and T_{2u} irreps can appear in different regions in the phase diagram. Among these states, the A_{1u} and A_{2u} channels keep the symmetry group O_h; for the ground states belonging to the high-dimensional irreps, there exist different kinds of symmetry breaking. The E_u channel is symmetry breaking from the cubic O_h group to the tetragonal D_{4h} group, the T_{2u} channel has two different ground states respecting the point group D_{4h} or D_{3d}, and the T_{1u} channel supports three different states with symmetry breaking to D_{4h}, D_{2h}, or D_{3d}. All these states are topologically nontrivial. Specifically, it is in a topological Dirac SC state with symmetry-protected nodal gap structures in the A_{2u} and T_{1u} states, and there exist Majorana arcs on the surfaces; while the A_{1u}, E_u, and T_{2u} (T_{2u} respecting the D_{3d} group) states are first-order topological superconductors favoring four surface Majorana cones; for the T_{2u} channel, there also exists a second-order TSC state (T_{2u} respecting the D_{4h} group) supporting helical Majorana hinge modes. The gapless surface or hinge modes and the point-group symmetry breaking can be detected in experiments, serving as signatures for the topological superconductivity in the series of materials.

II. MODEL AND METHOD

We start with a brief review of the crystal and electronic structures of the *AB*-type IV-VI materials. This series of materials crystallize in the rocksalt structure which respects the O_h point group together with translational symmetry of face-centered-cubic lattice as shown in Fig. 1(a) (space group No. 225). The corresponding first Brillouin zone (BZ) is a truncated octahedron, as shown in Fig. 1(b). In the BZ, there are four L points related by the C_4 rotational symmetry. At each L_n ($n = 1, 2, 3, 4$), the residual little group is D_{3d} which can be generated by the inversion symmetry, the C_3 rotation along the Γ-L direction and the mirror reflection parallel to the ΓZL_n plane. First-principle calculations show that the *AB*-type IV-VI materials are semiconductors

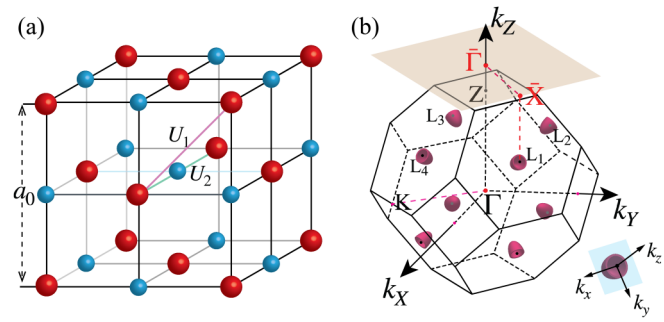

FIG. 1. (a) The lattice structure of the IV-VI semiconductors. The red and blue balls represent the A, B sublattices. U_1 and U_2 are the strength of the p-orbital density-density interaction between the nearest neighbors and next-nearest neighbors, respectively. a_0 is the lattice constant of the conventional unit cell. (b) The first BZ of the IV-VI semiconductors. Upon carrier doping, small Fermi surfaces (the claret shells) appear near the four L points which are related by C_4 rotation. The transparent brown plane represents the surface BZ on the (001) surface. Notice that $\bar{X}$ in the surface BZ is the projecting point of the L_1 and L_3 points in the bulk BZ. To describe the Fermi surfaces conveniently, aside from the global reference frame (k_X, k_Y, k_Z) we introduce a set of local reference frames at the four L points. We use (k_x, k_y, k_z) to denote the coordinates in the local reference frame at L_1, shown at the right bottom of the figure. The k_z axis goes along the Γ-L_1 direction and k_x goes along the Γ-K direction in the figure. The other three local reference frames can be obtained by taking C_4 rotation along the k_Z axis on the local reference frame at L_1.

with a narrow direct gap near the four L points. Around the gap, the conduction bands and the valence bands are contributed by the p orbitals of the A-type elements and B-type elements, and the ordering of the bands determines the topological property [84]. If the conduction band bottom (valence band top) is contributed by the B-type (A-type) element, the semiconductor is a topological crystalline insulator with even mirror Chern number; if the band ordering reverses, the semiconductor is topologically trivial. Upon carrier doping, four small Fermi pockets appear around the four L points, as sketched in Fig. 1(b), and superconductivity shows up below the transition temperature in the IV-VI semiconductors.

A. Normal-state Hamiltonian

We focus on the low-doping condition of the IV-VI semiconductors and give a general discussion on the normal bands at first. Since the four small Fermi surfaces are related by the C_4 rotation, for simplicity we can focus on the one located at L_1. Considering the symmetry constraints of the D_{3d} point group, the Fermi surface can be captured by a simple single-band model

$$H_0 = \sum_{\boldsymbol{k},s} \left(\frac{k_x^2 + k_y^2}{2m} + \frac{\xi k_z^2}{2m} - \mu \right) \hat{c}^\dagger_{\mathbf{k},s} \hat{c}_{\mathbf{k},s}, \tag{1}$$

where m is the effective mass and μ is the chemical potential, with $m, \mu > 0$ for the conduction bands and $m, \mu < 0$ for the valence bands. In the following analysis, it makes no difference for the conduction and valence bands, and we take

$m, \mu > 0$ for simplicity. The other symbols in Eq. (1) are explained as below. (i) k_x, k_y, and k_z are the momenta defined in the local reference frame at L_1, as shown in Fig. 1(b). (ii) Since the Fermi surface respects D_{3d} point-group symmetry, a parameter ξ has been introduced to characterize the anisotropy in different directions (based on the first-principle results, we estimate ξ for different kinds of IV-VI semiconductors and show it in Appendix A). (iii) The subscript $s = \uparrow, \downarrow$ labels angular momentum $j_z = \pm\frac{1}{2}$ defined according to the C_3 rotation along the Γ-L_1 direction rather than the real spin since the spin-orbit coupling in the IV-VI semiconductors cannot be neglected [84]. (iv) Although the single-band Hamiltonian cannot describe the nontrivial topology in the IV-VI semiconductors, it is a good approximation in the low-doping condition, considering that the orbital character on the Fermi surfaces is dominated by either the p orbitals of the A-type elements or the B-type elements.

B. Interaction

To generate superconductivity, we consider the density-density interaction between the p orbitals. In general, the interaction between different types of atoms needs to be taken into account. However, as mentioned above, in our consideration, i.e., the low-doping condition, the orbital characters on the Fermi surfaces are dominated by the p orbitals either from the A-type element or the B-type element, depending on whether the dopants are electrons or holes. Therefore, we can merely consider the interaction between the p orbitals in one sublattice in Fig. 1(a), and we restrict the interaction to the next-nearest neighbors

$$H_{\rm int} = U_0 \sum_i \hat{n}_i \hat{n}_i + \frac{U_1}{2} \sum_{\langle i,j\rangle} \hat{n}_i \hat{n}_j + \frac{U_2}{2} \sum_{\langle\langle i,j\rangle\rangle} \hat{n}_i \hat{n}_j, \quad (2)$$

where U_0, U_1, and U_2 are onsite, the nearest-neighbor, and the next-nearest-neighbor interactions, respectively, as indicated in Fig. 1(a). In the above equation, $\hat{n}_i$ is the density operator on the ith site defined as $\hat{n}_i = \sum_l \hat{n}_{i,l}$ with l denoting the freedom of spin and atomic orbitals, and $\langle ij\rangle$ and $\langle\langle ij\rangle\rangle$ denote the nearest neighbors and the next-nearest neighbors, respectively.

By doing a Fourier transformation, we can get the interacting Hamiltonian in the reciprocal space

$$H_{\rm int} = \sum_{\boldsymbol{q}} H_{\rm int}(\boldsymbol{q}) = \frac{1}{N} \sum_{\boldsymbol{q}} [U_0 + U_1 f_1(\boldsymbol{q}) + U_2 f_2(\boldsymbol{q})] \hat{n}_{\boldsymbol{q}} \hat{n}_{-\boldsymbol{q}}, \quad (3)$$

where N is the number of the sites in the system and $\hat{n}_{\boldsymbol{q}} = \sum_{\boldsymbol{K},l} \hat{\psi}_l^\dagger(\boldsymbol{K}+\boldsymbol{q})\hat{\psi}_l(\boldsymbol{K})$ and $f_\alpha(\boldsymbol{q}) = \sum_{\delta_\alpha} e^{i\boldsymbol{q}\cdot\delta_\alpha}$ with δ_α the bonds between the nearest (next-nearest) neighbors for $\alpha = 1$ ($\alpha = 2$). In the weak-coupling limit, only the interaction between electronic states on the Fermi surfaces is essential. Therefore, we restrict the momentum $\boldsymbol{K}$ and $\boldsymbol{K}+\boldsymbol{q}$ in the density operator within an area near the Fermi surfaces and have $\boldsymbol{K} = \mathbf{L}_n + \boldsymbol{k}$, $\boldsymbol{K}+\boldsymbol{q} = \mathbf{L}_m + \boldsymbol{k}'$, $|E_{\boldsymbol{k}} - \mu| < \delta\mu$, $|E_{\boldsymbol{k}'} - \mu| < \delta\mu$. In the above expression, $\mathbf{L}_m$ is the vector from the Γ point to L_m point, $E_{\boldsymbol{k}}$ is the kinetic energy of the states with momentum $\mathbf{L}_{1,2,3,4} + \boldsymbol{k}$, μ is the chemical potential, and $\delta\mu$ is the cutoff energy in the summation with $\delta\mu \ll \mu$. We can derive $|\boldsymbol{k}|, |\boldsymbol{k}'| \sim k_F \ll |\mathbf{L}_{1,2,3,4}|$ and $\boldsymbol{q} = \mathbf{L}_m - \mathbf{L}_n + \boldsymbol{k}' - \boldsymbol{k} = \mathbf{L}_{mn} + \tilde{\boldsymbol{q}}$, with $\mathbf{L}_{mn} = \mathbf{L}_m - \mathbf{L}_n$ and $\tilde{\boldsymbol{q}} \equiv \boldsymbol{k}' - \boldsymbol{k}$, $|\tilde{\boldsymbol{q}}| \ll |\mathbf{L}_{mn}|$. We substitute the relation $\hat{\psi}_l^\dagger(\boldsymbol{K}+\boldsymbol{q})\hat{\psi}_l(\boldsymbol{K}) = \hat{\psi}_l^\dagger(\boldsymbol{k}+\tilde{\boldsymbol{q}}+\mathbf{L}_m)\hat{\psi}_l(\boldsymbol{k}+\mathbf{L}_n)$ into Eq. (3) and obtain

TABLE I. The expansion of $f_i(\boldsymbol{q})$ in Eq. (3) at $\boldsymbol{q} = 0$ and $\boldsymbol{q} = L_{ij}$. $\tilde{\boldsymbol{q}}$ has the same magnitude as the Fermi momentum and it is small compared with L_{ij}, the vector from point L_i to L_j. We use $\tilde{q}_\parallel$ to denote the component of $\tilde{\boldsymbol{q}}$ parallel to $\boldsymbol{L}_{ij}$.

Coefficient function	Expansion
$f_1(\tilde{\boldsymbol{q}})$	$6 - \frac{1}{2}a_0^2\tilde{q}^2$
$f_2(\tilde{\boldsymbol{q}})$	$3 - \frac{1}{2}a_0^2\tilde{q}^2$
$f_1(\mathbf{L}_{mn}+\tilde{\boldsymbol{q}}), m \neq n$	$-2 + \frac{1}{2}a_0^2\tilde{q}_\parallel^2$
$f_2(\mathbf{L}_{mn}+\tilde{\boldsymbol{q}}), m \neq n$	$3 - \frac{1}{2}a_0^2\tilde{q}^2$

$$H_{\rm int} = \frac{1}{N} \sum_{\tilde{\boldsymbol{q}},m,n} [U_0 + U_1 f_1(\mathbf{L}_{mn}+\tilde{\boldsymbol{q}}) + U_2 f_2(\mathbf{L}_{mn}+\tilde{\boldsymbol{q}})] \hat{\rho}_{\tilde{\boldsymbol{q}},mn} \hat{\rho}_{-\tilde{\boldsymbol{q}},mn}. \quad (4)$$

In the above equation, $\hat{\rho}_{\tilde{\boldsymbol{q}},mn}$ is the newly defined density operator $\hat{\rho}_{\tilde{\boldsymbol{q}},mn} = \widetilde{\sum}_{\boldsymbol{k},l} \hat{\psi}_l^\dagger(\boldsymbol{k}+\tilde{\boldsymbol{q}}+\mathbf{L}_m)\hat{\psi}_l(\boldsymbol{k}+\mathbf{L}_n)$, where we use $\widetilde{\sum_{\boldsymbol{k}}}$ to denote the summation with a cutoff on the kinetic energy $E_{\boldsymbol{k}}$ and $E_{\boldsymbol{k}+\tilde{\boldsymbol{q}}}$. When $m = n$, the interaction is contributed by the electrons within the same Fermi surface, otherwise by the electrons from different Fermi surfaces. The coefficients $f_i(\mathbf{L}_{mn}+\tilde{\boldsymbol{q}})$ are calculated to the second order of $\tilde{\boldsymbol{q}}$ (details in Appendix C) and are listed in Table I.

To further simplify the interaction in Eq. (4) which includes all the p orbitals from atom A or B, we project the states $\hat{\psi}_l^\dagger(\boldsymbol{k}+\mathbf{L}_m)$ from the orbital basis to the band basis, and only the states on the Fermi surfaces will be preserved in the weak-coupling limit. We take the following three steps to accomplish such goal.

(i) In the low-doping limit, we use the wave functions at the L points to label the states on Fermi surfaces. In the above analysis, the orbital l in $\hat{\psi}_l(\boldsymbol{k}+\mathbf{L}_m)$ is defined in the global reference frame (the p orbitals are defined along the axis of the reference frame), where Z is taken along the [001] direction as shown in Fig. 1(b). In the following, for convenience, we adopt a set of local reference frames with the $L_{1,2,3,4}$ point as the origin, respectively. For instance, the local reference frame at L_1 is shown at the right bottom in Fig. 1(b). We take k_z along ΓL_1 and k_x along ΓX. The other three reference frames can be obtained by taking the C_4 rotation along k_Z on the one at L_1. We use $\hat{\phi}_{m,w}^\dagger(\boldsymbol{k})$ [$\hat{\phi}_{m,w}(\boldsymbol{k})$] to denote the creation (annihilation) operator in the mth local reference frame and the orbital w is defined in the local frame (k_x, k_y, k_z). The transformation from the global frame to the mth local frame can be accomplished by $\hat{U}_m$, $\hat{\psi}_l^\dagger(\boldsymbol{k}+\mathbf{L}_m) = \hat{U}_m\hat{\phi}_{m,l}^\dagger(\boldsymbol{k})\hat{U}_m^\dagger = \sum_w \mathcal{U}_{wl}^m \hat{\phi}_{m,w}^\dagger(\boldsymbol{k})$, and $\hat{\psi}_l(\boldsymbol{k}+\mathbf{L}_m) = \hat{U}_m\hat{\phi}_{m,l}(\boldsymbol{k})\hat{U}_m^\dagger = \sum_w \mathcal{U}_{wl}^{m*}\hat{\phi}_{m,w}(\boldsymbol{k})$, where $\mathcal{U}^m$ is the transformation matrix. We derive the density operator under the new basis as

$$\hat{\rho}_{\tilde{\boldsymbol{q}},mn} = \widetilde{\sum_{\boldsymbol{k},l}} \hat{\psi}_l^\dagger(\boldsymbol{k}+\tilde{\boldsymbol{q}}+\mathbf{L}_m)\hat{\psi}_l(\boldsymbol{k}+\mathbf{L}_n) = \widetilde{\sum_{\boldsymbol{k},l}} \hat{U}_m\hat{\phi}_{m,l}^\dagger(\boldsymbol{k}+\tilde{\boldsymbol{q}})\hat{U}_m^\dagger\hat{U}_n\hat{\phi}_{n,l}(\boldsymbol{k})\hat{U}_n^\dagger$$

TABLE II. Relations between the orbital basis and the basis labeled by angular momentum. All the states are defined in the local reference frame.

Angular momentum	Atomic orbitals and spin
$\|J=\frac{1}{2}, j_z=\frac{1}{2}\rangle$	$-\frac{1}{\sqrt{3}}\|p_z,\uparrow\rangle-\frac{1}{\sqrt{3}}\|p_x,\downarrow\rangle-\frac{i}{\sqrt{3}}\|p_y,\downarrow\rangle$
$\|J=\frac{3}{2}, j_z=\frac{1}{2}\rangle$	$\sqrt{\frac{2}{3}}\|p_z,\uparrow\rangle-\frac{1}{\sqrt{6}}\|p_x,\downarrow\rangle-\frac{i}{\sqrt{6}}\|p_y,\downarrow\rangle$
$\|J=\frac{1}{2}, j_z=-\frac{1}{2}\rangle$	$\frac{1}{\sqrt{3}}\|p_z,\downarrow\rangle-\frac{1}{\sqrt{3}}\|p_x,\uparrow\rangle+\frac{i}{\sqrt{3}}\|p_y,\uparrow\rangle$
$\|J=\frac{3}{2}, j_z=-\frac{1}{2}\rangle$	$\sqrt{\frac{2}{3}}\|p_z,\downarrow\rangle+\frac{1}{\sqrt{6}}\|p_x,\uparrow\rangle-\frac{i}{\sqrt{6}}\|p_y,\uparrow\rangle$

TABLE III. The projection from the orbital basis to the band basis at the L points. We list the orbital in the left column and its projection on the bands near the Fermi energy in the right column.

Original basis	After projection
$\|p_x,\uparrow\rangle$	$[\frac{1}{\sqrt{3}}\cos(\frac{\theta}{2})+\frac{1}{\sqrt{6}}\sin(\frac{\theta}{2})]\|j_z=-\frac{1}{2}\rangle_2$
$\|p_y,\uparrow\rangle$	$-i[\frac{1}{\sqrt{3}}\cos(\frac{\theta}{2})+\frac{1}{\sqrt{6}}\sin(\frac{\theta}{2})]\|j_z=-\frac{1}{2}\rangle_2$
$\|p_z,\uparrow\rangle$	$[\sqrt{\frac{2}{3}}\sin(\frac{\theta}{2})-\frac{1}{\sqrt{3}}\cos(\frac{\theta}{2})]\|j_z=\frac{1}{2}\rangle_2$
$\|p_x,\downarrow\rangle$	$-[\frac{1}{\sqrt{3}}\cos(\frac{\theta}{2})+\frac{1}{\sqrt{6}}\sin(\frac{\theta}{2})]\|j_z=\frac{1}{2}\rangle_2$
$\|p_y,\downarrow\rangle$	$-i[\frac{1}{\sqrt{3}}\cos(\frac{\theta}{2})+\frac{1}{\sqrt{6}}\sin(\frac{\theta}{2})]\|j_z=\frac{1}{2}\rangle_2$
$\|p_z,\downarrow\rangle$	$[\sqrt{\frac{2}{3}}\sin(\frac{\theta}{2})-\frac{1}{\sqrt{3}}\cos(\frac{\theta}{2})]\|j_z=-\frac{1}{2}\rangle_2$

$$= \widetilde{\sum_{\boldsymbol{k},l,w,v}} \mathcal{U}^{m}_{wl}\mathcal{U}^{n*}_{vl}\hat{\phi}^{\dagger}_{m,w}(\boldsymbol{k}+\tilde{\boldsymbol{q}})\hat{\phi}_{n,v}(\boldsymbol{k})$$
$$= \widetilde{\sum_{\boldsymbol{k},w,v}} \mathcal{D}^{mn}_{wv}\hat{\phi}^{\dagger}_{m,w}(\boldsymbol{k}+\tilde{\boldsymbol{q}})\hat{\phi}_{n,v}(\boldsymbol{k}). \quad (5)$$

In Eq. (5), $\mathcal{D}^{mn}=\mathcal{U}^{m}\mathcal{U}^{n\dagger}$ is an identity matrix for the intrapocket interaction, i.e., $m=n$; and the matrix form of $\mathcal{D}^{mn}$ for the interpocket interaction ($m\neq n$) is presented in Appendix D.

(ii) The first-principle calculation shows that the bands near the Fermi level are contributed by the states with the angular momentum $j_z=\pm\frac{1}{2}$ with j_z defined according to the rotation along ΓL [84]. Therefore, we transform the orbital basis $|p_{x,y,z},\uparrow(\downarrow)\rangle$ in the local reference frames to $|J,j_z\rangle$, and the results are shown in Table II. Here, we only preserve the states with $j_z=\pm\frac{1}{2}$.

(iii) As SO(3) symmetry is not respected in the real system, J is not a good quantum number, and the states at the L points must be the mix between $|J=\frac{1}{2},j_z=\pm\frac{1}{2}\rangle$ and $|J=\frac{3}{2},j_z=\pm\frac{1}{2}\rangle$. Moreover, at the L points the effective Hamiltonian describing the hybridization between these states takes the following form:

$$H_{\rm mix}=h_0\cos\theta\sigma_0\tau_3+h_0\sin\theta\sigma_3\tau_1, \quad (6)$$

where the Pauli matrices σ and τ act on the basis of j_z $\{j_z=\frac{1}{2},j_z=-\frac{1}{2}\}$ and J $\{J=\frac{1}{2},J=\frac{3}{2}\}$, respectively. In the above Hamiltonian, $h_0\cos\theta$ depicts the energy split between the states with $J=\frac{1}{2},J=\frac{3}{2}$, and $h_0\sin\theta$ is their hybridization arising from the crystal field, with θ a dimensionless parameter and h_0 the coefficient with the dimension of energy. Based on the first-principle results, we estimate θ for different kinds of IV-VI semiconductors and show it in Appendix A. We obtain four eigenstates by diagonalizing $H_{\rm mix}$ and list in the following:

$$\left|j_z=\frac{1}{2}\right\rangle_1=\left(-\sin\frac{\theta}{2},\cos\frac{\theta}{2},0,0\right)^{\intercal},$$
$$\left|j_z=\frac{1}{2}\right\rangle_2=\left(\cos\frac{\theta}{2},\sin\frac{\theta}{2},0,0\right)^{\intercal},$$
$$\left|j_z=-\frac{1}{2}\right\rangle_1=\left(0,0,\sin\frac{\theta}{2},\cos\frac{\theta}{2}\right)^{\intercal},$$
$$\left|j_z=-\frac{1}{2}\right\rangle_2=\left(0,0,-\cos\frac{\theta}{2},\sin\frac{\theta}{2}\right)^{\intercal}. \quad (7)$$

Here, we consider the states with the lower energy, i.e., $|j_z=\pm\frac{1}{2}\rangle_2$, which is near the Fermi energy in the conduction bands.

At last, we project the states $\hat{\phi}^{\dagger}_{w}(\boldsymbol{k})|0\rangle$ in each local reference frame onto $|j_z=\pm\frac{1}{2}\rangle_2$ for the corresponding Fermi surface based on the results in Table II and Eq. (7), and the final results are listed in Table III.

C. Mean-field superconducting orders

So far, we have projected the orbital basis in the global reference frame to the band basis (more details in Appendix D). We use $\hat{c}^{m\dagger}_{\boldsymbol{k},\uparrow(\downarrow)}$ to denote the creation operator for $|j_z=\frac{1}{2}\rangle_2$ ($|j_z=-\frac{1}{2}\rangle_2$) on the mth Fermi surface and $\hat{c}^{m}_{\boldsymbol{k},\uparrow(\downarrow)}$ to denote the annihilation operator. For superconductivity, the pairing occurs between the states on the same Fermi surface with opposite momentum. Therefore, we project the interaction in Eq. (4) onto the Fermi surfaces and in the superconducting channel it becomes

$$H_{\rm int}=\sum_{m,n}\sum_{d_1,d_2,g_1,g_2}\widetilde{\sum_{\boldsymbol{k}_1,\boldsymbol{k}_2}} f'_{d_1d_2g_1g_2}(\mathbf{L}_{mn}+\boldsymbol{k}_1-\boldsymbol{k}_2)\hat{c}^{m\dagger}_{\boldsymbol{k}_1,d_1}\hat{c}^{m\dagger}_{-\boldsymbol{k}_1,d_2}\hat{c}^{n}_{-\boldsymbol{k}_2,g_2}\hat{c}^{n}_{\boldsymbol{k}_2,g_1}+\text{non-SC}, \quad (8)$$

where $d_{1(2)}$ and $g_{1(2)}$ indicate pseudospin indices with the up and down directions defined along its own k_z direction in the local frame in Fig. 2(b) for each of the four Fermi pockets, and $f'_{s_1s_2}$ is the interaction strength between the four Fermi pockets. In our approximation, $f'_{d_1d_2g_1g_2}(\mathbf{L}_{mn}+\boldsymbol{k}_1-\boldsymbol{k}_2)$ is expanded to the second order of $\boldsymbol{k}_1-\boldsymbol{k}_2$. As a result, the interaction can be

rewritten as

$$H_{\rm int}=\sum_{m,n}\sum_{d_1,d_2,g_1,g_2}\widetilde{\sum_{\boldsymbol{k}_1,\boldsymbol{k}_2}}\left(g^{0,mn}_{d_1d_2g_1g_2}+g^{2,mn}_{d_1d_2g_1g_2}\left(k_1^2+k_2^2-2\boldsymbol{k}_1\cdot\boldsymbol{k}_2\right)\right)\hat{c}^{m\dagger}_{\boldsymbol{k}_1,d_1}\hat{c}^{m\dagger}_{-\boldsymbol{k}_1,d_2}\hat{c}^{n}_{-\boldsymbol{k}_2,g_2}\hat{c}^{n}_{\boldsymbol{k}_2,g_1}, \tag{9}$$

where $g^{0(2),mn}_{d_1d_2g_1g_2}$ is the expanding coefficient to the zeroth (second) order of $f'_{d_1d_2g_1g_2}(\mathbf{L}_{mn}+\boldsymbol{k}_1-\boldsymbol{k}_2)$ in Eq. (8) at $k_1-k_2=0$. $\hat{c}^{m\dagger}_{\boldsymbol{k},d_1}\hat{c}^{m\dagger}_{-\boldsymbol{k},d_2}$, $k_{x(y,z)}\hat{c}^{m\dagger}_{\boldsymbol{k},d_1}\hat{c}^{m\dagger}_{-\boldsymbol{k},d_2}$, and $k^2\hat{c}^{m\dagger}_{\boldsymbol{k},d_1}\hat{c}^{m\dagger}_{-\boldsymbol{k},d_2}$ can be decomposed according to the irreps basis of the D_{3d} group. We list the irreps basis $\hat{\delta}_i(\boldsymbol{k})$ in the zeroth and first order of $\boldsymbol{k}$ in Table IV. The irrep bases from different pockets take the same form if we use the local reference frame defined at each pocket, and we suppress the superscript m in $\hat{c}^{m}_{\boldsymbol{k},\uparrow(\downarrow)}$ to indicate any of the four pockets. The pairing in the second order of $\boldsymbol{k}$ is not in consideration (we discuss it in the later calculations). The C_4 rotation relates different Fermi pockets to each other and induces the symmetry group from point group D_{3d} to O_h. The detailed procedure of the inducing is shown in Appendix E. The basis obtained from the direct summation of the D_{3d} irreps basis $\hat{\delta}_i(\boldsymbol{k})$ on the four pockets is always reducible in the group O_h. However, we can decompose the reducible representation to the irreps of group O_h and obtain the irreps basis of O_h composed of $\hat{\delta}_i(\boldsymbol{k})$ defined on the four pockets (details in Appendix E). We use $\hat{\delta}_i(m,\boldsymbol{k})$ to represent $\hat{\delta}_i(\boldsymbol{k})$ on the mth pocket and list the induced irreps basis of the group O_h in Table V. Based on the results in Tables IV and V, we can decompose $\hat{c}^{m\dagger}_{\boldsymbol{k},d_1}\hat{c}^{m\dagger}_{-\boldsymbol{k},d_2}$, $k_{x(y,z)}\hat{c}^{m\dagger}_{\boldsymbol{k},d_1}\hat{c}^{m\dagger}_{-\boldsymbol{k},d_2}$, and $k^2\hat{c}^{m\dagger}_{\boldsymbol{k},d_1}\hat{c}^{m\dagger}_{-\boldsymbol{k},d_2}$ according to the irreps basis of the group O_h and the interaction turns out to be

$$H_{\rm int}=\sum_{\epsilon,\kappa,\zeta,\boldsymbol{k},\boldsymbol{k}'}\frac{1}{N}\tilde{f}^{\epsilon}_{\kappa}(U_0,U_1,U_2,\theta)\hat{\Delta}^{\epsilon}_{\kappa,\zeta}(\boldsymbol{k})^{\dagger}\hat{\Delta}^{\epsilon}_{\kappa,\zeta}(\boldsymbol{k}')+\text{non-SC}, \tag{10}$$

where $\tilde{f}^{\epsilon}_{\kappa}(U_0,U_1,U_2,\theta)$ is the coefficient. In the equation, ϵ represents the symmetry of the irreps with $\epsilon=A_{1g(u)}$, $A_{2g(u)}$, $E_{g(u)}$, $T_{1g(u)}$, and $T_{2g(u)}$, κ stands for the κth basis in irreps ϵ, and ζ means the ζth component in a given basis. For instance, for $\epsilon=T_u$ we have $\kappa=1,2$ and $\zeta=1,2,3$ (in Table V, there are two different T_{2u} and the T_{2u} representation is three dimensional, i.e., each T_{2u} has three components). We assume the strength of the onsite interaction is much bigger than the other two, $|U_0|\gg|U_1|,|U_2|$. When U_0 is negative, the ground state is the BCS type which is topologically trivial. When U_0 is positive, the irreps with even parity cannot be the ground states (details in Appendix F). Therefore, in the following we set $U_0>0$ and only focus on the odd-parity superconductivity induced by U_1 and U_2. We have in total 15 channels in 5 pairing symmetries: $2A_{1u}$, $1A_{2u}$, $3E_u$, $4T_{1u}$, and $5T_{2u}$. After taking the mean-field approximation $\sum_{\boldsymbol{k}}\frac{1}{N}\langle\tilde{f}^{\epsilon}_{\kappa}(U_0,U_1,U_2,\theta)\hat{\Delta}^{\epsilon}_{\kappa,\zeta}(\boldsymbol{k})^{\dagger}\rangle=\lambda^{\epsilon}_{\kappa,\zeta}$, we obtain the following Hamiltonian:

$$H_{\rm BdG}=H_0+\sum_{\epsilon,\kappa,\zeta,\boldsymbol{k}}\left(\lambda^{\epsilon}_{\kappa,\zeta}\hat{\Delta}^{\epsilon}_{\kappa,\zeta}(\boldsymbol{k})+\lambda^{\epsilon*}_{\kappa,\zeta}\hat{\Delta}^{\epsilon}_{\kappa,\zeta}(\boldsymbol{k})^{\dagger}-\frac{N\left|\lambda^{\epsilon}_{\kappa,\zeta}\right|^2}{\tilde{f}^{\epsilon}_{\kappa}(U_0,U_1,U_2,\theta)}\right)+\text{non-SC}, \tag{11}$$

where H_0 is the normal-state Hamiltonian in Eq. (1). Then, we calculate the free energy for each of the irreps (details in Appendix G) and obtain the superconducting ground states.

TABLE IV. The irreps basis of group D_{3d}. We use $\hat{\delta}_i(\boldsymbol{k})$ to represent the notation for the irreps basis of group D_{3d}. To simplify the expression, $\uparrow$ and $\downarrow$ stand no longer for the real spin defined above, but for the pseudospin $|j_z=\frac{1}{2}\rangle_2$ and $|j_z=-\frac{1}{2}\rangle_2$ in Eq. (7). The symmetry of each basis is listed in the right column. For $i=1,2,3,4$, the irreps are one dimensional and only have one component; while for $i=5,6,7$, the e_u irrep is two dimensional and we use $\hat{\delta}_{i,1(2)}(\boldsymbol{k})$ to denote the first (second) component of the basis.

	Irreps basis	Symmetry
$\hat{\delta}_1(\boldsymbol{k})$	$\frac{\sqrt{2}}{2}(\hat{c}_{\boldsymbol{k},\uparrow}\hat{c}_{-\boldsymbol{k},\downarrow}-\hat{c}_{\boldsymbol{k},\downarrow}\hat{c}_{-\boldsymbol{k},\uparrow})$	a_{1g}
$\hat{\delta}_2(\boldsymbol{k})$	$\frac{\sqrt{2}}{2}k_z(\hat{c}_{\boldsymbol{k},\uparrow}\hat{c}_{-\boldsymbol{k},\downarrow}+\hat{c}_{\boldsymbol{k},\downarrow}\hat{c}_{-\boldsymbol{k},\uparrow})$	a_{1u}
$\hat{\delta}_3(\boldsymbol{k})$	$\frac{1}{2}[(ik_x+k_y)\hat{c}_{\boldsymbol{k},\uparrow}\hat{c}_{-\boldsymbol{k},\uparrow}+(-ik_x+k_y)\hat{c}_{\boldsymbol{k},\downarrow}\hat{c}_{-\boldsymbol{k},\downarrow}]$	a_{1u}
$\hat{\delta}_4(\boldsymbol{k})$	$\frac{1}{2}[(ik_x+k_y)\hat{c}_{\boldsymbol{k},\uparrow}\hat{c}_{-\boldsymbol{k},\uparrow}-(-ik_x+k_y)\hat{c}_{\boldsymbol{k},\downarrow}\hat{c}_{-\boldsymbol{k},\downarrow}]$	a_{2u}
$\hat{\delta}_{5,1}(\boldsymbol{k})$	$\frac{\sqrt{2}}{2}(ik_x+k_y)\hat{c}_{\boldsymbol{k},\downarrow}\hat{c}_{-\boldsymbol{k},\downarrow}$	e_u
$\hat{\delta}_{5,2}(\boldsymbol{k})$	$\frac{\sqrt{2}}{2}(-ik_x+k_y)\hat{c}_{\boldsymbol{k},\uparrow}\hat{c}_{-\boldsymbol{k},\uparrow}$	
$\hat{\delta}_{6,1}(\boldsymbol{k})$	$k_z\hat{c}_{\boldsymbol{k},\downarrow}\hat{c}_{-\boldsymbol{k},\downarrow}$	e_u
$\hat{\delta}_{6,2}(\boldsymbol{k})$	$k_z\hat{c}_{\boldsymbol{k},\uparrow}\hat{c}_{-\boldsymbol{k},\uparrow}$	
$\hat{\delta}_{7,1}(\boldsymbol{k})$	$\frac{1}{2}(-ik_x+k_y)(\hat{c}_{\boldsymbol{k},\uparrow}\hat{c}_{-\boldsymbol{k},\downarrow}+\hat{c}_{\boldsymbol{k},\downarrow}\hat{c}_{-\boldsymbol{k},\uparrow})$	e_u
$\hat{\delta}_{7,2}(\boldsymbol{k})$	$\frac{1}{2}(-ik_x+k_y)(\hat{c}_{\boldsymbol{k},\uparrow}\hat{c}_{-\boldsymbol{k},\downarrow}+\hat{c}_{\boldsymbol{k},\downarrow}\hat{c}_{-\boldsymbol{k},\uparrow})$	

III. RESULTS

As shown in the former section, for each pairing symmetry there can be multiple linearly independent channels for the Cooper pairs. For example, there are three E_u channels and five T_{2u} channels, as shown in Table V. For channels of higher than one-dimensional irreps, there are multiple components in each channel. If a pairing symmetry ϵ has κ channels and each channel is a ζ-dimensional irrep, we need a complex vector $(r^{\epsilon}_1,\ldots,r^{\epsilon}_{\kappa})\otimes(t^{\epsilon}_1,\ldots,t^{\epsilon}_{\zeta})$ to describe the superconducting ground states. For instance, the E_u state can be described as $(r^{E_u}_1,r^{E_u}_2,r^{E_u}_3)\otimes(t^{E_u}_1,t^{E_u}_2)$ in general. Obviously, the above vector satisfies $r^{\epsilon}_{\kappa}t^{\epsilon}_{\zeta}=\lambda^{\epsilon}_{\kappa,\zeta}$ with $\lambda^{\epsilon}_{\kappa,\zeta}$ being the coefficients in Eq. (11) for irrep ϵ. By calculating and minimizing the mean-field free energy, which is shown in detail in Appendix G, we can get the irrep and the corresponding coefficients $\mathbf{r}$ and $\mathbf{t}$ for the superconducting ground states. The topological properties of the ground states can be analyzed accordingly.

TABLE V. The irreps of the O_h group denoted as A_{1u}, A_{2u}, E_u, T_{1u}, and T_{2u} are induced from the irreps of the D_{3d} group a_{1u}, a_{2u}, and e_u. Here, we use $\hat{\delta}_i(j,\boldsymbol{k})$ to label the irreps basis $\hat{\delta}_i(\boldsymbol{k})$ of group D_{3d} on the jth Fermi pocket, whose forms in their corresponding local reference frames are all the same and are listed in Table IV.

Irreps of O_h	Induced from	Combination of irreps of D_{3d}	
A_{1u}	a_{1u}	$\frac{1}{2}(\hat{\delta}_i(1,\boldsymbol{k})+\hat{\delta}_i(2,\boldsymbol{k})+\hat{\delta}_i(3,\boldsymbol{k})+\hat{\delta}_i(4,\boldsymbol{k}))$	$i=2,3$
T_{2u}		$\frac{1}{2}(\hat{\delta}_i(1,\boldsymbol{k})-\hat{\delta}_i(2,\boldsymbol{k})-\hat{\delta}_i(3,\boldsymbol{k})+\hat{\delta}_i(4,\boldsymbol{k}))$	
		$\frac{1}{2}(\hat{\delta}_i(1,\boldsymbol{k})+\hat{\delta}_i(2,\boldsymbol{k})-\hat{\delta}_i(3,\boldsymbol{k})-\hat{\delta}_i(4,\boldsymbol{k}))$	
		$\frac{1}{2}(\hat{\delta}_i(1,\boldsymbol{k})-\hat{\delta}_i(2,\boldsymbol{k})+\hat{\delta}_i(3,\boldsymbol{k})-\hat{\delta}_i(4,\boldsymbol{k}))$	
A_{2u}	a_{2u}	$\frac{1}{2}(\hat{\delta}_i(1,\boldsymbol{k})-\hat{\delta}_i(2,\boldsymbol{k})+\hat{\delta}_i(3,\boldsymbol{k})-\hat{\delta}_i(4,\boldsymbol{k}))$	$i=4$
T_{1u}		$\frac{1}{2}(\hat{\delta}_i(1,\boldsymbol{k})-\hat{\delta}_i(2,\boldsymbol{k})-\hat{\delta}_i(3,\boldsymbol{k})+\hat{\delta}_i(4,\boldsymbol{k}))$	
		$\frac{1}{2}(\hat{\delta}_i(1,\boldsymbol{k})+\hat{\delta}_i(2,\boldsymbol{k})-\hat{\delta}_i(3,\boldsymbol{k})-\hat{\delta}_i(4,\boldsymbol{k}))$	
		$\frac{1}{2}(\hat{\delta}_i(1,\boldsymbol{k})+\hat{\delta}_i(2,\boldsymbol{k})+\hat{\delta}_i(3,\boldsymbol{k})+\hat{\delta}_i(4,\boldsymbol{k}))$	
E_u	e_u	$\frac{1}{2}(\hat{\delta}_{i,1}(1,\boldsymbol{k})+\hat{\delta}_{i,1}(2,\boldsymbol{k})+\hat{\delta}_{i,1}(3,\boldsymbol{k})+\hat{\delta}_{i,1}(4,\boldsymbol{k}))$	$i=5,6,7$
		$\frac{1}{2}(\hat{\delta}_{i,2}(1,\boldsymbol{k})-\hat{\delta}_{i,2}(2,\boldsymbol{k})+\hat{\delta}_{i,2}(3,\boldsymbol{k})-\hat{\delta}_{i,2}(4,\boldsymbol{k}))$	
T_{1u}		$\frac{\sqrt{3}}{4}(\hat{\delta}_{i,1}(1,\boldsymbol{k})+\hat{\delta}_{i,1}(2,\boldsymbol{k})-\hat{\delta}_{i,1}(3,\boldsymbol{k})-\hat{\delta}_{i,1}(4,\boldsymbol{k}))+\frac{1}{4}(\hat{\delta}_{i,2}(1,\boldsymbol{k})-\hat{\delta}_{i,2}(2,\boldsymbol{k})-\hat{\delta}_{i,2}(3,\boldsymbol{k})+\hat{\delta}_{i,2}(4,\boldsymbol{k}))$	
		$\frac{\sqrt{3}}{4}(-\hat{\delta}_{i,1}(1,\boldsymbol{k})+\hat{\delta}_{i,1}(2,\boldsymbol{k})+\hat{\delta}_{i,1}(3,\boldsymbol{k})-\hat{\delta}_{i,1}(4,\boldsymbol{k}))+\frac{1}{4}(\hat{\delta}_{i,2}(1,\boldsymbol{k})+\hat{\delta}_{i,2}(2,\boldsymbol{k})-\hat{\delta}_{i,2}(3,\boldsymbol{k})-\hat{\delta}_{i,2}(4,\boldsymbol{k}))$	
		$-\frac{1}{2}(\hat{\delta}_{i,2}(1,\boldsymbol{k})+\hat{\delta}_{i,2}(2,\boldsymbol{k})+\hat{\delta}_{i,2}(3,\boldsymbol{k})+\hat{\delta}_{i,2}(4,\boldsymbol{k}))$	
T_{2u}		$\frac{1}{4}(\hat{\delta}_{i,1}(1,\boldsymbol{k})-\hat{\delta}_{i,1}(2,\boldsymbol{k})-\hat{\delta}_{i,1}(3,\boldsymbol{k})+\hat{\delta}_{i,1}(4,\boldsymbol{k}))+\frac{\sqrt{3}}{4}(\hat{\delta}_{i,2}(1,\boldsymbol{k})+\hat{\delta}_{i,2}(2,\boldsymbol{k})-\hat{\delta}_{i,2}(3,\boldsymbol{k})-\hat{\delta}_{i,2}(4,\boldsymbol{k}))$	
		$\frac{\sqrt{3}}{4}(\hat{\delta}_{i,1}(1,\boldsymbol{k})+\hat{\delta}_{i,1}(2,\boldsymbol{k})-\hat{\delta}_{i,1}(3,\boldsymbol{k})-\hat{\delta}_{i,1}(4,\boldsymbol{k}))+\frac{1}{4}(-\hat{\delta}_{i,2}(1,\boldsymbol{k})+\hat{\delta}_{i,2}(2,\boldsymbol{k})+\hat{\delta}_{i,2}(3,\boldsymbol{k})-\hat{\delta}_{i,2}(4,\boldsymbol{k}))$	
		$\frac{1}{2}(-\hat{\delta}_{i,2}(1,\boldsymbol{k})+\hat{\delta}_{i,2}(2,\boldsymbol{k})-\hat{\delta}_{i,2}(3,\boldsymbol{k})+\hat{\delta}_{i,2}(4,\boldsymbol{k}))$	

A. Phase diagrams

We study the ground states with respect to the Fermi-surface anisotropy ξ introduced in Eq. (1) and the nearest- and next-nearest-neighbor interaction U_1, U_2 in Eq. (2). In the calculation, we parametrize U_1, U_2 as $U_1 = V\sin\phi$ and $U_2 = V\cos\phi$. For other parameters, we set $m = 0.5$, $\mu = 16$, and $V = 1.0$, and focus on the two conditions with $\theta = -0.08\pi$ and $\theta = -0.66\pi$ with θ defined in Eq. (6) (a more systematic study is presented in Appendix B). Notice that if both U_1 and U_2 are repulsive, i.e., $0 < \phi < \pi/2$, superconductivity will not be favored in the mean-field level, as shown in the phase diagram in Fig. 2.

1. $\theta = -0.08\pi$

In the $\theta = -0.08\pi$ scenario, according to Eq. (7) the electronic states on the Fermi surfaces are mainly contributed by $|J=\frac{1}{2}, j_z=\pm\frac{1}{2}\rangle$ in Table II whose wave function is nearly isotropic with respect to the p_x, p_y, and p_z orbitals. The corresponding phase diagram is shown in Fig. 2(a), where there exist the A_{1u}, A_{2u}, E_u, and T_{2u} states. The E_u state is characterized by a vector $(r_1^{E_u}, r_2^{E_u}, r_3^{E_u})\otimes(1,0)$, and there are two different T_{2u} states including $T_{2u,[001]}$ and $T_{2u,[111]}$, which are featured by $(r_1^{T_{2u}}, r_2^{T_{2u}}, r_3^{T_{2u}}, r_4^{T_{2u}}, r_5^{T_{2u}})\otimes(0,0,1)$ and $(r_1^{T_{2u}}, r_2^{T_{2u}}, r_3^{T_{2u}}, r_4^{T_{2u}}, r_5^{T_{2u}})\otimes(1,1,1)$, respectively. Among the ground states in the phase diagram, the A_{2u} state is nodal, and the other states are fully gapped. We present the corresponding superconducting gap structures obtained from numerical calculations in Figs. 3 and 6. It can be noticed that both the A_{1u} and A_{2u} states respect all the symmetries in the point group O_h, the E_u and $T_{2u,[001]}$ states break the threefold rotational symmetry along the Γ-L direction and preserve the D_{4h} point group, and the $T_{2u,[111]}$ state only respects the D_{3d} symmetry group with the main rotation axis along the Γ-L direction. This symmetry-breaking information can be read out from Table VI: for instance, on the E_u row only operations that are diagonal can preserve $\mathbf{t} = (1,0)$, thus remaining symmetries in the ordered phase.

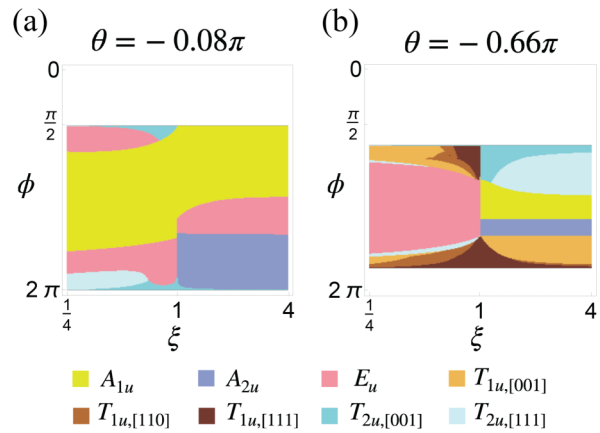

FIG. 2. Phase diagrams for the Hamiltonian in Eq. (11). The left (right) corresponds to the $\theta = -0.08\pi$ ($\theta = -0.66\pi$) condition.

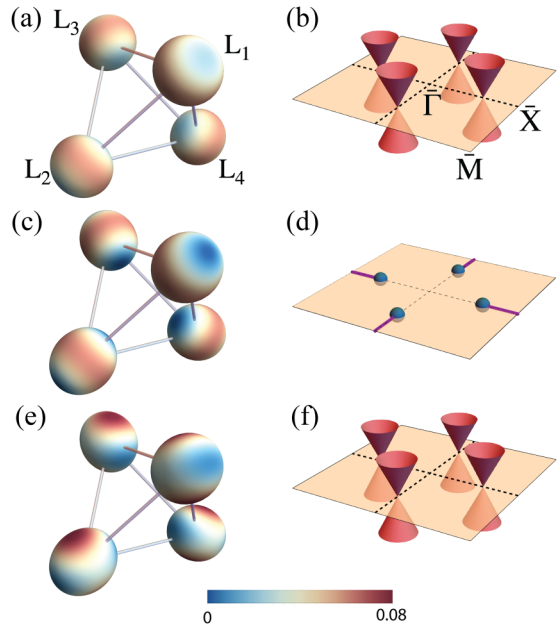

FIG. 3. (a), (c), (e) Show the superconducting gap on the Fermi surfaces and (b), (d), (f) sketch the surface modes on the (001) surface for the A_{1u}, A_{2u}, and E_u states, which are presented in the phase diagrams in Fig. 2. (a), (b) Correspond to the A_{1u} state, (c), (d) the A_{2u} state, and (e), (f) the E_u state. The different colors on the Fermi surfaces in (a), (c), and (e) indicate the magnitude of superconducting gap, and the meaning of the colors is represented by the color bar at the bottom. In (b) and (f), the red cones are the Majorana cones; and in (d), the blue points are the projecting points of the bulk Dirac nodes and the purple lines represent the Majorana zero-energy arcs. Notice that the Majorana zero-energy arcs are all fourfold degenerate since L_1 and L_3 (L_2 and L_4) project onto the same $\bar{X}$ point on the (001) surface. $\bar{\Gamma}$, $\bar{X}$, and $\bar{M}$ are the high-symmetry points in the surface BZ shown in Fig. 1(b).

One major feature in the $\theta = -0.08\pi$ condition is that the A_{1u} state occupies a large area in the phase diagram, as shown in Fig. 2(a). This is closely related to the fact that U_1 is highly anisotropic (isotropic) for the interpocket (intrapocket) interaction while U_2 is isotropic for both the interpocket and intrapocket interactions, as indicated in Table I. When U_1 and U_2 are projected onto the Fermi surfaces, the isotropic and anisotropic properties are expected to be inherited. Therefore, in the region dominated by U_2 (ϕ is around π) the nearly isotropic A_{1u} state shown in Fig. 3(a) is favored. In the region with more anisotropic parameters, i.e., the U_1 dominated area and $|\xi - 1| \gg 0$ area, the states with more anisotropic gap structures are preferred (we treat the nodal state as the most anisotropic one). Moreover, it is worth pointing out that the nodal A_{2u} state merely appears in the large-ξ region. This is because (i) the condition $\xi > 1$ ($\xi < 1$) corresponds to a larger (smaller) Fermi velocity along the Γ-L direction, and (ii) to lower the free energy it tends to open a larger superconducting gap on the part of the Fermi surface where there is larger density of states [89].

2. $\theta = -0.66\pi$

For the $\theta = -0.66\pi$ scenario, in addition to the A_{1u}, A_{2u}, E_u, and T_{2u} states, three different kinds of T_{1u} states, including $T_{1u,[001]}$, $T_{1u,[110]}$, and $T_{1u,[111]}$, also appear in the phase diagram as shown in Fig. 2(b). The A_{1u}, A_{2u}, E_u, and T_{2u} states here have qualitatively the same gap structures and symmetry breaking as those presented in the $\theta = -0.08\pi$ case. The $T_{1u,[001]}$, $T_{1u,[110]}$, and $T_{1u,[111]}$ states can be characterized by the vectors $(r_1^{T_{1u}}, r_2^{T_{1u}}, r_3^{T_{1u}}, r_4^{T_{1u}}) \otimes (0, 0, 1)$, $(r_1^{T_{1u}}, r_2^{T_{1u}}, r_3^{T_{1u}}, r_4^{T_{1u}}) \otimes (1, 1, 0)$, and $(r_1^{T_{1u}}, r_2^{T_{1u}}, r_3^{T_{1u}}, r_4^{T_{1u}}) \otimes (1, 1, 1)$, respectively. The three T_{1u} states are all nodal and the corresponding gap structures on the Fermi surfaces are shown in Fig. 4. According to gap structures, one can notice that the $T_{1u,[001]}$ state is symmetry breaking from the point group O_h to D_{4h}, the $T_{1u,[110]}$ state respects the D_{2h} group, and the $T_{1u,[111]}$ state is D_{3d} symmetric.

Compared to the $\theta = -0.08\pi$ case, in the phase diagram for $\theta = -0.66\pi$ the states whose superconducting gap is more anisotropic are more favored, and the nearly isotropic A_{1u} state only occupies a small region, as shown in Fig. 2(b). This may arise from the fact that the Fermi surfaces in this condition, according to the results in Eq. (7), are dominated by $|J = \frac{3}{2}, j_z = \pm\frac{1}{2}\rangle$ in Table II which is more anisotropic with respect to the p_x, p_y, and p_z orbitals; this may lead to more anisotropic effective interactions on the Fermi surfaces. Correspondingly, the anisotropic superconducting ground states are more favored.

TABLE VI. Irreps of group O_h. C_{2a}, C_{2b}, and C_{2c} are the three twofold rotations. The axis of C_{2a} goes along the x axis in the local reference frame. The axes of C_{2b} and C_{2c} can be obtained from the axis of C_{2a} by C_3 rotation.

	C_3	C_3^2	C_{2a}	C_{2b}	C_{2c}	C_4	C_4^2
$A_{1g}(A_{1u})$	1	1	1	1	1	1	1
$A_{2g}(A_{2u})$	1	1	−1	−1	−1	−1	1
$E_g(E_u)$	$\begin{pmatrix} -\frac{1}{2} & -\frac{\sqrt{3}}{2} \\ \frac{\sqrt{3}}{2} & -\frac{1}{2} \end{pmatrix}$	$\begin{pmatrix} -\frac{1}{2} & -\frac{\sqrt{3}}{2} \\ \frac{\sqrt{3}}{2} & -\frac{1}{2} \end{pmatrix}$	$\begin{pmatrix} 1 & 0 \\ 0 & -1 \end{pmatrix}$	$\begin{pmatrix} -\frac{1}{2} & \frac{\sqrt{3}}{2} \\ -\frac{\sqrt{3}}{2} & -\frac{1}{2} \end{pmatrix}$	$\begin{pmatrix} -\frac{1}{2} & \frac{\sqrt{3}}{2} \\ \frac{\sqrt{3}}{2} & \frac{1}{2} \end{pmatrix}$	$\begin{pmatrix} 1 & 0 \\ 0 & -1 \end{pmatrix}$	$\begin{pmatrix} 1 & 0 \\ 0 & 1 \end{pmatrix}$
$T_{1g}(T_{1u})$	$\begin{pmatrix} 0 & 0 & 1 \\ 1 & 0 & 0 \\ 0 & 1 & 0 \end{pmatrix}$	$\begin{pmatrix} 0 & 1 & 0 \\ 0 & 0 & 1 \\ 1 & 0 & 0 \end{pmatrix}$	$\begin{pmatrix} 0 & -1 & 0 \\ -1 & 0 & 0 \\ 0 & 0 & -1 \end{pmatrix}$	$\begin{pmatrix} -1 & 0 & 0 \\ 0 & 0 & -1 \\ 0 & -1 & 0 \end{pmatrix}$	$\begin{pmatrix} 0 & 0 & -1 \\ 0 & -1 & 0 \\ -1 & 0 & 0 \end{pmatrix}$	$\begin{pmatrix} 0 & -1 & 0 \\ 1 & 0 & 0 \\ 0 & 0 & 1 \end{pmatrix}$	$\begin{pmatrix} -1 & 0 & 0 \\ 0 & -1 & 0 \\ 0 & 0 & 1 \end{pmatrix}$
$T_{2g}(T_{2u})$	$\begin{pmatrix} 0 & 1 & 0 \\ 0 & 0 & 1 \\ 1 & 0 & 0 \end{pmatrix}$	$\begin{pmatrix} 0 & 0 & 1 \\ 1 & 0 & 0 \\ 0 & 1 & 0 \end{pmatrix}$	$\begin{pmatrix} 0 & 1 & 0 \\ 1 & 0 & 0 \\ 0 & 0 & 1 \end{pmatrix}$	$\begin{pmatrix} 0 & 0 & 1 \\ 0 & 1 & 0 \\ 1 & 0 & 0 \end{pmatrix}$	$\begin{pmatrix} 1 & 0 & 0 \\ 0 & 0 & 1 \\ 0 & 1 & 0 \end{pmatrix}$	$\begin{pmatrix} 0 & -1 & 0 \\ 1 & 0 & 0 \\ 0 & 0 & -1 \end{pmatrix}$	$\begin{pmatrix} -1 & 0 & 0 \\ 0 & -1 & 0 \\ 0 & 0 & 1 \end{pmatrix}$

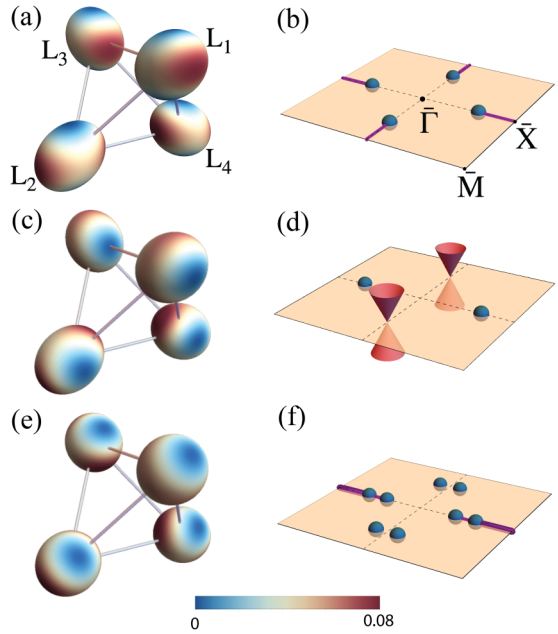

FIG. 4. (a), (c), (e) Show the superconducting gap on the Fermi surfaces and (b), (d), (f) sketch the surface modes on the (001) surface for the $T_{1u,[001]}$, $T_{1u,[110]}$, and $T_{1u,[111]}$ states, which are presented in the phase diagrams in Fig. 2. (a), (b) Correspond to the $T_{1u,[001]}$ state, (c), (d) the $T_{1u,[110]}$ state, and (e), (f) the $T_{1u,[111]}$ state. Similar to Fig. 3, the blue points are the projecting points of the bulk Dirac nodes and the purple lines represent the Majorana zero-energy arcs in (b), (d), and (f). Notice that in (b), the Majorana zero-energy arcs are fourfold degenerate similar to Fig. 3(d); however, in (f) the Majorana zero-energy arcs along $\bar{\Gamma}$-$\bar{X}$ are fourfold degenerate near the BZ boundary but twofold degenerate inside the BZ, which is because the bulk Dirac nodes on the L_1 and L_3 Fermi surfaces no longer project onto the same points on the surface BZ in the $T_{1u,[111]}$ state.

B. Topological property of the ground state

In this section, we present an analysis on the topological properties of the superconducting ground states in the phase diagrams in Fig. 2, and more detailed analysis can be found in Appendix H. Since all the states in the phase diagrams are time-reversal invariant, the SC belongs to class DIII according to the Altland-Zirnbauer classification [90,91]. We take the following strategy in the analysis. We first analyze the topological property of the superconductivity on each Fermi surface. Then, taking all the Fermi surfaces into account, we know the topological property of the whole system for each ground state in the phase diagrams in Fig. 2. To study the topological properties of the ground states, it is convenient to write the odd-parity superconductivity in the vector form, i.e., $\Delta(\mathbf{k}) = \boldsymbol{d}(\boldsymbol{k}) \cdot \boldsymbol{\sigma} i\sigma_2$ with $\boldsymbol{d}(\mathbf{k}) = (d_1(\boldsymbol{k}), d_2(\boldsymbol{k}), d_3(\boldsymbol{k}))$. According to Eq. (11), it is easy to obtain $\hat{c}^\dagger_{\boldsymbol{k}}(\boldsymbol{d}(\boldsymbol{k}) \cdot \boldsymbol{\sigma} i\sigma_2)\hat{c}^\dagger_{-\boldsymbol{k}} = \sum_{\kappa,\zeta} \lambda^*_{\epsilon,\kappa,\zeta} \hat{\Delta}^\dagger_{\epsilon,\kappa,\zeta}(\boldsymbol{k})$ for each irrep channel labeled by ϵ.

1. A_{1u}

We start with the A_{1u} state. The A_{1u} state is fully gapped and it respects the full symmetry of the O_h point group, as indicated in Fig. 3(a). The topological property of such SCs is featured by the 3D winding number [90–92]. On the L_1 Fermi surface, this state can be described by a vector $\mathbf{d}(\mathbf{k}) = (\alpha k_x, \alpha k_y, \beta k_z)$ (α, β are coefficients determined by the parameters in the mean-field calculations). Obviously, the superconductivity on the L_1 Fermi surface is topologically equal to the famous ^{3}He-B phase [93] which is featured by a three-dimensional (3D) winding number $w_1 = \mathrm{sgn}(\alpha\beta)$ with sgn the sign function, and this leads to a Majorana cone on the surface as shown in Fig. 5(b) (only the L_1 Fermi surface in consideration). Since the A_{1u} pairing order is C_4 even, we can conclude that the winding numbers contributed by the superconductivity on the four Fermi surfaces are all the same, and the whole system is characterized by a winding number $w = 4w_1$. Therefore, in total four Majorana cones are expected on the surfaces. Specifically, on the (001) surface, we sketch the Majorana cones in Fig. 3(b).

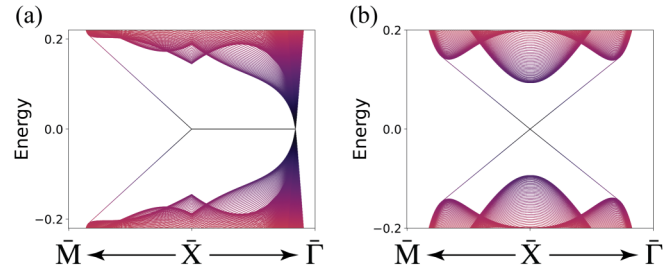

FIG. 5. (a), (b) Show the surface modes for the gapless and full-gap states on the (001) surface, in the condition with merely one single Fermi surface taken into account. $\bar{\Gamma}$, $\bar{X}$, and $\bar{M}$ are the high-symmetry points in the surface BZ shown in Fig. 1(b).

2. A_{2u}

As shown in Fig. 3(c), the A_{2u} state also preserves the O_h point group. However, different from the A_{1u} state it possesses robust superconducting nodes on the Fermi surfaces along the Γ-L direction, making the A_{2u} state the so-called topological Dirac SCs [94]. On the L_1 Fermi surface, the superconductivity can be described by a vector $\mathbf{d}(\mathbf{k}) = (-\alpha k_y, \alpha k_x, 0)$. Namely, in the local frame on the L_1 Fermi surface the pairing takes the form $\hat{\Delta}(\mathbf{k}) \sim (ik_x + k_y)\hat{c}_{\mathbf{k},\uparrow}\hat{c}_{-\mathbf{k},\uparrow} + (ik_x - k_y)\hat{c}_{\mathbf{k},\downarrow}\hat{c}_{-\mathbf{k},\downarrow}$. This is similar to the planar phase of the ^{3}He superfluid [93], where the pairing occurs between electrons with the same spin and carries opposite angular momentum for Cooper pairs with opposite spin. The Dirac nodes lead to Majorana zero-energy arcs on the surfaces on the surface, which are guaranteed by both the mirror symmetry and the chiral symmetry. To be more specific, the Dirac nodes are protected by the 1D mirror-symmetry-protected winding number and more details are presented in Appendix H. On the (001) surface the superconductivity on each Fermi surface results in surface modes in Fig. 5(a), and taking all the four Fermi surfaces into account, we can get the zero-energy arcs illustrated in Fig. 3(d). Notice that the zero-energy arcs in Fig. 3(d) are fourfold degenerate. This phenomenon arises for the following reasons. (i) The eight Dirac nodes on the four Fermi surfaces have four projecting points on the (001) surface because the two Dirac nodes are related by the mirror symmetry M_h which maps $(k_X, k_Y, k_Z) \mapsto (k_X, k_Y, -k_Z)$ in the global frame must project onto the same point on the

(001) surface (the L_1 and L_3 Fermi surfaces are related by M_h, and so do the L_2 and L_4 Fermi surfaces). (ii) The zero-energy arcs from the L_1 and L_3 Fermi surfaces (the L_2 and L_4 Fermi surfaces) which are related by the $C_{2Z} = C_4^2$ symmetry are located at the same position in the surface BZ. (iii) The superconducting order is even under C_{2Z} leading to the zero-energy arcs from the L_1 and L_3 Fermi surfaces cannot hybridize (more details in Appendix H).

Before going to the next state, it is worth pointing out that for a spin-triplet SC, its superconducting gap is nodeless only when its superconducting order is odd under the mirror symmetry crossing the Fermi surfaces. This constraint arises from the fact that in the superconducting order $\Delta(\mathbf{k}) = \boldsymbol{d}(\boldsymbol{k}) \cdot \boldsymbol{\sigma} i\sigma_2$, $\boldsymbol{d}(\boldsymbol{k})$ transforms as a vector while $\boldsymbol{\sigma} i\sigma_2$ transforms as a pseudovector under the crystalline symmetries. The above statement can be directly verified by comparing the A_{1u} and A_{2u} states. For instance, we consider the mirror symmetry M_a which crosses the L_1 Fermi surface and maps $(k_X, k_Y, k_Z) \mapsto (k_Y, k_X, k_Z)$ in the global frame and $(k_x, k_y, k_z) \mapsto (-k_x, k_y, k_z)$ in the local frame defined at the L_1 point in Fig. 1(b) ($M_a = i\sigma_1$ in the local frame). It is easy to check that on the L_1 Fermi surface in the $k_x = 0$ plane M_a transforms the superconducting order as $M_a\Delta(\boldsymbol{k})M_a^T = -\Delta(M_a\boldsymbol{k})$ for the A_{1u} state while $M_a\Delta(\boldsymbol{k})M_a^T = \Delta(M_a\boldsymbol{k})$ for the A_{2u} state.

3. E_u

The E_u state in Fig. 3(e) is fully gapped with symmetry breaking from point group O_h to D_{4h}. Despite the symmetry breaking, the E_u state shares similar topological property with the A_{1u} state. On the L_1 Fermi surface, it can be described by a vector $\mathbf{d}(\mathbf{k}) = (\alpha k_x, -\alpha k_y + \beta k_z, \gamma k_y)$, which contributes a winding number $w_1 = -\mathrm{sgn}(\alpha\beta\gamma)$. Moreover, the C_4 rotational symmetry preserves in the E_u state and the superconducting order remains invariant under the C_4 rotational symmetry. Hence, the superconductivity on the four Fermi surfaces contributes the same winding number and the whole system has a total winding number $w = 4w_1$. The surface modes for the E_u state are expected to be similar to that in the A_{1u} state, as indicated in Fig. 3(f).

4. T_{1u}

In the phase diagram in Fig. 2, the three T_{1u} states are all nodal and they respect different symmetry groups, as illustrated in Fig. 4. As pointed out, the $T_{1u,[001]}$ state in Fig. 4(a) is a symmetry-breaking state from point group O_h to D_{4h}, the $T_{1u,[110]}$ state in Fig. 4(c) from point group O_h to D_{2h}, and the $T_{1u,[111]}$ state in Fig. 4(e) from point group O_h to D_{3d}. The nodal gap structure in the three states is guaranteed by the mirror symmetries.

The analysis for the $T_{1u,[001]}$ state is similar to the A_{2u} state. Specifically, the $T_{1u,[001]}$ state preserves the mirror symmetry M_a, and on the L_1 Fermi surface, the $T_{1u,[001]}$ state can be depicted by the vector $\mathbf{d}(\mathbf{k}) = (\alpha k_y + \beta k_z, \gamma_1 k_x, \gamma_2 k_x)$. One can check that the superconducting order is even under M_a, leading to nodes on the L_1 Fermi surface. As the C_4 symmetry is preserved in the $T_{1u,[001]}$ state and the four Fermi surfaces are related by the C_4 symmetry, we can immediately get the superconductivity on the other Fermi surfaces and the gap structure in Fig. 4(a). The $T_{1u,[001]}$ has similar surface modes with the A_{2u} state as shown in Fig. 4(b), and the analysis is also similar. The similarity between the two states can be naively understood from the fact that compared to the A_{2u} state, the $T_{1u,[001]}$ state only breaks the threefold rotational symmetry which can never be preserved on the (001) surface.

In the $T_{1u,[111]}$ state, similar to the $T_{1u,[001]}$ state on each Fermi surface there are two Dirac nodes, as presented in Fig. 4(e). On the L_1 and L_3 Fermi surfaces, the Dirac nodes are protected by the mirror symmetry M_a (M_a is defined in the A_{2u} part); and the superconductivity on the L_2 and L_4 Fermi surfaces can be obtained by taking the threefold rotational symmetry C_3 into account, as C_3 is preserved in the $T_{1u,[111]}$ state and the $L_2 \sim L_4$ Fermi surfaces are related by C_3. The $T_{1u,[111]}$ state possesses different surface modes on the (001) surface compared to the $T_{1u,[001]}$ state, as illustrated in Fig. 4(f). One feature for the $T_{1u,[111]}$ state is that the eight Dirac nodes in the bulk energy spectrum project onto eight different points on the (001) surface since there are no symmetry-enforced degenerate projecting points here (the $T_{1u,[111]}$ state respects the D_{3d} point group and breaks the mirror symmetry M_h which is vital for the surface modes for the $T_{1u,[001]}$ state). Another feature for the $T_{1u,[111]}$ state is that the zero-energy arcs survive only along one direction in the surface BZ shown in Fig. 4(f) because the mirror symmetry protecting the bulk Dirac nodes on the L_1 and L_3 Fermi surfaces (which is in fact M_a) preserves but the mirror symmetries protecting the bulk Dirac nodes on the L_2 and L_4 Fermi surfaces cannot be maintained on the (001) surface. Here, it is worth mentioning that the zero-energy arcs in Fig. 4(f) are obtained by analyzing the topological invariant based on the numerical mean-field results because the L_1 and L_3 Fermi surfaces are not related by any symmetry in the $T_{1u,[111]}$ state.

Compared to the above two states, the $T_{1u,[110]}$ state is more special. Based on the numerical results, we find that the superconductivity on the L_1 and L_3 Fermi surfaces are nodal with two Dirac nodes on each Fermi surface, and on the L_2 and L_4 Fermi surfaces the superconducting gap is full gap, shown in Fig. 4(c). In fact, this can be understood from the following two aspects. (i) The $T_{1u,[110]}$ state merely respects the D_{2h} symmetry group, under which the L_1 and L_3 Fermi surfaces (L_2 and L_4 Fermi surfaces) are related with each other but the $L_1(3)$ and $L_2(4)$ Fermi surfaces are not related. (ii) The superconducting order is even under the mirror symmetry M_a (as mentioned, M_a crosses the L_1 and L_3 Fermi surfaces), which makes the superconductivity nodal on the L_1 and L_3 Fermi surfaces; however, the superconducting order is odd under the mirror symmetry $C_4M_aC_4^{-1}$ ($C_4M_aC_4^{-1}$ is the mirror symmetry crossing the L_2 and L_4 Fermi surfaces, i.e., the $\Gamma L_2 L_4$ plane), and this leads to the nodeless gap structures on the L_2 and L_4 Fermi surfaces. The surface modes on the (001) surface for the $T_{1u,[110]}$ state are sketched in Fig. 4(d). One can notice that in the $T_{1u,[110]}$ state the Dirac nodes on the L_1 and L_3 Fermi surfaces cannot result in zero-energy arcs between the projecting points of the Dirac nodes [the four Dirac nodes have two projecting points on the (001) surface due to the mirror symmetry M_h]. This is because, though the Dirac nodes on each of the Fermi surfaces (the L_1 and

L_3 Fermi surfaces) do lead to zero-energy arcs on the (001) surface shown in Fig. 5(a), the zero-energy arcs from the two Fermi surfaces will hybridize and gap out on the (001) surface, which is different from the condition in the $T_{1u,[001]}$ state shown in Fig. 4(b). The difference arises from the fact that the L_1 and L_3 Fermi surfaces are related by $C_{2Z} = C_4^2$, and in the $T_{1u,[110]}$ ($T_{1u,[001]}$) state the superconducting order is odd (even) under C_{2Z}. The full-gap superconductivity on the L_2 and L_4 Fermi surfaces leads to two Dirac cones on the (001) surface, which is protected by a mirror Chern number $|C_M| = 2$ (a more detailed analysis for the mirror Chern number is presented in Appendix H). The mirror Chern number is defined as $C_M = (C_{+i} - C_{-i})/2$, where C_{+i} (C_{-i}) is the Chern number in the $C_4 M_a C_4^{-1}$ invariant subspace with mirror eigenvalue $+i$ ($-i$) the eigenvalues of M_a in the $\Gamma L_2 L_4$ plane. Here, we can consider the mirror Chern number because for the mirror odd superconductivity in each of the mirror-invariant subspaces in the $\Gamma L_2 L_4$ plane the particle-hole symmetry preserves [95] while neither the time-reversal symmetry nor the chiral symmetry (the chiral symmetry is the product of the time-reversal symmetry and the particle-hole symmetry) maintains. Moreover, the two mirror-invariant subspaces are related by the time-reversal symmetry, which means that the Chern numbers in the two subspaces are always opposite with each other and the mirror Chern number satisfies $C_M = C_{+i} = -C_{-i}$. It is easy to check the superconductivity on the L_2 Fermi surface contributes mirror Chern number 1 or -1. Aside from the L_2 Fermi surface, the L_4 Fermi surface which is related to the L_2 Fermi surface by C_{2Z} contributes the same mirror Chern number. Therefore, the SC has $|C_M| = 2$ on the $\Gamma L_2 L_4$ plane. Based on the above analysis, the surface modes for the $T_{1u,[110]}$ state on the (001) surface are expected as that in Fig. 4(d).

5. T_{2u}

As mentioned, the two T_{2u} states in the phase diagram in Fig. 2 are characterized by the vectors $(r_1^{T_{2u}}, r_2^{T_{2u}}, r_3^{T_{2u}}, r_4^{T_{2u}}, r_5^{T_{2u}}) \otimes (1, 1, 1)$ and $(r_1^{T_{2u}}, r_2^{T_{2u}}, r_3^{T_{2u}}, r_4^{T_{2u}}, r_5^{T_{2u}}) \otimes (0, 0, 1)$, respectively. Both of the two states are featured by a nodeless and strongly anisotropic gap structure, as shown in Fig. 6.

The $T_{2u,[001]}$ state is a symmetry-breaking state from point group O_h to D_{4h}. We still begin with the superconductivity on the L_1 Fermi surface, which can be described by a vector $\mathbf{d}(\mathbf{k}) = (\alpha k_x, \beta_1 k_y + \beta_2 k_z, \gamma_1 k_y + \gamma_2 k_z)$. Obviously, the L_1 Fermi surface contributes a winding number $w_1 = \mathrm{sgn}(\alpha\beta_1\gamma_2 - \alpha\beta_2\gamma_1)$. As mentioned, the T_{2u} state keeps the C_4 rotational symmetry. However, in this case, the superconducting order is C_4 odd, namely, there is a π phase difference between the pairing amplitude on the L_1 and L_3 Fermi surfaces and the superconducting orders on the L_2 and L_4 Fermi surfaces. Therefore, the winding numbers contributed by the four Fermi surfaces have the following relation $w_1 = -w_2 = w_3 = -w_4$, and the whole system has a total winding number $w = 0$. Although the $T_{2u,[001]}$ state has a total winding number zero, it belongs to a second-order TSC state [19,96–109]. Moreover, the second-order topological superconductivity here thoroughly stems from the pairing on the Fermi surfaces and is protected by the mirror symmetry intrinsically. This is different from the previous studies where the second-order topological superconductivity is realized by introducing external mass domain into the edge modes of a topological insulator[103–106]. Specifically, the second-order topological superconductivity is protected by the even mirror Chern number defined according to the M_a and $C_4 M_a C_4^{-1}$ mirror symmetries, namely, the mirror Chern numbers in the $\Gamma L_1 L_3$ plane and $\Gamma L_2 L_4$ plane. The analysis for the two mirror Chern numbers is similar to that in the $T_{1u,[110]}$ state in the above, and it turns out the mirror Chern number in the $\Gamma L_1 L_3$ plane (the $\Gamma L_2 L_4$ plane) is $|C_M| = 2$ ($|C_M| = 2$). A more detailed discussion on the mirror Chern number is listed in Appendix H. For a SC with an even mirror Chern number, it must be a second-order TSC protected by the mirror symmetry [101,110]. Correspondingly, in our case two Majorana cones are expected on the M_a ($C_4 M_a C_4^{-1}$) invariant line in the surface BZ on the (001) surface, and there will be one pair of helical Majorana modes localized on each hinge respecting the mirror symmetry M_a ($C_4 M_a C_4^{-1}$) such as the intersection between the (100) and (010) surfaces. According to the above analysis, we can sketch the topological surface states and hinge states for the $T_{2u,[001]}$ state as shown in Fig. 6(b).

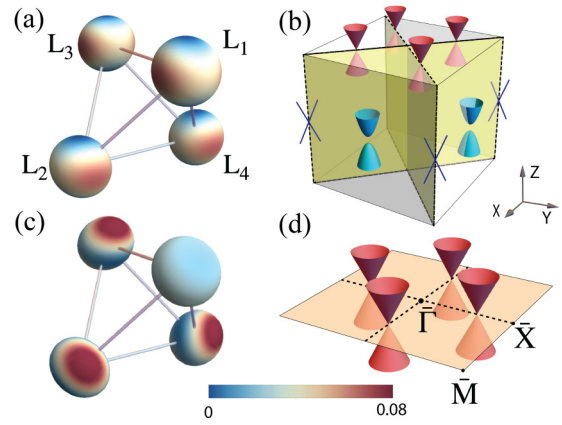

FIG. 6. (a), (c) Show the superconducting gap on the Fermi surfaces for the $T_{2u,[001]}$ and $T_{2u,[111]}$ states, respectively. (d) Sketches the surface modes on the (001) surface for the $T_{2u,[111]}$ state. (b) Illustrates the surface modes and hinge modes for the $T_{2u,[001]}$ state. It supports four Majorana cones on the (001) surface which are protected by the mirror symmetries M_a: $(k_X, k_Y, k_Z) \mapsto (k_Y, k_X, k_Z)$ and M_b: $(k_X, k_Y, k_Z) \mapsto (-k_Y, -k_X, k_Z)$; on the (100) and (010) surfaces no Majorana cones are supported, but there exists one pair of Majorana helical hinge modes at each intersection between the (100) and (010) surfaces.

For the $T_{2u,[111]}$ state, it has symmetry breaking from O_h to D_{3d}, as shown in Fig. 6(c). Since the $L_2 \sim L_4$ Fermi surfaces are related by the C_3 rotational symmetry and the superconducting order is even under C_3, the superconductivity on the $L_2 \sim L_4$ Fermi surfaces contributes the same winding number. As to the L_1 Fermi surface, there is no symmetry operation which maps it to the other Fermi surfaces. According to the numerical results, we find that it contributes the same winding number with each of the other three Fermi surfaces. Therefore, the $T_{2u,[111]}$ state is a first-order topological SC with total

winding number $w = 4$, and we sketch its surface modes in Fig. 6(d).

IV. DISCUSSION AND CONCLUSION

Our theory may account for the interesting results in the typical IV-VI semiconductor such as SnTe in recent experiments, including the zero-bias peak in In-doped SnTe in the soft point-contact spectroscopy measurements [87] and the gapless excitations on the surface of superconducting $Pb_{1-x}Sn_xTe$ revealed by the high-resolution STM measurements [88] where both of the measurements are done on the (001) surface. The penetration depth and the STM measurements [88,111] indicate a nodeless superconducting gap in $Sn_{1-x}In_xTe$ and $Pb_{1-x}Sn_xTe$. As indicated in the phase diagram in Fig. 2, the A_{1u}, E_u, $T_{2u,[001]}$, and $T_{2u,[111]}$ superconductivity can be candidates for the ground states. This is different from the previous study [112], where SnTe has been predicted to be in the A_{1u} state. According to our theory, all of the three states are fully gapped and support gapless excitations on the (001) surface. To distinguish the three states, the upper critical field measurements can provide important information. The $T_{2u,[111]}$ state can be distinguished from others by measuring the upper critical field applied along the [001] direction, since among the fully gapped states only it breaks the fourfold rotational symmetry. As the E_u and $T_{2u,[001]}$ states preserve the fourfold rotation but break the threefold rotational symmetry along the [111] direction, the upper critical field is expected to break the threefold rotational symmetry accordingly, if the field is applied perpendicular to the [111] direction. The $T_{2u,[001]}$ state can be distinguished from the E_u state by measuring the surface modes on different surfaces. Since the $T_{2u,[001]}$ state is a second-order TSC, it only supports gapless surface modes on certain surfaces, as illustrated in Fig. 6(b); the E_u state is a first-order TSC with winding number 4, which supports Majorana cones on every surface. Therefore, if the soft point-contact spectroscopy measurements are done on the (111) surface, a zero-bias peak is expected in the E_u state while it is absent for the T_{2u} state; similarly, if we take the high-resolution quasiparticle interference measurements on the (111) surface, the gapless excitations can be observed only in the E_u state. Moreover, the helical Majorana modes at the intersection between the (100) and (010) surfaces can provide smoking-gun evidence for the $T_{2u,[001]}$ state, which can be detected by the high-resolution STM measurements.

Although the A_{2u} and T_{1u} states seem not to be the ground state for SnTe, it may be favored in other doped superconducting IV-VI semiconductors or systems with similar crystal and electronic structures. Therefore, we also discuss its experimental characteristics here. Due to the Dirac points in its energy spectrum, the specific heat would scale with T^3 at low temperature; and the zero-energy arcs on the surface can provide further evidences in the quasiparticle interference measurements.

In summary, the superconductivity in underdoped *AB*-type IV-VI semiconductors has been studied theoretically. We start from a spin-orbit-coupled *p*-orbital model with interaction restricted to the next-nearest neighbors. By projecting the *p* orbitals onto the Fermi surfaces, a single-band effective model is derived. We solve the model at the mean-field level and study the possible spin-triplet superconductivity systematically. We find that various superconducting states, including the A_{1u}, A_{2u}, E_u, T_{1u}, and T_{2u} states, appear in the phase diagram with respect to the anisotropy of the Fermi surface and the interaction strength. All the states are time-reversal invariant. Symmetry breaking and topological properties of the ground states are discussed. The corresponding edge states are presented. The experimental detections for the ground states are suggested.

TABLE VII. The anisotropic coefficient ξ for the *AB*-type IV-VI semiconductors. ξ has been fit for both the conduction band bottom and valence band top based on the first-principle results.

ξ	SnTe	PbTe	PbSe
Valence band	0.417724	0.0940988	0.798178
Conduction band	1.64083	0.110617	0.790197

ACKNOWLEDGMENT

The work is supported by the Ministry of Science and Technology of China (Grant No. 2016YFA0302400) and Chinese Academy of Sciences (Grant No. XDB33000000).

APPENDIX A: PARAMETERS FOR THE *AB*-TYPE IV-VI SEMICONDUCTORS

Based on the first-principle calculations on the electronic structures of the *AB*-type IV-VI semiconductors, including SnTe, PbTe, and PbSe, we fit the parameters ξ and θ in the main text for these materials, as listed in Tables VII and VIII in the following. The anisotropic parameter ξ is obtained by fitting the bands along the $[1\bar{1}0]$ and [111] directions (both directions are defined in the global frame). The parameter θ featuring the mix between the $|J = \frac{3}{2}, j_z = \pm\frac{1}{2}\rangle$ and $|J = \frac{1}{2}, j_z = \pm\frac{1}{2}\rangle$ states on the Fermi surfaces is obtained based on the bands at the L_1 point (we focus on the small-Fermi-surface limit) in the presence of spin-orbit coupling from the first-principle simulations.

APPENDIX B: SUPERCONDUCTING PHASE DIAGRAMS

Based on the numerical method presented in the following sections, we solve the mean-field Hamiltonian and get the superconducting phase diagrams. In the main text, we only show the results for the two cases with $\theta = -0.25 = -0.08\pi$ and $\theta = -2.0735 = -0.66\pi$. Here, we present a systematic study with respect to different values of θ, and the results are shown

TABLE VIII. The mixing angle θ for the *AB*-type IV-VI semiconductors at the L_1 point.

θ	SnTe	PbTe	SnSe
Valence band	−0.780014	−2.5244	−1.48254
Conduction band	−2.2809	−0.251672	−2.05523

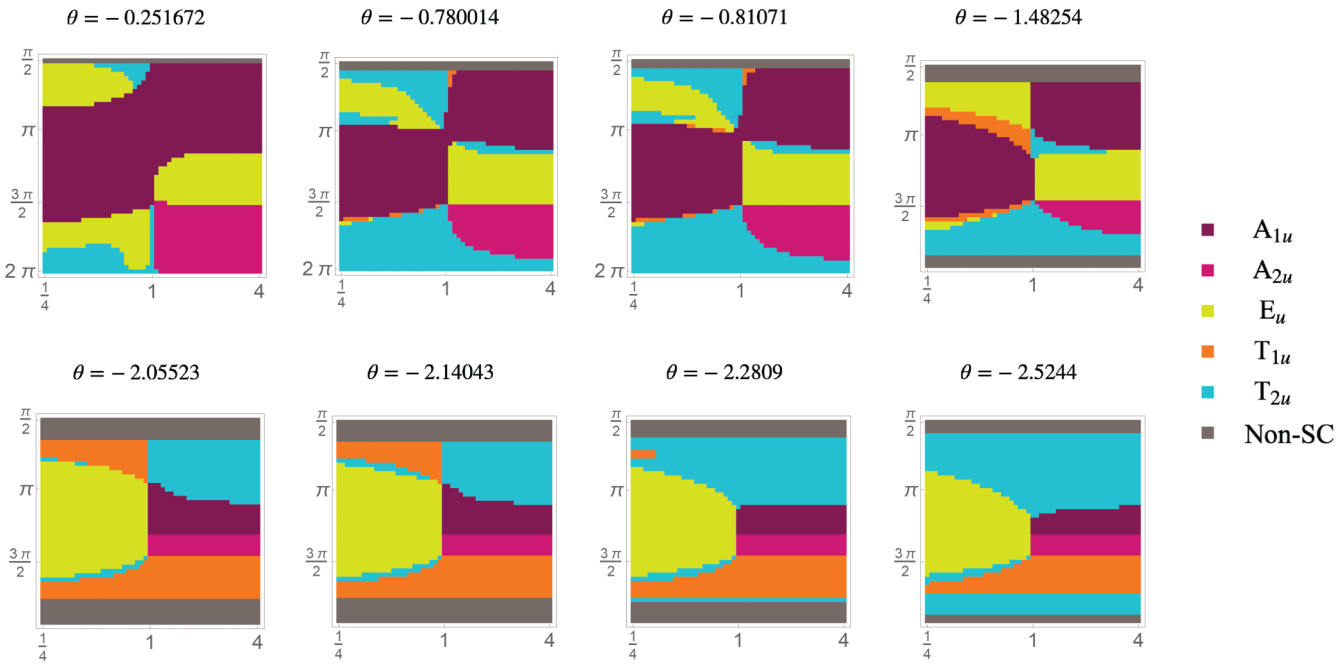

FIG. 7. The phase diagrams with respect to different θ.

in Fig. 7. The detailed phase diagrams for the SnTe condition, $\theta = -0.78 = -0.248\pi$ and $\theta = -2.28 = -0.726\pi$, are presented in Fig. 8. Notice that the superconducting ground states appearing in phase diagrams for SnTe are the same as those in the phase diagrams in the main text.

Aside from the phase diagrams with respect to the different values of θ, we also present the results for the PbTe in Fig. 9, whose Fermi surfaces are highly anisotropic. As shown in Fig. 9(a), if the Fermi energy lies in the conduction bands, only the full-gap superconducting states are supported; and if the Fermi energy lies in the valence bands, the condition is more complicated as shown in Fig. 9(b). Notice that in the phase diagrams, except for the $E_{u,[01]}$ state, other states are all the same as those in the main text. In fact, the $E_{u,[01]}$ state has similar gap structures and topological properties with the A_{2u} state since their superconducting orders transform in a similar way under the crystalline symmetries (compared to the A_{2u} state, the $E_{u,[01]}$ state only breaks the threefold rotational symmetry) which can be seen from Table VI in the main text.

APPENDIX C: MOMENTUM DEPENDENCE OF INTRAPOCKET AND INTERPOCKET INTERACTIONS

The lattice structure and Brillouin zone are shown in Fig. 1 in the main text. We introduce the density-density interaction in the paper written as below:

$$H_{\text{int}} = U_0 \sum_i \hat{n}_i \hat{n}_i + \frac{U_1}{2} \sum_{\langle ij \rangle} \hat{n}_i \hat{n}_j + \frac{U_2}{2} \sum_{\langle\langle ij \rangle\rangle} \hat{n}_i \hat{n}_j. \quad \text{(C1)}$$

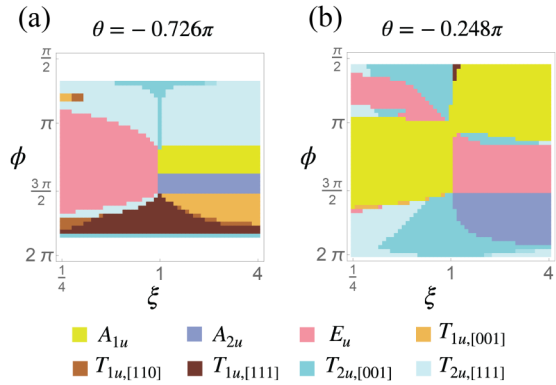

FIG. 8. The phase diagrams for SnTe, where $\theta = -0.726\pi$ corresponds to the conduction band and $\theta = -0.248\pi$ corresponds to the valence band.

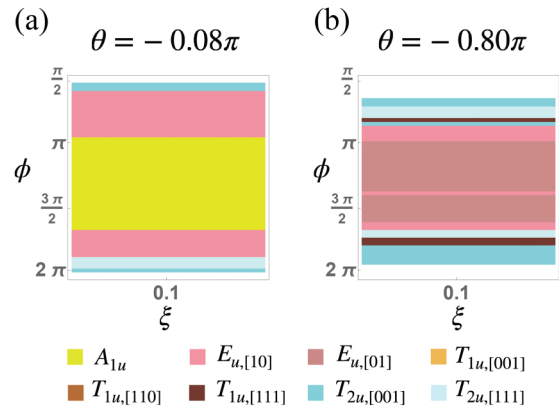

FIG. 9. The phase diagrams corresponding to the anisotropy coefficient $\xi = 0.1$.

We take the Fourier transformation to Eq. (C1) and obtain

$$H_{\text{int}} = \frac{1}{N}\sum_{\boldsymbol{K}_1,\boldsymbol{K}_2,\boldsymbol{q},l_1,l_2} \hat{\psi}^{\dagger}_{\boldsymbol{K}_1+\boldsymbol{q},l_1}\hat{\psi}_{\boldsymbol{K}_1,l_1}\hat{\psi}^{\dagger}_{\boldsymbol{K}_2-\boldsymbol{q},l_2}\hat{\psi}_{\boldsymbol{K}_2,l_2} \times\left(U_0+\frac{U_1}{2}\sum_{\langle ij\rangle}e^{-i\boldsymbol{r}_{ij}\cdot\boldsymbol{q}}+\frac{U_2}{2}\sum_{\langle\langle ij\rangle\rangle}e^{-i\boldsymbol{r}_{ij}\cdot\boldsymbol{q}}\right), \quad \text{(C2)}$$

where N is the number of the sites. We restrict the electronic states involved in the interaction within an area near the Fermi surfaces and set $\boldsymbol{K}=\mathbf{L}_n+\boldsymbol{k}$, $\boldsymbol{K}+\boldsymbol{q}=\mathbf{L}_m+\boldsymbol{k}'$, $|E_{\boldsymbol{k}}-\mu|<\delta\mu$, $|E_{\boldsymbol{k}'}-\mu|<\delta\mu$, where $\mathbf{L}_m$ is the vector from the Γ point to L_m point; $E_{\boldsymbol{k}}$ is the kinetic energy of the states with momentum $\mathbf{L}_{1,2,3,4}+\boldsymbol{k}$; μ is the chemical potential and $\delta\mu$ is the cutoff energy in the summation $\delta\mu\ll\mu$. We can derive $|\boldsymbol{k}|, |\boldsymbol{k}'|\sim k_F\ll|\mathbf{L}_{1,2,3,4}|$, $\boldsymbol{q}=\mathbf{L}_m-\mathbf{L}_n+\boldsymbol{k}'-\boldsymbol{k}=\mathbf{L}_{mn}+\tilde{\boldsymbol{q}}$ with $\mathbf{L}_{mn}=\mathbf{L}_m-\mathbf{L}_n$ and $\tilde{\boldsymbol{q}}\equiv\boldsymbol{k}'-\boldsymbol{k}$, $|\tilde{\boldsymbol{q}}|\ll|\mathbf{L}_{mn}|$. We define a new density operator $\hat{\rho}_{\tilde{\boldsymbol{q}},mn}=\widetilde{\sum}_{\boldsymbol{k},l}\hat{\psi}^{\dagger}_{l}(\boldsymbol{k}+\tilde{\boldsymbol{q}}+\mathbf{L}_m)\hat{\psi}_l(\boldsymbol{k}+\mathbf{L}_n)$, where we use $\widetilde{\sum_{\boldsymbol{k}}}$ to denote a cutoff on both the kinetic energy $E_{\boldsymbol{k}}$ and $E_{\boldsymbol{k}+\tilde{\boldsymbol{q}}}$ in the summation. Then, the Hamiltonian becomes

$$H_{\text{int}} = \frac{1}{N}\widetilde{\sum_{\tilde{\boldsymbol{q}},m=n}}\hat{\rho}_{\tilde{\boldsymbol{q}},mm}\hat{\rho}_{-\tilde{\boldsymbol{q}},mm}\left(U_0+\frac{U_1}{2}\sum_{\langle ij\rangle}e^{-i\boldsymbol{r}_{ij}\cdot\tilde{\boldsymbol{q}}}+\frac{U_2}{2}\sum_{\langle\langle ij\rangle\rangle}e^{-i\boldsymbol{r}_{ij}\cdot\tilde{\boldsymbol{q}}}\right) + \frac{1}{N}\widetilde{\sum_{\tilde{\boldsymbol{q}},m,n}}\hat{\rho}_{\tilde{\boldsymbol{q}},mn}\hat{\rho}_{-\tilde{\boldsymbol{q}},mn}\left(U_0+\frac{U_1}{2}\sum_{\langle ij\rangle}e^{-i\boldsymbol{r}_{ij}\cdot(\tilde{\boldsymbol{q}}+\mathbf{L}_{mn})}+\frac{U_2}{2}\sum_{\langle\langle ij\rangle\rangle}e^{-i\boldsymbol{r}_{ij}\cdot(\tilde{\boldsymbol{q}}+\mathbf{L}_{mn})}\right). \quad \text{(C3)}$$

From Fig. 1(a) we can obtain $\boldsymbol{r}_{\langle ij\rangle}=\frac{a_0}{2}(\pm1,\pm1,0)^{\intercal}$, $\frac{a_0}{2}(\pm1,0,\pm1)^{\intercal}$, $\frac{a_0}{2}(0,\pm1,\pm1)^{\intercal}$, and $\boldsymbol{r}_{\langle\langle ij\rangle\rangle}=a_0(\pm1,0,0)^{\intercal}$, $a_0(0,\pm1,0)^{\intercal}$, $a_0(0,0,\pm1)^{\intercal}$. From Fig. 1(b) we can obtain $\mathbf{L}_{mn}=\frac{2\pi}{a_0}(\pm1,0,0)^{\intercal}$, $\frac{2\pi}{a_0}(0,\pm1,0)^{\intercal}$, $\frac{2\pi}{a_0}(0,0,\pm1)^{\intercal}$. We substitute $\boldsymbol{r}_{\langle ij\rangle}$, $\boldsymbol{r}_{\langle\langle ij\rangle\rangle}$, and $\mathbf{L}_{mn}$ into Eq. (C3) and obtain the intrapocket and interpocket interactions from different neighbors as follows,

a. Intrapocket the nearest neighbors:

$$\begin{aligned}H_{\text{int-intra-n}} &= \frac{1}{N}\frac{U_1}{2}\sum_{\tilde{\boldsymbol{q}},m}\sum_{\omega,\omega'=x,y,z}^{\omega\neq\omega'}\hat{\rho}_{\tilde{\boldsymbol{q}},mm}\hat{\rho}_{-\tilde{\boldsymbol{q}},mm}\left(e^{-i\frac{a_0}{2}(\tilde{q}_\omega+\tilde{q}_{\omega'})}+e^{-i\frac{a_0}{2}(\tilde{q}_\omega-\tilde{q}_{\omega'})}+e^{-i\frac{a_0}{2}(-\tilde{q}_\omega+\tilde{q}_{\omega'})}+e^{-i\frac{a_0}{2}(-\tilde{q}_\omega-\tilde{q}_{\omega'})}\right)\\ &= \frac{1}{N}U_1\sum_{\tilde{\boldsymbol{q}},m}\sum_{\omega,\omega'=x,y,z}^{\omega\neq\omega'}\hat{\rho}_{\tilde{\boldsymbol{q}},mm}\hat{\rho}_{-\tilde{\boldsymbol{q}},mm}\left[\cos\left(\frac{a_0}{2}(\tilde{q}_\omega+\tilde{q}_{\omega'})\right)+\cos\left(\frac{a_0}{2}(\tilde{q}_\omega-\tilde{q}_{\omega'})\right)\right]\\ &= \frac{1}{N}U_1\sum_{\tilde{\boldsymbol{q}},m}\hat{\rho}_{\tilde{\boldsymbol{q}},mm}\hat{\rho}_{-\tilde{\boldsymbol{q}},mm}\left(6-\frac{a_0^2}{2}(\tilde{q}_x^2+\tilde{q}_y^2+\tilde{q}_z^2)\right).\end{aligned} \quad \text{(C4)}$$

b. Intrapocket the next nearest neighbors:

$$\begin{aligned}H_{\text{int-intra-nn}} &= \frac{1}{N}\frac{U_2}{2}\sum_{\tilde{\boldsymbol{q}},m}\hat{\rho}_{\tilde{\boldsymbol{q}},mm}\hat{\rho}_{-\tilde{\boldsymbol{q}},mm}\left(e^{ia_0\tilde{q}_x}+e^{-ia_0\tilde{q}_x}+e^{ia_0\tilde{q}_y}+e^{-ia_0\tilde{q}_y}+e^{i\frac{a_0}{2}\tilde{q}_z}+e^{-i\frac{a_0}{2}\tilde{q}_z}\right)\\ &= \frac{1}{N}U_2\sum_{\tilde{\boldsymbol{q}},m}\hat{\rho}_{\tilde{\boldsymbol{q}},mm}\hat{\rho}_{-\tilde{\boldsymbol{q}},mm}[\cos(a_0\tilde{q}_x)+\cos(a_0\tilde{q}_y)+\cos(a_0\tilde{q}_z)]\\ &= \frac{1}{N}U_1\sum_{\tilde{\boldsymbol{q}},m}\hat{\rho}_{\tilde{\boldsymbol{q}},mm}\hat{\rho}_{-\tilde{\boldsymbol{q}},mm}\left(3-\frac{a_0^2}{2}(\tilde{q}_x^2+\tilde{q}_y^2+\tilde{q}_z^2)\right).\end{aligned} \quad \text{(C5)}$$

c. Interpocket the nearest neighbors:

$$\begin{aligned}H_{\text{int-inter-n}} &= \frac{1}{N}\frac{U_1}{2}\sum_{\tilde{\boldsymbol{q}}mn}\sum_{\langle ij\rangle}\hat{\rho}_{\tilde{\boldsymbol{q}},mn}\hat{\rho}_{-\tilde{\boldsymbol{q}},mn}e^{-i(\mathbf{L}_{mn}\cdot\boldsymbol{r}_{ij}+\tilde{\boldsymbol{q}}\cdot\boldsymbol{r}_{ij})}\\ &= \frac{1}{N}U_1\sum_{\tilde{\boldsymbol{q}}mn}\hat{\rho}_{\tilde{\boldsymbol{q}},mn}\hat{\rho}_{-\tilde{\boldsymbol{q}},mn}\left[\cos\left(\pi+\frac{a_0}{2}(\tilde{q}_{\perp1}+\tilde{q}_{\parallel})\right)+\cos\left(\pi+\frac{a_0}{2}(\tilde{q}_{\perp1}-\tilde{q}_{\parallel})\right)+\cos\left(\pi+\frac{a_0}{2}(\tilde{q}_{\perp2}+\tilde{q}_{\parallel})\right)\right.\\ &\quad\left.+\cos\left(\pi+\frac{a_0}{2}(\tilde{q}_{\perp2}-\tilde{q}_{\parallel})\right)+\cos\left(\frac{a_0}{2}(\tilde{q}_{\perp1}+\tilde{q}_{\perp2})\right)+\cos\left(\frac{a_0}{2}(\tilde{q}_{\perp1}-\tilde{q}_{\perp2})\right)\right]\\ &= \frac{1}{N}U_1\sum_{\tilde{\boldsymbol{q}}mn}\hat{\rho}_{\tilde{\boldsymbol{q}},mn}\hat{\rho}_{-\tilde{\boldsymbol{q}},mn}\left(-2+\frac{1}{2}\tilde{q}_{\parallel}^2\right),\end{aligned} \quad \text{(C6)}$$

where we use $\tilde{q}_{\parallel}$ to denote the component of $\tilde{\boldsymbol{q}}$ parallel to $\mathbf{L}_{mn}$ and $\tilde{q}_{\perp 1,2}$ to denote the other two components perpendicular to $\mathbf{L}_{mn}$. For example, we take $m=1, n=2, \mathbf{L}_{12}=\frac{2\pi}{a_0}(-1,0,0)$. $\tilde{q}_{\parallel}$ is taken as $\tilde{q}_x$ and $\tilde{q}_{\perp 1,2}$ are taken as $\tilde{q}_y$ and $\tilde{q}_z$.

d. Interpocket the next-nearest neighbors:

$$
\begin{aligned}
H_{\text{int-intra-nn}} &= \frac{1}{N}\frac{U_2}{2}\sum_{\tilde{\boldsymbol{q}}mn}\hat{\rho}_{\tilde{\boldsymbol{q}},mn}\hat{\rho}_{-\tilde{\boldsymbol{q}},mn}\left(e^{i(2\pi+a_0\tilde{q}_{\parallel})}+e^{i(2\pi-a_0\tilde{q}_{\parallel})}+e^{ia_0\tilde{q}_{\perp 1}}+e^{-ia_0\tilde{q}_{\perp 1}}+e^{i\frac{a_0}{2}\tilde{q}_{\perp 2}}+e^{-i\frac{a_0}{2}\tilde{q}_{\perp 2}}\right)\\
&= \frac{1}{N}U_2\sum_{\tilde{\boldsymbol{q}}}\hat{\rho}_{\tilde{\boldsymbol{q}},mn}\hat{\rho}_{-\tilde{\boldsymbol{q}},mn}[\cos(a_0\tilde{q}_{\parallel})+\cos(a_0\tilde{q}_{\perp 1})+\cos(a_0\tilde{q}_{\perp 2})]\\
&= \frac{1}{N}U_2\sum_{\boldsymbol{q}}\hat{\rho}_{\tilde{\boldsymbol{q}},mn}\hat{\rho}_{-\tilde{\boldsymbol{q}},mn}\left(3-\frac{a_0^2}{2}(\tilde{q}_{\parallel}^2+\tilde{q}_{\perp 1}^2+\tilde{q}_{\perp 2}^2)\right).
\end{aligned}
\tag{C7}
$$

Here we simplify $\tilde{q}_x^2+\tilde{q}_y^2+\tilde{q}_z^2$ and $\tilde{q}_{\parallel}^2+\tilde{q}_{\perp 1}^2+\tilde{q}_{\perp 2}^2$ as $\tilde{q}^2$ and write the interaction as $H_{\text{int}}=\sum_{i,\tilde{\boldsymbol{q}}}\frac{1}{N}U_i f_i(\tilde{\boldsymbol{q}}+\mathbf{L}_{mn})\hat{\rho}_{\tilde{\boldsymbol{q}},mn}\hat{\rho}_{-\tilde{\boldsymbol{q}},mn}$ with $f_i(\tilde{\boldsymbol{q}}+\mathbf{L}_{mn})$ listed in Table I.

APPENDIX D: PROJECTION FROM ORBITAL BASIS TO THE BAND BASIS

In the weak-coupling condition, only the interaction between the states on the Fermi surfaces is essential. In the above, we have constrained the momentum $\boldsymbol{K}$ and $\boldsymbol{K}+\boldsymbol{q}$ near the Fermi surfaces and take an energy cutoff in the summation. To obtain the effective interaction on the Fermi surfaces, we need to project the states from the orbital basis onto the states on the Fermi surfaces (remember that in the low-doping condition, we use the states at the L points to label the states on the Fermi surfaces). We first establish four local reference frames with L_m as the coordinate origin and ΓL_m as the z axis shown in Fig. 10. The axes of the local reference frame at L_1 written in the global reference frame are defined as

$$
\begin{aligned}
\boldsymbol{x} &= \left(\frac{\sqrt{2}}{2},-\frac{\sqrt{2}}{2},0\right)^{\mathsf{T}}\\
\boldsymbol{y} &= \left(\frac{\sqrt{6}}{6},\frac{\sqrt{6}}{6},-\sqrt{\frac{2}{3}}\right)^{\mathsf{T}}\\
\boldsymbol{z} &= \left(\sqrt{\frac{1}{3}},\sqrt{\frac{1}{3}},\sqrt{\frac{1}{3}}\right)^{\mathsf{T}},
\end{aligned}
$$

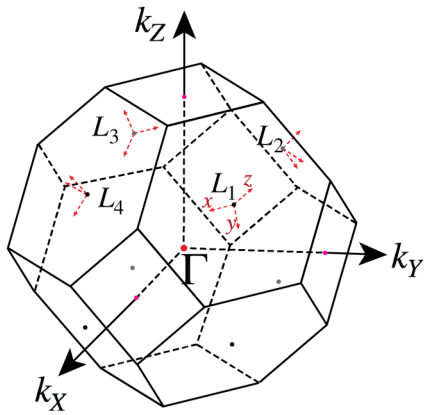

FIG. 10. The local reference coordinates on four L points.

and the other three coordinates of the local reference frames can be obtained by taking the C_4 (defined along the k_Z axis) rotation on the first one. We transform the states created by the operator $\hat{\psi}^{\dagger}(\boldsymbol{k}+\mathbf{L}_m)$ in the global reference frame to the states created by the operator $\hat{\phi}^{\dagger}(\boldsymbol{k})$ in the local reference frames by the operator $\hat{U}_m$, and $\hat{\psi}_l^{\dagger}(\boldsymbol{k}+\mathbf{L}_m)=\hat{U}_m\hat{\phi}_{m,l}^{\dagger}(\boldsymbol{k})\hat{U}_m^{\dagger}=\sum_w \mathcal{U}_{wl}^m\hat{\phi}_{m,w}^{\dagger}(\boldsymbol{k})$ and $\hat{\psi}_l(\boldsymbol{k}+\mathbf{L}_m)=\hat{U}_m\hat{\phi}_{m,l}(\boldsymbol{k})\hat{U}_m^{\dagger}=\sum_w \mathcal{U}_{wl}^{m*}\hat{\phi}_{m,w}(\boldsymbol{k})$. For the intrapocket interaction, $m=n$, the density operator is transformed as

$$
\begin{aligned}
\hat{\rho}_{\tilde{\boldsymbol{q}},mm} &= \widetilde{\sum_{\boldsymbol{k},l}}\hat{\psi}_l^{\dagger}(\boldsymbol{k}+\tilde{\boldsymbol{q}}+\mathbf{L}_m)\hat{\psi}_l(\boldsymbol{k}+\mathbf{L}_m)\\
&= \widetilde{\sum_{\boldsymbol{k},l}}\hat{U}_m\hat{\phi}_{m,l}^{\dagger}(\boldsymbol{k}+\tilde{\boldsymbol{q}})\hat{U}_m^{\dagger}\hat{U}_m\hat{\phi}_{n,l}(\boldsymbol{k})\hat{U}_m^{\dagger}\\
&= \widetilde{\sum_{\boldsymbol{k},l,w,v}}\mathcal{U}_{wl}^m\mathcal{U}_{vl}^{m*}\hat{\phi}_{m,w}^{\dagger}(\boldsymbol{k}+\tilde{\boldsymbol{q}})\hat{\phi}_{n,v}(\boldsymbol{k})\\
&= \widetilde{\sum_{\boldsymbol{k},w}}\hat{\phi}_{m,w}^{\dagger}(\boldsymbol{k}+\tilde{\boldsymbol{q}})\hat{\phi}_{m,w}(\boldsymbol{k}).
\end{aligned}
\tag{D1}
$$

We use the fact that the similarity transformation matrix $\mathcal{U}^m$ is unitary and $\sum_l \mathcal{U}_{wl}^m\mathcal{U}_{vl}^{m*}=\delta_{wv}$. For the interpocket interaction, $m\neq n$, and we have

$$
\begin{aligned}
\hat{\rho}_{\tilde{\boldsymbol{q}},mn} &= \widetilde{\sum_{\boldsymbol{k},l}}\hat{\psi}_l^{\dagger}(\boldsymbol{k}+\tilde{\boldsymbol{q}}+\mathbf{L}_m)\hat{\psi}_l(\boldsymbol{k}+\mathbf{L}_n)\\
&= \widetilde{\sum_{\boldsymbol{k},l}}\hat{U}_m\hat{\phi}_{m,l}^{\dagger}(\boldsymbol{k}+\tilde{\boldsymbol{q}})\hat{U}_m^{\dagger}\hat{U}_n\hat{\phi}_{n,l}(\boldsymbol{k})\hat{U}_n^{\dagger}\\
&= \widetilde{\sum_{\boldsymbol{k},l,w,v}}\mathcal{U}_{wl}^m\mathcal{U}_{vl}^{n*}\hat{\phi}_{m,w}^{\dagger}(\boldsymbol{k}+\tilde{\boldsymbol{q}})\hat{\phi}_{n,v}(\boldsymbol{k})\\
&= \widetilde{\sum_{\boldsymbol{k},w,v}}\mathcal{D}_{wv}^{mn}\hat{\phi}_{m,w}^{\dagger}(\boldsymbol{k}+\tilde{\boldsymbol{q}})\hat{\phi}_{n,v}(\boldsymbol{k}),
\end{aligned}
\tag{D2}
$$

where the matrix $\mathcal{D}^{mn}$ can be obtained by the following two steps. (i) The representation of the density operator $\hat{\rho}_{\tilde{\boldsymbol{q}},mn}$ is an identity matrix in the global reference frame and is invariant under the similarity transformation. We take a rotation on the global referencee frame and make the directions of the axes coinciding with the local reference frame at L_1.

(ii) We take C_4 rotation to transform the orbitals defined in the reference coordinates of the local reference frame at L_1 to the orbitals in the local reference frames at L_m and L_n. The matrix $\mathcal{U}^m$ can be obtained as $\mathcal{U}^m = e^{-\frac{i}{2}(m-1)\frac{\pi}{2}\boldsymbol{\sigma}\cdot\hat{\boldsymbol{z}}} \otimes e^{-i(m-1)\frac{\pi}{2}\boldsymbol{s}\cdot\hat{\boldsymbol{z}}}$. $\boldsymbol{\sigma} = (\sigma_x, \sigma_y, \sigma_z)$, $\boldsymbol{s} = (s_x, s_y, s_z)$. $\sigma_{x,y,z}$ and $s_{x,y,z}$ are the generators of SU(2) and SO(3) group, respectively. $\hat{\boldsymbol{z}}$ is the unit vector in the direction of the k_Z axis in the local reference frame $\hat{\boldsymbol{z}} = (0, -\sqrt{\frac{2}{3}}, \sqrt{\frac{1}{3}})^\intercal$. The matrix $\mathcal{D}^{mn}$ is obtained as $\mathcal{D}^{mn} = \mathcal{U}^m \mathcal{U}^{n\dagger}$. The interaction under the basis of the four local reference frames is obtained as

$$H_{\text{int}} = \sum_{m\tilde{\boldsymbol{q}}\boldsymbol{k}l_1l_2} \hat{\phi}^\dagger_{m,\boldsymbol{k}+\tilde{\boldsymbol{q}},l_1}\hat{\phi}^\dagger_{m,-\boldsymbol{k}-\tilde{\boldsymbol{q}},l_2}\hat{\phi}_{m,-\boldsymbol{k},l_2}\hat{\phi}_{m,\boldsymbol{k},l_1}[U_0 + U_1 f_1(\tilde{\boldsymbol{q}}) + U_2 f_2(\tilde{\boldsymbol{q}})]$$
$$+ \sum_{\tilde{\boldsymbol{q}}\boldsymbol{k}mn}\sum_{w_1w_2v_1v_2} \mathcal{D}^{mn}_{w_1v_1}\mathcal{D}^{mn}_{w_2v_2}\hat{\phi}^\dagger_{m,\boldsymbol{k}+\tilde{\boldsymbol{q}},w_1}\hat{\phi}^\dagger_{m,-\boldsymbol{k}-\tilde{\boldsymbol{q}},w_2}\hat{\phi}_{n,-\boldsymbol{k},v_2}\hat{\phi}_{n,\boldsymbol{k},v_1}[U_0 + U_1 f_1(\tilde{\boldsymbol{q}} + \mathbf{L}_{mn}) + U_2 f_2(\tilde{\boldsymbol{q}} + \mathbf{L}_{mn})]. \quad \text{(D3)}$$

For the next step, we transform the orbital w_1, w_2, v_1, and v_2 in the local reference frames to the eigenstates of the C_3 rotation (defined along ΓL_m) with eigenvaules $j_z = \pm\frac{1}{2}$, including $|J = \frac{3}{2}, j_z = \pm\frac{1}{2}\rangle$, $|J = \frac{1}{2}, j_z = \pm\frac{1}{2}\rangle$ on each pocket. The relations between the orbital basis and angular momentum basis can be obtained by Clebsch-Gordan coefficients

$$\left|J = \frac{1}{2}, j_z = \frac{1}{2}\right\rangle = -\frac{1}{\sqrt{3}}|p_z, \uparrow\rangle - \frac{1}{\sqrt{3}}|p_x, \downarrow\rangle - \frac{i}{\sqrt{3}}|p_y, \downarrow\rangle,$$
$$\left|J = \frac{3}{2}, j_z = \frac{1}{2}\right\rangle = \sqrt{\frac{2}{3}}|p_z, \uparrow\rangle - \frac{1}{\sqrt{6}}|p_x, \downarrow\rangle - \frac{i}{\sqrt{6}}|p_y, \downarrow\rangle,$$
$$\left|J = \frac{1}{2}, j_z = -\frac{1}{2}\right\rangle = \frac{1}{\sqrt{3}}|p_z, \downarrow\rangle - \frac{1}{\sqrt{3}}|p_x, \uparrow\rangle + \frac{i}{\sqrt{3}}|p_y, \uparrow\rangle,$$
$$\left|J = \frac{3}{2}, j_z = -\frac{1}{2}\right\rangle = \sqrt{\frac{2}{3}}|p_z, \downarrow\rangle + \frac{1}{\sqrt{6}}|p_x, \uparrow\rangle - \frac{i}{\sqrt{6}}|p_y, \uparrow\rangle. \quad \text{(D4)}$$

We obtain the interaction in the angular momentum basis as

$$H_{\text{int}} = \sum_{m\tilde{\boldsymbol{q}}\boldsymbol{k}t_1t_2} \hat{\phi}^\dagger_{m,\boldsymbol{k}+\tilde{\boldsymbol{q}},t_1}\hat{\phi}^\dagger_{m,-\boldsymbol{k}-\tilde{\boldsymbol{q}},t_2}\hat{\phi}_{m,-\boldsymbol{k},t_2}\hat{\phi}_{m,\boldsymbol{k},t_1}[U_0 + U_1 f_1(\tilde{\boldsymbol{q}}) + U_2 f_2(\tilde{\boldsymbol{q}})]$$
$$+ \sum_{\tilde{\boldsymbol{q}}\boldsymbol{k}mn}\sum_{w_1w_2v_1v_2}\sum_{t_1t_2r_1r_2} \mathcal{G}^*_{w_1t_1}\mathcal{D}^{mn}_{w_1v_1}\mathcal{G}_{v_1r_1}\mathcal{G}^*_{w_2t_2}\mathcal{D}^{mn}_{w_2v_2}\mathcal{G}_{v_2t_2}\hat{\phi}^\dagger_{m,\boldsymbol{k}+\tilde{\boldsymbol{q}},t_1}\hat{\phi}^\dagger_{m,-\boldsymbol{k}-\tilde{\boldsymbol{q}},t_2}\hat{\phi}_{n,-\boldsymbol{k},r_2}\hat{\phi}_{n,\boldsymbol{k},r_1}[U_0 + U_1 f_1(\boldsymbol{q}) + U_2 f_2(\boldsymbol{q})], \quad \text{(D5)}$$

where the indices $t_{1,2}, r_{1,2} = 1, 2, 3, 4$ denote the basis $|J = \frac{1}{2}, j_z = \frac{1}{2}\rangle$, $|J = \frac{3}{2}, j_z = \frac{1}{2}\rangle$, $|J = -\frac{1}{2}, j_z = \frac{1}{2}\rangle$, and $|J = \frac{3}{2}, j_z = -\frac{1}{2}\rangle$, respectively. $\mathcal{G}_{w_1't_1}$ is the transformation coefficient with $w_1' = 1, 2, 3, 4, 5, 6$ indicating the orbitals in the local reference frame $(\uparrow, \downarrow) \otimes (p_x, p_y, p_z)$:

$$\mathcal{G} = \begin{pmatrix} 0 & 0 & -\frac{1}{\sqrt{3}} & \frac{1}{\sqrt{6}} \\ 0 & 0 & \frac{i}{\sqrt{3}} & -\frac{i}{\sqrt{6}} \\ -\frac{1}{\sqrt{3}} & \sqrt{\frac{2}{3}} & 0 & 0 \\ -\frac{1}{\sqrt{3}} & -\frac{1}{\sqrt{6}} & 0 & 0 \\ -\frac{i}{\sqrt{3}} & -\frac{i}{\sqrt{6}} & 0 & 0 \\ 0 & 0 & \frac{1}{\sqrt{3}} & \sqrt{\frac{2}{3}} \end{pmatrix}. \quad \text{(D6)}$$

We can simplify the interaction as

$$H_{\text{int}} = \sum_{m\tilde{\boldsymbol{q}}\boldsymbol{k}t_1t_2} \hat{\phi}^\dagger_{m,\boldsymbol{k}+\tilde{\boldsymbol{q}},t_1}\hat{\phi}^\dagger_{m,-\boldsymbol{k}-\tilde{\boldsymbol{q}},t_2}\hat{\phi}_{m,-\boldsymbol{k},t_2}\hat{\phi}_{m,\boldsymbol{k},t_1}[U_0 + U_1 f_1(\tilde{\boldsymbol{q}}) + U_2 f_2(\tilde{\boldsymbol{q}})]$$
$$+ \sum_{\tilde{\boldsymbol{q}}\boldsymbol{k}mn}\sum_{t_1t_2r_1r_2} (\mathcal{G}^\dagger\mathcal{D}^{mn}\mathcal{G})_{t_1r_1}(\mathcal{G}^\dagger\mathcal{D}^{mn}\mathcal{G})_{t_2r_2}\hat{\phi}^\dagger_{m,\boldsymbol{k}+\tilde{\boldsymbol{q}},t_1}\hat{\phi}^\dagger_{m,-\boldsymbol{k}-\tilde{\boldsymbol{q}},t_2}\hat{\phi}_{n,-\boldsymbol{k},r_2}\hat{\phi}_{n,\boldsymbol{k},r_1}[U_0 + U_1 f_1(\boldsymbol{q}) + U_2 f_2(\boldsymbol{q})]. \quad \text{(D7)}$$

Based on the effective Hamiltonian H_{mix} on the Fermi surface introduced in the main text, we take the two eigenstates $|j_z = \pm\frac{1}{2}\rangle_2$ as the states on the Fermi pockets. Finally, we project the interaction in the global reference frame onto the four Fermi surfaces

and obtain

$$H_{\rm int} = \sum_{m\tilde{\boldsymbol{q}}\boldsymbol{k}d_1d_2} \hat{c}^\dagger_{m,\boldsymbol{k}+m\tilde{,}\boldsymbol{q},d_1}\hat{c}^\dagger_{m,-\boldsymbol{k}-\tilde{\boldsymbol{q}},d_2}\hat{c}_{m,-\boldsymbol{k},d_2}\hat{c}_{m,\boldsymbol{k},d_1}[U_0+U_1f_1(\tilde{\boldsymbol{q}})+U_2f_2(\tilde{\boldsymbol{q}})]$$
$$+\sum_{\tilde{\boldsymbol{q}}\boldsymbol{k}mn}\sum_{d_1d_2g_1g_2}(\mathcal{M}^\dagger\mathcal{G}^\dagger\mathcal{D}^{mn}\mathcal{G}\mathcal{M})_{d_1g_1}(\mathcal{M}^\dagger\mathcal{G}^\dagger\mathcal{D}^{mn}\mathcal{G}\mathcal{M})_{d_2g_2}\hat{c}^\dagger_{m,\boldsymbol{k}+\tilde{\boldsymbol{q}},d_1}\hat{c}^\dagger_{m,-\boldsymbol{k}-\tilde{\boldsymbol{q}},d_2}\hat{c}_{n,-\boldsymbol{k},g_2}\hat{c}_{n,\boldsymbol{k},g_1}[U_0+U_1f_1(\boldsymbol{q})+U_2f_2(\boldsymbol{q})]. \quad \text{(D8)}$$

Here we use $\hat{c}_{m,\boldsymbol{k},d}$ to denote the states on the mth Fermi pocket with pseudospin $d =\uparrow (\downarrow)$. $\mathcal{M}$ is composed by the eigenstates on the Fermi surfaces $|j_z = \pm\frac{1}{2}\rangle_2$,

$$\mathcal{M} = \begin{pmatrix} \cos\frac{\theta}{2} & 0 \\ \sin\frac{\theta}{2} & 0 \\ 0 & -\cos\frac{\theta}{2} \\ 0 & \sin\frac{\theta}{2} \end{pmatrix}. \quad \text{(D9)}$$

APPENDIX E: INDUCING IRREPS OF POINT GROUP O_h FROM POINT GROUP D_{3d}

The point group O_h is the semidirect product of point group D_{3d} and the fourfold cyclic group $\{C_4, C_4^2, C_4^3, C_4^4\}$, which means $O_h = \{D_{3d}, C_4D_{3d}, C_4^2D_{3d}, C_4^3D_{3d}\} = \{D_{3d}, D_{3d}C_4, D_{3d}C_4^2, D_{3d}C_4^3\}$. We can obtain that for any element R_1 in the point group D_{3d}, we can always find another element R_2 also in D_{3d} which satisfies $R_1C_4^\alpha = C_4^\beta R_2$. Namely, for a given α we can find a β satisfying the relation

$$\forall\,\alpha\in\{1,2,3,4\},\quad R_1\in D_{3d},\quad \exists\beta\in 1,2,3,4,$$
$$R_2\in D_{3d},\quad R_1C_4^\alpha = C_4^\beta R_2. \quad \text{(E1)}$$

In the point group D_{3d}, there are three C_2 rotation symmetries denoted as C_{2a}, C_{2b}, and C_{2c}. The axis of C_{2a} coincides with the x axis in the local reference frame. The axes of C_{2b} and C_{2c} are obtained by acting the C_3 rotation (along ΓL) on the axis of C_{2a}. We take one element from each class of D_{3d}, C_3, and C_{2a} to show the relations in Eq. (E1):

$$C_3C_4 = {C_4}^3C_3^2,\quad C_3{C_4}^2 = C_4C_{2b},\quad C_3{C_4}^3 = {C_4}^2C_{2c}, \quad \text{(E2)}$$

$$C_{2a}C_4 = {C_4}^3C_{2a}^2,\quad C_{2a}{C_4}^2 = C_4^2C_{2a},\quad C_{2a}{C_4}^3 = C_4C_{2a}. \quad \text{(E3)}$$

The other symmetries can be analyzed similarly. In the main text, we have already shown the irreps basis of D_{3d} denoted as $\hat{\delta}_{\iota,\eta}$. The index ι indicates the irreps and η indicates the component of the irreps. For the one-dimensional irreps like $a_{1g(u)}$ and $a_{2g(u)}$, $\eta = 1$, while for $e_{u(g)}$, $\eta = 1, 2$. For the element R in the group D_{3d}, we have

$$R\hat{\delta}_{\iota,\eta_1} = \sum_{\eta_2}\hat{\delta}_{\eta_2}\mathcal{R}_\iota(R)_{\eta_2\eta_1}, \quad \text{(E4)}$$

where $\mathcal{R}_\iota(R)$ is the irreps matrix of the element R. Now we add a superscript m on the irreps basis, i.e., $\hat{\delta}^m_{\iota,\eta}$, to denote $\hat{\delta}_{\iota,\eta}$ on the Fermi pocket at L_m. In the last section, we act C_4 rotation on the first local reference frame directly to obtain the other three. Similarly, we have $C_4^i\hat{\delta}^m_{\iota,\eta} = \hat{\delta}^{(m+i)\bmod 4}_{\iota,\eta}$. We can obtain the representations of C_4 and C_4^2 in the equation below:

$$\mathbb{R}_\iota(C_4) = \begin{pmatrix} 0 & 0 & 0 & \mathcal{I}_\iota \\ \mathcal{I}_\iota & 0 & 0 & 0 \\ 0 & \mathcal{I}_\iota & 0 & 0 \\ 0 & 0 & \mathcal{I}_\iota & 0 \end{pmatrix},$$
$$\mathbb{D}(C_4^2) = \begin{pmatrix} 0 & 0 & \mathcal{I}_\iota & 0 \\ 0 & 0 & 0 & \mathcal{I}_\iota \\ \mathcal{I}_\iota & 0 & 0 & 0 \\ 0 & \mathcal{I}_\iota & 0 & 0 \end{pmatrix}, \quad \text{(E5)}$$

where we use $\mathcal{I}_\iota$ to denote the identity matrix with the same dimension as the irreps of D_{3d} indicated by ι. Based on Eqs. (E2), (E3), and (E4), we can induce the representations of group O_h based on the irreps basis of group D_{3d}, $\{\hat{\delta}^1_\iota, \hat{\delta}^2_\iota, \hat{\delta}^3_\iota, \hat{\delta}^4_\iota\}$, where the index η is suppressed and $\hat{\delta}^m_\iota$ denotes the vector $\{\hat{\delta}^m_{\iota,1},\ldots,\hat{\delta}^m_{\iota,\eta}\}$:

$$\begin{aligned} C_3\hat{\delta}^1_\iota &= \hat{\delta}^1_\iota\mathcal{R}_\iota(C_3),\\ C_3\hat{\delta}^2_\iota &= C_3C_4\hat{\delta}^1_\iota = C_4^3C_3^2\hat{\delta}^1_\iota\\ &= C_4^3\hat{\delta}^1_\iota\mathcal{R}_\iota(C_3^2) = \hat{\delta}^4_\iota\mathcal{R}_\iota(C_3^2),\\ C_3\hat{\delta}^3_\iota &= C_3C_4^2\hat{\delta}^1_\iota = C_4C_{2b}\hat{\delta}^1_\iota\\ &= C_4\hat{\delta}^1_\iota\mathcal{R}_\iota(C_{2b}) = \hat{\delta}^2_\iota\mathcal{R}_\iota(C_{2b}),\\ C_3\hat{\delta}^4_\iota &= C_3C_4^3\hat{\delta}^1_\iota = C_4^2C_{2c}\hat{\delta}^1_\iota\\ &= C_4^2\hat{\delta}^1_\iota\mathcal{R}_\iota(C_{2c}) = \hat{\delta}^3_\iota\mathcal{R}_\iota(C_{2c}), \end{aligned} \quad \text{(E6)}$$

and, similarly, for C_{2a} we have

$$\begin{aligned} C_{2a}\hat{\delta}^1_\iota &= \hat{\delta}^1_\iota\mathcal{R}_\iota(C_{2a}),\\ C_{2a}\hat{\delta}^2_\iota &= C_{2a}C_4\hat{\delta}^1_\iota = C_4^3C_{2a}\hat{\delta}^1_\iota\\ &= C_4^3\hat{\delta}^1_\iota\mathcal{R}_\iota(C_{2a}) = \hat{\delta}^4_\iota\mathcal{R}_\iota(C_{2a}),\\ C_{2a}\hat{\delta}^3_\iota &= C_{2a}C_4^2\hat{\delta}^1_\iota = C_4^2C_{2a}\hat{\delta}^1_\iota\\ &= C_4^2\hat{\delta}^1_\iota\mathcal{R}_\iota(C_{2a}) = \hat{\delta}^3_\iota\mathcal{R}_\iota(C_{2b}),\\ C_{2a}\hat{\delta}^4_\iota &= C_{2a}C_4^3\hat{\delta}^1_\iota = C_4C_{2a}\hat{\delta}^1_\iota\\ &= C_4\hat{\delta}^1_\iota\mathcal{R}_\iota(C_{2a}) = \hat{\delta}^2_\iota\mathcal{R}_\iota(C_{2a}). \end{aligned} \quad \text{(E7)}$$

With the two equations in the above, we can obtain the induced representation of C_3 and C_{2a} in group O_h as

$$\mathbb{R}_\iota(C_3) = \begin{pmatrix} \mathcal{R}_\iota(C_3) & 0 & 0 & 0 \\ 0 & 0 & \mathcal{R}_\iota(C_{2b}) & 0 \\ 0 & 0 & 0 & \mathcal{R}_\iota(C_{2c}) \\ 0 & \mathcal{R}_\iota(C_3^2) & 0 & 0 \end{pmatrix}, \quad \text{(E8)}$$

TABLE IX. The irreps matrices of point group D_{3d}.

	C_3	C_3^2	C_{2a}	C_{2b}	C_{2c}
$a_{1g(u)}$	1	1	1	1	1
$a_{2g(u)}$	1	1	−1	−1	−1
$e_{g(u)}$	$\begin{pmatrix} -\frac{1}{2} & -\frac{\sqrt{3}}{2} \\ \frac{\sqrt{3}}{2} & -\frac{1}{2} \end{pmatrix}$	$\begin{pmatrix} -\frac{1}{2} & \frac{\sqrt{3}}{2} \\ -\frac{\sqrt{3}}{2} & -\frac{1}{2} \end{pmatrix}$	$\begin{pmatrix} 1 & 0 \\ 0 & -1 \end{pmatrix}$	$\begin{pmatrix} -\frac{1}{2} & -\frac{\sqrt{3}}{2} \\ -\frac{\sqrt{3}}{2} & \frac{1}{2} \end{pmatrix}$	$\begin{pmatrix} -\frac{1}{2} & \frac{\sqrt{3}}{2} \\ \frac{\sqrt{3}}{2} & \frac{1}{2} \end{pmatrix}$

$$\mathbb{R}_\iota(C_{2a}) = \begin{pmatrix} \mathcal{R}_\iota(C_{2a}) & 0 & 0 & 0 \\ 0 & 0 & 0 & \mathcal{R}_\iota(C_{2a}) \\ 0 & 0 & \mathcal{R}_\iota(C_{2a}) & 0 \\ 0 & \mathcal{R}_\iota(C_{2a}) & 0 & 0 \end{pmatrix}. \tag{E9}$$

We use $\mathbb{R}_\iota(R)$ to denote the representations of O_h and all of the irreps of D_{3d}, $\mathcal{R}_\iota(R)$, are listed in Table IX. So far, we have obtained the induced representations of C_3, C_{2a}, C_4, and C_4^2 which belong to different classes in group O_h. The induced representations are not irreps apparently and we decompose the induced representations into the irreps in the form of the equation

$$X\mathbb{R}_\iota(R)X^\dagger = \bigoplus_\epsilon \left(\bigoplus_{c_\epsilon} \mathcal{R}_\epsilon(R) \right), \tag{E10}$$

where X is a similarity transformation matrix and c_ϵ denotes how many times the irrep $\mathcal{R}_\epsilon(R)$ appear in the decomposition with ϵ indicating the irreps of O_h. c_ϵ can be obtained as $c_\epsilon = \sum_{R\in O_h} \frac{1}{g}\chi_\epsilon(R)^*\chi(R)$. g is the order of the group which equals to 48 for O_h. $\chi_\epsilon(R)$ is the character of the irreps of the element R and $\chi(R)$ is the character of $\mathbb{R}_\iota$. At last, we decompose the induced representations as follows:

$$\begin{aligned} X_1\mathbb{R}_{a_{1u(g)}}(R)X_1^\dagger &= \mathcal{R}_{A_{1u(g)}}(R) \oplus \mathcal{R}_{T_{2u(g)}}(R), \\ X_2\mathbb{R}_{a_{2u(g)}}(R)X_2^\dagger &= \mathcal{R}_{A_{2u(g)}}(R) \oplus \mathcal{R}_{T_{1u(g)}}(R), \\ X_3\mathbb{R}_{e_{u(g)}}(R)X_3^\dagger &= \mathcal{R}_{E_{u(g)}}(R) \oplus \mathcal{R}_{T_{1u(g)}}(R) \oplus \mathcal{R}_{T_{2u(g)}}(R). \end{aligned} \tag{E11}$$

We use $a_{1u(g)}$, $a_{2u(g)}$, and $e_{u(g)}$ to denote irreps of D_{3d} distinguishing with the irreps of O_h written as $A_{1u(g)}$, $A_{2u(g)}$, $E_{u(g)}$, $T_{1u(g)}$, and $T_{2u(g)}$. The similarity matrices $X_{1,2,3}$ can be solved out to obtain the induced irreps basis of group O_h which are shown explicitly in the main text.

APPENDIX F: SINGLET STATES EXCLUDED FROM OUR CONSIDERATION

In Eq. (4), we expand the interaction to the second order of $\tilde{\boldsymbol{q}}$. The interaction in the zeroth order has the pairing function as a constant and is decomposed into a trivial channel $\hat{\delta}^\dagger_{a_{1g}}\hat{\delta}_{a_{1g}}$. After we introduce $\boldsymbol{k}$ and $\boldsymbol{k}'$ in Appendix C, the interaction in the second order of $\tilde{q}$ can be written as $\tilde{\boldsymbol{q}}^2 = \boldsymbol{k}^2 + \boldsymbol{k}'^2 - 2\boldsymbol{k}\boldsymbol{k}'$. Among the three terms, $\boldsymbol{k}^2$ and $\boldsymbol{k}'^2$ provide the even-parity pairing, and in the even-parity pairing channels the interaction can be decomposed as $\hat{\delta}^\dagger_\epsilon\hat{\delta}_{a_{1g}} + \text{H.c}$. The irrep a_{1g} can only induce the A_{1g} and T_{2g} irreps of group O_h. Therefore, the even-parity pairing channels can be only A_{1g} and T_{2g}. Moreover, both the A_{1g} and T_{2g} pairing states are topologically trivial.

We assume the onsite interaction strength $|U_0|$ much bigger than the other two, $|U_0| \gg |U_1|, |U_2|$. When the onsite interaction is attractive, i.e., $U_0 < 0$, the interaction in Eq. (D8) is domained by the term in the zeroth order of $\boldsymbol{k}$. The intrapocket interaction can be decomposed as

$$X_1 \bigoplus_m (\hat{\delta}^{m\dagger}_{a_{1g}}\hat{\delta}^m_{a_{1g}})X_1^\dagger = \hat{\Delta}^\dagger_{A_{1g}}\hat{\Delta}_{A_{1g}} \oplus \hat{\Delta}^\dagger_{T_{2g}}\hat{\Delta}_{T_{2g}}. \tag{F1}$$

Thus, when $U_0 < 0$, the ground state is dominated by the topologically trivial channels.

For the repulsive onsite interaction, $U_0 > 0$, the zeroth-order interaction (U_0 dominates U_1 and U_2) are positive which cannot support superconductivity on the mean-field level. We then expand the interaction to the second order of $\boldsymbol{k}$. Here, we use $\hat{\Delta}^0_{A_{1g}}$ and $\hat{\Delta}^0_{T_{2g}}$ to denote the basis composed by the pairing function in the zeroth order of $\boldsymbol{k}$ and $\hat{\Delta}^2_{A_{1g}}$ and $\hat{\Delta}^2_{T_{2g}}$ to denote the basis composed by the pairing function in the second order of $\boldsymbol{k}$. The interaction decomposed into A_{1g} channel can be written as

$$H_{\text{int}} = (\hat{\Delta}^{0\dagger}_{A_{1g}}, \hat{\Delta}^{2\dagger}_{A_{1g}}) \begin{pmatrix} h_0(\theta, U_0) & h(\theta, U_1, U_2) \\ h(\theta, U_1, U_2)^* & 0 \end{pmatrix} \begin{pmatrix} \hat{\Delta}^0_{A_{1g}} \\ \hat{\Delta}^2_{A_{1g}} \end{pmatrix}, \tag{F2}$$

where $h_0(\theta, U_0) = 3 + \frac{1}{12}[4\cos(\theta) + 3\cos(2\theta) + 5]$ obtained in the former sections and $|h(\theta, U_1, U_2)| \ll |h_0(\theta, U_0)|$. We diagonalize H_{int} matrix and obtain the coefficient for each A_{1g} channel as $\frac{h_0(\theta,U_0)}{2} \pm \sqrt{\frac{h_0(\theta,U_0)^2}{4} + |h(\theta, U_1, U_2)|^2}$, in which only one is negative but close to zero, $\lim_{|h(\theta,U_1,U_2)|\ll|h_0(\theta,U_0)|} \frac{h_0(\theta,U_0)}{2} - \sqrt{\frac{h_0(\theta,U_0)^2}{4} + |h(\theta, U_1, U_2)|^2} = -|\frac{h(\theta,\ U_1,\ U_2)}{h_0(\theta,U_0)}||h(\theta, U_1, U_2)| \sim 0$. The analysis for the T_{2g} channel is similar to A_{1g}. Therefore, the onsite repulsive interaction excludes the spin-singlet pairing states.

APPENDIX G: MEAN-FIELD APPROXIMATION CALCULATION

We use Δ to denote the superconducting gap and μ to denote the chemical potential. In the weak-pairing limit, we only consider the electronic states within a shell near the Fermi surfaces. We take the thickness of the shell as $2\delta\mu$, i.e., $\mu - \delta\mu < \frac{k_x^2+k_y^2}{2m} + \frac{\xi k_z^2}{2m} < \mu + \delta\mu$. Moreover, in the weak-pairing limit it requires

$$\Delta \ll \delta\mu \ll \mu. \tag{G1}$$

The pairing part of the BdG Hamiltonian is written as

$$\begin{aligned} H_{\text{pairing}} = (\hat{c}_{\boldsymbol{k},\uparrow}, \hat{c}_{\boldsymbol{k},\downarrow})[&id_1(\boldsymbol{k})\sigma_1\sigma_2 + id_2(\boldsymbol{k})\sigma_2\sigma_2 \\ &+ id_3(\boldsymbol{k})\sigma_3\sigma_2] \begin{pmatrix} \hat{c}_{-\boldsymbol{k},\uparrow} \\ \hat{c}_{-\boldsymbol{k},\downarrow} \end{pmatrix} + \text{H.c.}, \end{aligned} \tag{G2}$$

where σ are the Pauli matrices. For the spin-triplet states from the interaction expanded to the second order of $\boldsymbol{k}$, $d_{1,2,3}(\boldsymbol{k})$ are linear functions of $\boldsymbol{k}$. In the spherical coordinates, $\boldsymbol{k} = k(\sin\theta\cos\phi, \sin\theta\sin\phi, \cos\theta)$, and the linear function $d_{1,2,3}(\boldsymbol{k})$ can be written as $kd_{1,2,3}(\theta, \phi)$, where k is the magnitude of $\boldsymbol{k}$. We also write $d_i(\theta, \phi)$ into the vector form $\boldsymbol{d} = (d_1(\theta, \phi), d_2(\theta, \phi), d_3(\theta, \phi))$. The dispersion of the BdG

Hamiltonian can be obtained as

$$E(k,\theta,\phi)=\pm\sqrt{\left(\frac{g(\theta,\phi)}{2m}k^2-\mu\right)^2+k^2\boldsymbol{d}^2\pm 2k^2\sqrt{[\mathrm{Re}\,(\boldsymbol{d})\times\mathrm{Im}\,(\boldsymbol{d})]\cdot[\mathrm{Re}\,(\boldsymbol{d})\times\mathrm{Im}\,(\boldsymbol{d})]}}. \tag{G3}$$

In the equation above, $g(\theta,\phi)=\sin\theta^2+\xi\cos\theta^2$. ξ is used to depict the anisotropy of the Fermi surfaces. For simplicity, we suppress the variables θ, ϕ and write $g(\theta,\phi)$ and $d_i(\theta,\phi)$ as g and d_i in the following calculation. When the d_i function has the same phase, $\arg(d_1)=\arg(d_2)=\arg(d_3)$, we have $\mathrm{Re}(\boldsymbol{d})\times\mathrm{Im}(\boldsymbol{d})=0$. In this condition, the system has lower free energy and the time-reversal symmetry is respected. We take a gauge where $\arg(d_1)=\arg(d_2)=\arg(d_3)=0$. Namely, d_1, d_2, and d_3 are all real and the dispersion takes the form as

$$E(k,\theta,\phi)=\pm\sqrt{\left(\frac{g(\theta,\phi)}{2m}k^2-\mu\right)^2+k^2\boldsymbol{d}^2}. \tag{G4}$$

We integrate the negative eigenvaules within a shell (with a thickness of $\delta\mu$) near the four Fermi surfaces to obtain the free energy. The free energy saved in the superconducting state is

$$\Delta E=\int d\Omega\int_{\frac{g}{2m}k^2=\mu-\delta\mu}^{\frac{g}{2m}k^2=\mu+\delta\mu}\rho_{\boldsymbol{k}}k^2dk\left(\sqrt{\left(\frac{g}{2m}k^2-\mu\right)^2+\boldsymbol{d}^2k^2}-\left|\frac{g}{2m}k^2-\mu\right|\right)+\frac{N\lambda^2}{\tilde{f}(U_1,U_2)}, \tag{G5}$$

where Ω stands for the solid angle, $d\Omega=\sin\theta\,d\theta\,d\phi$, and $\rho_{\boldsymbol{k}}$ is the density of the states with respect to $\boldsymbol{k}$ which is treated as a constant in the integral area. In the above equation, λ and $\tilde{f}(U_1,U_2)$ are short for λ_ϵ and $\tilde{f}_\epsilon(U_1,U_2)$, with ϵ labeling the channels with different symmetries. λ_ϵ is the modulus of the vector $\Lambda_\epsilon=(\lambda_{\epsilon,1,1},\ldots,\lambda_{\epsilon,\kappa,\zeta})^{\mathsf{T}}$ obtained from the mean-field approximation, and $\lambda_{\epsilon,\kappa,\zeta}=\frac{1}{N}\sum_{\boldsymbol{k}}\tilde{f}_{\epsilon,\kappa}(U_1,U_2)\hat{\Delta}_{\epsilon,\kappa,\zeta}=\langle\tilde{f}_{\epsilon,\kappa}(U_1,U_2)\hat{\Delta}_{\epsilon,\kappa,\zeta}\rangle$ with $\hat{\Delta}_{\epsilon,\kappa,\zeta}$ being the ζth basis of the κth irrep in the channel ϵ. For example, we totally have 5 T_{2u} and T_{2u} is a three-dimensional irrep. We take $\epsilon=T_{2u}$, $\kappa=1,2,3,4,5$, $\zeta=1,2,3$. In general, $\lambda_{\epsilon,\kappa,\zeta}$ is a complex number. However, due to the time-reversal symmetry, we can choose a gauge where $\lambda_{\epsilon,\kappa,\zeta}$ is real. $\tilde{f}_\epsilon(U_1,U_2)$ is the effective interaction in the corresponding channel, and $\tilde{f}_\epsilon(U_1,U_2)=\lambda_\epsilon^2/\sum_{\kappa,\zeta}\frac{\lambda_{\epsilon,\kappa,\zeta}^2}{\tilde{f}_{\epsilon,\kappa}(U_1,U_2)}$. We write ΔE as $\Delta E'+\frac{\lambda^2}{\tilde{f}(U_1,U_2)}$, with $\Delta E'$ being the integral part in Eq. (G5). We can change the variable k in the integral to $x=k^2$ and obtain

$$\Delta E'=\int d\Omega\int_{\frac{2m}{g}(\mu-\delta\mu)}^{\frac{2m}{g}(\mu+\delta\mu)}\rho_{\boldsymbol{k}}dx\frac{\sqrt{x}}{2}\left(\sqrt{\left(\frac{g}{2m}x-\mu\right)^2+\boldsymbol{d}^2x}-\left|\frac{g}{2m}x-\mu\right|\right). \tag{G6}$$

Then, we substitute x with $\frac{2m\mu}{g}t$,

$$\begin{aligned}\Delta E'&=\int d\Omega\int_{1-\frac{\delta\mu}{\mu}}^{1+\frac{\delta\mu}{\mu}}\rho_{\boldsymbol{k}}dt\frac{(2m)^{\frac{3}{2}}\mu^{\frac{5}{2}}}{2g^{\frac{3}{2}}}\sqrt{t}\left(\sqrt{(t-1)^2+\frac{2m\boldsymbol{d}^2}{g\mu}t}-|t-1|\right)\\&=\int d\Omega\int_{-\frac{\delta\mu}{\mu}}^{\frac{\delta\mu}{\mu}}\rho_{\boldsymbol{k}}dt\frac{(2m)^{\frac{3}{2}}\mu^{\frac{5}{2}}}{2g^{\frac{3}{2}}}\sqrt{t+1}\left(\sqrt{t^2+\frac{2m\boldsymbol{d}^2}{g\mu}(t+1)}-|t|\right).\end{aligned} \tag{G7}$$

According to the relation in Eq. (G1), $\frac{\delta\mu}{\mu}\ll 1$, we have

$$\lim_{t\to 0}\sqrt{t+1}\left(\sqrt{t^2+\frac{2m\boldsymbol{d}^2}{g\mu}(t+1)}-|t|\right)=\sqrt{t^2+\frac{2m\boldsymbol{d}^2}{g\mu}}-|t|. \tag{G8}$$

We substitute Eq. (G8) into (G7) and simplify the integral as

$$\begin{aligned}\Delta E'&=\rho_{\boldsymbol{k}}\int d\Omega\frac{(2m)^{\frac{3}{2}}\mu^{\frac{5}{2}}}{g^{\frac{3}{2}}}\int_0^{\frac{\delta\mu}{\mu}}\left(\sqrt{t^2+\frac{2m\boldsymbol{d}^2}{g\mu}}-t\right)\\&=\rho_{\boldsymbol{k}}\int d\Omega\frac{(2m)^{\frac{3}{2}}\mu^{\frac{5}{2}}}{g^{\frac{3}{2}}}\left[\frac{1}{2}\frac{\delta\mu}{\mu}\sqrt{\frac{2m\boldsymbol{d}^2}{g\mu}+\frac{\delta\mu^2}{\mu^2}}+\frac{1}{2}\frac{2m\boldsymbol{d}^2}{g\mu}\ln\left(\frac{\delta\mu}{\mu}+\sqrt{\frac{2m\boldsymbol{d}^2}{g\mu}+\frac{\delta\mu^2}{\mu^2}}\right)-\frac{1}{4}\frac{2m\boldsymbol{d}^2}{g\mu}\ln\frac{2m\boldsymbol{d}^2}{g\mu}-\frac{1}{2}\frac{\delta\mu^2}{\mu^2}\right].\end{aligned} \tag{G9}$$

We also have $\frac{2m\boldsymbol{d}^2}{g\mu}/\frac{\delta\mu^2}{\mu^2} \ll 1$ derived from

$$\frac{2m\boldsymbol{d}^2}{g\mu}\Big/\frac{\delta\mu^2}{\mu^2} = \frac{2m\boldsymbol{d}^2\mu}{\delta\mu^2 g} = \frac{\boldsymbol{d}^2 k_F^2\mu}{\delta\mu^2\frac{g}{2m}k_F^2} = \frac{\Delta^2\mu}{\delta\mu^2\mu} = \frac{\Delta^2}{\delta\mu^2} \ll 1. \tag{G10}$$

We approximate $\sqrt{\frac{2m\boldsymbol{d}^2}{g\mu}+\frac{\delta\mu^2}{\mu^2}}-\frac{\delta\mu}{\mu}$ as $\frac{1}{2}\frac{2m\boldsymbol{d}^2}{g\delta\mu}$ and $\sqrt{\frac{2m\boldsymbol{d}^2}{g\mu}+\frac{\delta\mu^2}{\mu^2}}+\frac{\delta\mu}{\mu}$ as $2\frac{\delta\mu}{\mu}$, and substitute it into Eq. (G9) obtaining

$$\begin{aligned}\Delta E' &= \int \rho_{\boldsymbol{k}} d\Omega \frac{(2m)^{\frac{3}{2}}\mu^{\frac{5}{2}}}{g^{\frac{3}{2}}}\left[\frac{1}{4}\frac{2m\boldsymbol{d}^2}{g\mu}+\frac{1}{4}\frac{2m\boldsymbol{d}^2}{g\mu}\ln\left(\frac{4g\delta\mu^2}{2m\mu\boldsymbol{d}^2}\right)+0(d^2)\right]\\ &\sim \int \rho_{\boldsymbol{k}} d\Omega \frac{(2m)^{\frac{3}{2}}\mu^{\frac{5}{2}}}{g^{\frac{3}{2}}}\frac{1}{4}\frac{2m\boldsymbol{d}^2}{g\mu}\ln\left(\frac{4g\delta\mu^2}{2m\mu\boldsymbol{d}^2}\right).\end{aligned} \tag{G11}$$

In the second line of the above equation, we adopt the approximation $\ln(\frac{4g\delta\mu^2}{2m\mu\boldsymbol{d}^2}) \gg 1$. g and $\boldsymbol{d}^2$ are the functions of θ and ϕ. Meanwhile, $\boldsymbol{d}$ is the linear function of $\lambda_{\kappa,\zeta}$, i.e., $d_i(\theta,\phi) = \sum_{\kappa,\zeta}\mathcal{A}(\theta,\phi)_{i,\kappa,\zeta}\lambda_{\kappa,\zeta}$. Now, we use one index j to indicate both κ and ζ and simplify the above relation in a vector form $d_i(\theta,\phi) = \sum_j \mathcal{A}(\theta,\phi)_{i,j}\lambda_j$. Accordingly, we have $\boldsymbol{d}(\theta,\phi) = \mathcal{A}(\theta,\phi)\Lambda = \lambda\mathcal{A}(\theta,\phi)\hat{\Lambda}$, where $\hat{\Lambda}$ is a unit vector satisfying $\hat{\Lambda}^\dagger\hat{\Lambda} = 1$. The gap function is obtained as

$$\boldsymbol{d}(\theta,\phi)^2 = \lambda^2\hat{\Lambda}^\dagger\mathcal{A}(\theta,\phi)^\dagger\mathcal{A}(\theta,\phi)\hat{\Lambda}. \tag{G12}$$

We define $\mathbb{A}(\theta,\phi) = \mathcal{A}(\theta,\phi)^\dagger\mathcal{A}(\theta,\phi)$ and substitute Eq. (G12) into (G11) and get

$$\Delta E = -\frac{(2m)^{\frac{5}{2}}\mu^{\frac{3}{2}}\lambda^2\rho_{\boldsymbol{k}}}{4}\ln\frac{m\mu\lambda^2}{2\delta\mu^2}\int d\Omega\frac{1}{g^{\frac{5}{2}}}\hat{\Lambda}^\dagger\mathbb{A}\hat{\Lambda} - \frac{(2m)^{\frac{5}{2}}\mu^{\frac{3}{2}}\lambda^2\rho_{\boldsymbol{k}}}{4}\int d\Omega\frac{1}{g^{\frac{5}{2}}}\hat{\Lambda}^\dagger\mathbb{A}\hat{\Lambda}\ln\frac{\hat{\Lambda}^\dagger\mathbb{A}\hat{\Lambda}}{g} + \frac{N\lambda^2}{\tilde{f}(U_1,U_2)}. \tag{G13}$$

We set $\frac{(2m)^{\frac{5}{2}}\mu^{\frac{3}{2}}}{4}\rho_{\boldsymbol{k}} = \alpha$, $\int d\Omega\frac{1}{g^{\frac{5}{2}}}\hat{\Lambda}^\dagger\mathbb{A}\hat{\Lambda} = A$, $\frac{m\mu}{2\delta\mu^2} = \beta^2$, $\int d\Omega\frac{1}{g^{\frac{5}{2}}}\hat{\Lambda}^\dagger\mathbb{A}\hat{\Lambda}\ln\frac{\hat{\Lambda}^\dagger\mathbb{A}\hat{\Lambda}}{g} = B$, and the equation can be simplified as

$$\Delta E = -2\alpha A\lambda^2\ln\beta\lambda - \alpha B\lambda^2 + \frac{N\lambda^2}{\tilde{f}(U_1,U_2)}. \tag{G14}$$

For a system, ξ, U_1, and U_2 are all determined. ΔE depends on $\boldsymbol{\lambda}$, and the $\boldsymbol{\lambda}$ corresponding to the lowest free energy. i.e., ΔE the biggest, is the ground state. With a certain $\hat{\lambda}$, we can solve A and B for each channel and the maximum of ΔE has λ satisfying $\frac{\partial\Delta E}{\partial\lambda} = 0$:

$$2\alpha A\ln\beta\lambda = \frac{N}{\tilde{f}(U_1,U_2)} - \alpha A - \alpha B. \tag{G15}$$

We substitute the relation into ΔE and obtain

$$\Delta E = \frac{A\alpha}{\beta^2}\exp\left(\frac{N}{A\tilde{f}(U_1,U_2)\alpha} - \frac{B}{A} - 1\right). \tag{G16}$$

In the above equation, we have $\tilde{f}(U_1,U_2)\alpha \sim 0$ derivated as follows:

$$\tilde{f}(U_1,U_2)\alpha = \tilde{f}(U_1,U_2)\frac{(2m)^{\frac{5}{2}}\mu^{\frac{3}{2}}\rho_{\boldsymbol{k}}}{4} = \frac{\tilde{f}(U_1,U_2)k_F^2\rho_{\boldsymbol{k}}mk_F(2m)^{\frac{3}{2}}\mu^{\frac{3}{2}}}{2k_F^3}, \tag{G17}$$

where $\tilde{f}(U_1,U_2)k_F^2$ is the interaction strength expanded to the second order of $\tilde{\boldsymbol{q}}$. We have $\rho_{\boldsymbol{k}}4\pi k^2dk \sim \rho_E dE$ with ρ_E as the density of states about the energy and $dE \sim \frac{k}{m}dk$. Therefore, we can derive $\rho_{\boldsymbol{k}}km \sim \rho_E$. Substitute the relation into the above equation, and we have

$$\tilde{f}(U_1,U_2)\alpha \sim \frac{\tilde{f}(U_1,U_2)k_F^2\rho_{E=\mu}(2m)^{\frac{3}{2}}\mu^{\frac{3}{2}}}{2k_F^3} \sim \frac{\tilde{f}(U_1,U_2)k_F^2\rho_{E=\mu}\mu^{\frac{3}{2}}}{2\mu^{\frac{3}{2}}} \sim \tilde{f}(U_1,U_2)k_F^2\rho_{\mathrm{FS}} \sim 0, \tag{G18}$$

where $\rho_{E=\mu}$ is the density of states at the Fermi surfaces. Constrained by the weak-pairing limit, the production of interaction strength and the density of states is near zero $\tilde{f}(U_1,U_2)k_F^2\rho_{\mathrm{FS}} \sim 0$. We take logarithm on both sides of the equation to compare the saved free energy of each channel:

$$\ln\Delta E = \frac{N}{A\tilde{f}(U_1,U_2)\alpha} - \frac{B}{A} - 1 + \ln\frac{A\alpha}{\beta^2}. \tag{G19}$$

α, β are the same for every channel, so we drop these constant terms and only compare the residual $\frac{N}{A\tilde{U}\alpha} - \frac{B}{A} + \ln A$. The first term $\frac{N}{A\tilde{U}\alpha}$ domains the saved free energy. A can be written as $(\mathcal{A}\hat{\lambda})^\dagger(\mathcal{A}\hat{\lambda})$ which is positive while $\tilde{f}(U_1,U_2)$ is negative. The

bigger $|A\tilde{f}(U_1, U_2)|$ is, the more free energy the system saves. The values of $A\tilde{f}(U_1, U_2)$ are degenerated in the space spanned by the order parameter in the freedom of the index ζ. We decompose the vector of order parameter $\lambda_\epsilon \hat{\Lambda}_\epsilon$ into the direct product of two parts $\lambda_\epsilon \hat{\Lambda}_{\epsilon,\kappa} \otimes \hat{\Lambda}_{\epsilon,\zeta}$, and obtain $\hat{\Lambda}_{\epsilon,\kappa}$ by maximizing $|A\tilde{f}(U_1, U_2)|$ and obtain $\hat{\Lambda}_{\epsilon,\zeta}$ by minimizing B. There are two A_{1u}, one A_{2u}, three E_u, four T_{1u}, and five T_{2u} channels in total. So, the $\hat{\Lambda}_{\epsilon,\kappa}$ for these channels have two, one, three, four, and five components, respectively. We use the conjugate gradient method to minimize $A\tilde{f}(U_1, U_2)$. With the obtained $\hat{\Lambda}_{\epsilon,\kappa}$, we sample on the unit vector $\hat{\Lambda}_{\epsilon,\zeta}$, which has the same number of components as the dimension of the channels themselves, and search for the ground states. We find that the E_u channel always takes [10] state, and T_{1u} states can take [001], [110], and [111] states, and the T_{2u} channel can take [001] and [111] states, in different regions of the phase diagram.

APPENDIX H: SYMMETRIES AND TOPOLOGICAL PROPERITIES OF EACH CHANNEL

In the Nambu space, $\hat{\psi}_{\boldsymbol{k}}^\dagger = (\hat{c}_{\boldsymbol{k},\uparrow}^\dagger, \hat{c}_{\boldsymbol{k},\downarrow}^\dagger, \hat{c}_{-\boldsymbol{k},\uparrow}, \hat{c}_{-\boldsymbol{k},\downarrow})$, the particle-hole symmetry takes the matrix form $\mathcal{C} = \eta_1\sigma_0 K$ (K is the conjugation operation), where η and σ are the Pauli matrices acting on the Nambu and the pseudospin degrees of freedom, respectively. The time-reversal symmetry takes the matrix form $\mathcal{T} = i\eta_0\sigma_2 K$. Combining the particle-hole symmetry and the time-reversal symmetry, we have the chiral symmetry $\mathcal{S} = \mathcal{C}\mathcal{T} = i\eta_1\sigma_2$. For the spatial symmetry operation R belonging to the D_{3d} group on the L_m Fermi pocket, we have

$$R\hat{c}_{\boldsymbol{k},d}^{m\dagger}R^\dagger = \sum_{d'} \hat{c}_{R\boldsymbol{k},d'}^{m\dagger}\mathcal{R}_{d'd}, \quad R\hat{c}_{\boldsymbol{k},d}^{m}R^\dagger = \sum_{d'} \hat{c}_{R\boldsymbol{k},d'}^{m}\mathcal{R}_{d'd}^*, \tag{H1}$$

where $\mathcal{R}$ is the transformation matrix corresponding to symmetry operation R. In the superconducting state, the spatial operation R transforms the pairing part of the BdG Hamiltonian $\sum_{m,d_1,d_2}(\mathcal{H}_{\rm SC}^m)_{d_1d_2}(\boldsymbol{k})\hat{c}_{\boldsymbol{k},d_1}^{m\dagger}\hat{c}_{-\boldsymbol{k},d_2}^{m\dagger} + \text{H.c.}$ as

$$\begin{aligned} &R\sum_{d_1,d_2}\left(\mathcal{H}_{\rm SC}^m\right)_{d_1d_2}(\boldsymbol{k})\hat{c}_{\boldsymbol{k},d_1}^\dagger\hat{c}_{-\boldsymbol{k},d_2}^\dagger R^\dagger \\ &= \sum_{d_1,d_2,d',d''}\left(\mathcal{H}_{\rm SC}^m\right)_{d_1d_2}(\boldsymbol{k})\hat{c}_{R\boldsymbol{k},d'^m}^\dagger\mathcal{R}_{d'd_1}\hat{c}_{-R\boldsymbol{k},d''}^{m\dagger}\mathcal{R}_{d''d_2} \\ &= \sum_{d',d''}\left(\mathcal{R}\mathcal{H}_{\rm SC}^m(\boldsymbol{k})\mathcal{R}^\intercal\right)_{d'd''}\hat{c}_{R\boldsymbol{k},d'}^{m\dagger}\hat{c}_{-R\boldsymbol{k},d''}^{m\dagger}. \end{aligned} \tag{H2}$$

In Eq. (G2), the spin-triplet pairing has the general form $\mathcal{H}_{\rm SC}^m(k) = i\boldsymbol{\sigma}\cdot\boldsymbol{d}(\boldsymbol{k})\sigma_2 = i\sigma_1\sigma_2 d_1(\boldsymbol{k}) + i\sigma_2\sigma_2 d_2(\boldsymbol{k}) + i\sigma_3\sigma_2 d_3(\boldsymbol{k})$. We take the mirror symmetry M_a as an example to show the constraint of the spatial symmetry on the superconductivity. M_a crosses the L_1 Fermi surface, and it maps $(k_X, k_Y, k_Z) \mapsto (k_Y, k_X, k_Z)$ in the global frame and $(k_x, k_y, k_z) \mapsto (-k_x, k_y, k_z)$ in the local frame defined at the L_1 point in Fig. 1(b). Obviously, the $k_x = 0$ plane is invariant under M_a. In the local reference frame at L_1, M_a takes the matrix form $\mathbb{M}_a$, $\mathbb{M}_a = e^{-\frac{i}{2}\sigma_1\pi} = -i\sigma_1$ under the basis $(\hat{c}_{\boldsymbol{k},\uparrow}^\dagger, \hat{c}_{\boldsymbol{k},\downarrow}^\dagger)$. Straightforwardly, we act $\mathbb{M}_a$ on the matrices $\boldsymbol{\sigma}\sigma_2$ and have

$$\begin{aligned} \mathbb{M}_a\sigma_1\sigma_2\mathbb{M}_a^\intercal &= \sigma_1\sigma_2, \\ \mathbb{M}_a\sigma_2\sigma_2\mathbb{M}_a^\intercal &= -\sigma_2\sigma_2, \\ \mathbb{M}_a\sigma_3\sigma_2\mathbb{M}_a^\intercal &= -\sigma_3\sigma_2. \end{aligned} \tag{H3}$$

According to the above equation, one obtains that under M_a the spin-triplet pairing transforms as $\mathbb{M}_a\mathcal{H}_{\rm SC}(\boldsymbol{k})\mathbb{M}_a^\intercal = \tilde{\mathcal{H}}_{\rm SC}(\boldsymbol{k}) = i\sigma_1\sigma_2 d_1(\boldsymbol{k}) - i\sigma_2\sigma_2 d_2(\boldsymbol{k}) - i\sigma_3\sigma_2 d_3(\boldsymbol{k})$. In the mirror-invariant plane, $\mathbb{M}_a\mathcal{H}_{\rm SC}(\boldsymbol{k})\mathbb{M}_a^\intercal = \ell\mathcal{H}(M_a\boldsymbol{k})$, with $\ell = \pm 1$ determined by the form of $\boldsymbol{d}(\boldsymbol{k})$ and $\ell = 1$ ($\ell = -1$) corresponding to the mirror-even (mirror-odd) superconductivity. In the Nambu space, the matrix form of the mirror symmetry M_a is

$$\mathcal{M}_a = \begin{pmatrix} \mathbb{M}_a & 0 \\ 0 & \ell\mathbb{M}_a^* \end{pmatrix}. \tag{H4}$$

In the following, we give more detailed analysis on the topological properties of the superconducting ground states in the phase diagram in the main text.

A_{1u}: The A_{1u} state is full gap. We consider the superconductivity on the L_1 Fermi pocket, where the **d** vector, as mentioned in the main text, is $\boldsymbol{d}(\boldsymbol{k}) = (\alpha k_x, \alpha k_y, \beta k_z)$ (both the **d** vector and the coefficients α, β are obtained from the mean-field calculation). For a 3D full-gap SC belonging to class DIII, its topological invariant is the 3D winding number. For the simple single-orbital model in our consideration, to obtain the 3D winding number, we can write the pairing function in the form $\mathcal{H}_{\rm SC}(\boldsymbol{k}) = \sum_{m,n=1,2,3} ik_m\mathcal{A}_{mn}\sigma_n\sigma_2$, where we use $k_{1,2,3}$ to denote $k_{x,y,z}$. In the above form, it can be proved that the winding number of the single-orbital Hamiltonian equals to $\text{sgn}(\det\mathcal{A})$ (notice that the conclusion

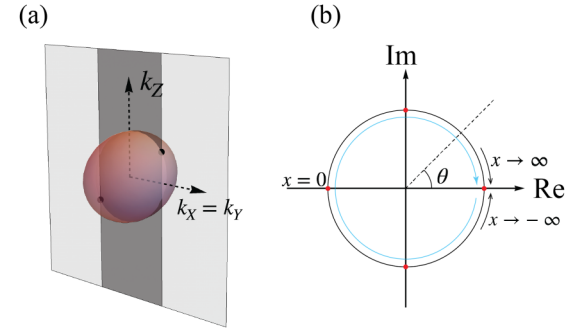

FIG. 11. (a) Shows the Fermi surface L_1 (the red ball) and the two black points stand for the superconducting nodes on the Fermi surface in the A_{2u} state. We use the transparent gray plane to denote the mirror plane. In the BZ on the (001) surface, at the projecting points of the dark gray region, there exist Majorana zero-energy arcs. (b) Re and Im stand for the real and imaginary axis. θ is the complex phase angle of the off-diagonal entry in Eq. (H8). If we take x from $-\infty$ to ∞, θ will travel on the circle along the direction of the blue trace. It approaches to the red point on the positive real axis from up (down) side, when we take $x \to \infty$ ($x \to -\infty$). If we take $x = 0$, the off-diagonal entry is a negative real number, indicated by the red point on the negative real axis. The two red points on the imaginary axis correspond to the two roots of the equation $\frac{1}{3m}x^2 + \frac{\xi}{6m}(3k_X - x)^2 - \mu = 0$ with opposite sign.

only applies to the single-orbital model in our consideration, i.e., H_0 in the main text, with merely linear terms of $\mathbf{k}$ in the superconducting pairing). Since the superconducting order is even under the C_4 symmetry in the A_{1u} channel, the winding number of each pocket is the same, i.e., $\mathrm{sgn}(\det \mathcal{A})$ being the same on each of the pockets, and the system is characterized by the total winding number $w = 4\,\mathrm{sgn}(\alpha^2\beta)$.

A_{2u}: The A_{2u} state is gapless, and we show the gapless point on the L_1 Fermi surface in Fig. 11(a). The d vector on the L_1 pocket is $\boldsymbol{d}(\boldsymbol{k}) = (-\alpha k_y, \alpha k_x, 0)$. The nodal gap structure in the A_{2u} state is protected by the mirror symmetry M_a and the chiral symmetry. Under the mirror symmetry M_a, the pairing function transforms as

$$\mathbb{M}_a \mathcal{H}_{\mathrm{SC}}(\boldsymbol{k}) \mathbb{M}_a^{\mathsf{T}} = \tilde{\mathcal{H}}(\boldsymbol{k}) = -i\sigma_1\sigma_2\alpha k_y - i\sigma_2\sigma_2\alpha k_x = \mathcal{H}_{\mathrm{SC}}(M_a\boldsymbol{k}). \quad \text{(H5)}$$

Obviously, the superconducting order is even under M_a, namely $\ell = 1$, and the chiral symmetry commutes with M_a. To show the topological protection of the nodal gap structure, we first decompose the BdG Hamiltonian according to M_a in the mirror-invariant plane ($k_x = 0$) into different mirror-invariant subspaces with the basis $\hat{\psi}^\dagger_{\boldsymbol{k}} = 1/\sqrt{2}(-\hat{c}^\dagger_{\boldsymbol{k},\uparrow} + \hat{c}^\dagger_{\boldsymbol{k},\downarrow}, \hat{c}_{-\boldsymbol{k},\uparrow} + \hat{c}_{-\boldsymbol{k},\downarrow}, \hat{c}^\dagger_{\boldsymbol{k},\uparrow} + \hat{c}^\dagger_{\boldsymbol{k},\downarrow}, -\hat{c}_{-\boldsymbol{k},\uparrow} + \hat{c}_{-\boldsymbol{k},\downarrow})$, and the Hamiltonian takes the form

$$H_{\mathrm{BdG}}(\boldsymbol{k}, k_x = 0) = \begin{pmatrix} \frac{k_y^2}{2m} + \frac{\xi k_z^2}{2m} - \mu & -\alpha k_y & 0 & 0 \\ -\alpha k_y & -\frac{k_y^2}{2m} - \frac{\xi k_z^2}{2m} + \mu & 0 & 0 \\ 0 & 0 & \frac{k_y^2}{2m} + \frac{\xi k_z^2}{2m} - \mu & -\alpha k_y \\ 0 & 0 & -\alpha k_y & -\frac{k_y^2}{2m} - \frac{\xi k_z^2}{2m} + \mu \end{pmatrix}. \quad \text{(H6)}$$

Within each subspace, the chiral symmetry is respected. Then, we transform the Hamiltonian in each subspace to the off-diagonalized form

$$H_{\mathrm{submirror}} = \begin{pmatrix} 0 & i\alpha k_y + \frac{k_y^2}{2m} + \frac{\xi k_z^2}{2m} - \mu \\ -i\alpha k_y + \frac{k_y^2}{2m} + \frac{\xi k_z^2}{2m} - \mu & 0 \end{pmatrix}. \quad \text{(H7)}$$

To study the surface modes on the (001) surface, we change the Hamiltonian from the local to the global reference frame with $k_y = \sqrt{\frac{1}{6}}(k_X + k_Y) - \sqrt{\frac{2}{3}}k_Z$, $k_z = \sqrt{\frac{1}{3}}(k_X + k_Y + k_Z)$, and in the mirror-invariant plane $k_X = k_Y$ we have

$$H_{\mathrm{submirror}} = \begin{pmatrix} 0 & i\alpha\sqrt{\frac{2}{3}}(k_X - k_Z) + \frac{(k_X - k_Z)^2}{3m} + \xi\frac{(2k_X + k_Z)^2}{6m} - \mu \\ -i\alpha\sqrt{\frac{2}{3}}(k_X - k_Z) + \frac{(k_X - k_Z)^2}{3m} + \xi\frac{(2k_X + k_Z)^2}{6m} - \mu & 0 \end{pmatrix}. \quad \text{(H8)}$$

We take k_X satisfying $-\sqrt{\frac{2m\mu}{3\xi}} < k_X < \sqrt{\frac{2m\mu}{3\xi}}$, i.e., the dark gray region in Fig. 11(a), and set $k_X - k_Z = x$. The off-diagonal terms in Eq. (H8) become $\pm i\alpha x + \frac{1}{3m}x^2 + \frac{\xi}{6m}(3k_X - x)^2 - \mu$. When we take x from $-\infty$ to ∞, equivalent to k_Z from ∞ to $-\infty$, the complex phase of the off-diagonal terms changes from 0 to -2π as indicated in Fig. 11(b). Namely, for each fixed k_X satisfying $-\sqrt{\frac{2m\mu}{3\xi}} < k_X < \sqrt{\frac{2m\mu}{3\xi}}$, the line (k_X, k_X, k_Z) carries a 1D winding number -1, leading to a pair of zero-energy modes at the point (k_X, k_X) in the surface BZ on the (001) surface. Take all the k_X into account, and we can get the Majorana zero-energy arcs shown in the main text.

E_u: For the E_u state which is fully gapped, the unit vector (t_1, t_2) in the order parameter is taken as $(1, 0)$. From the representation table in the main text, we know that the symmetry of the system breaks from the group O_h to D_{4h}. However, the C_{2a} and C_4 symmetries are preserved and the character of C_{2a} and C_4 symmetries equal to 1, i.e., the superconducting order being even under C_{2a} and C_4. Therefore, though there is symmetry breaking, the E_u state has similar topological property with the A_{1u} state. Specifically, the $\mathbf{d}$ vector on the L_1 Fermi pocket is $(\alpha k_x, \alpha k_y + \beta k_z, \gamma k_y)$, and the system is characterized by the winding number $w = -4\,\mathrm{sgn}(\alpha\beta\gamma)$.

$T_{2u,[001]}$: For the $T_{2u,[001]}$ state, the symmetry of the system breaks from the O_h group to the D_{4h} group, and the C_{2a} and C_4 symmetries are respected according to the irreps table in the main text. The character of C_{2q} and C_4 equals to 1 and -1, respectively. On the L_1 Fermi pocket, the $\mathbf{d}$ vector takes the form $\boldsymbol{d}(\boldsymbol{k}) = (\alpha k_x, \beta_1 k_y + \beta_2 k_z, \gamma_1 k_y + \gamma_2 k_z)$. The 3D winding number contributed by the L_1 Fermi pocket is $w_1 = \mathrm{sgn}(\det \mathcal{A}) = \mathrm{sgn}(\alpha\beta_1\gamma_2 - \alpha\beta_2\gamma_1)$. However, different from A_{1u} and E_u, the superconducting order is odd under C_4 symmetry leading to opposite 3D winding numbers on the C_4-related Fermi pockets. Namely, the winding numbers contributed by the four Fermi pockets are $w_1, -w_1, w_1, -w_1$, respectively. We can see that the total winding number gives 0. However, the state is topologically nontrivial and is characterized by nonzero mirror Chern numbers. We consider the mirror symmetry M_a under

which the superconducting order is odd and $\mathbb{M}_a\mathcal{H}_{\rm sc}(\boldsymbol{k})\mathbb{M}_a^{\intercal} = -\mathcal{H}_{\rm sc}(\boldsymbol{k})$ in the $k_x = 0$ plane. In the mirror-invariant plane, we can decompose the BdG Hamiltonian into different mirror subspaces. Similar to the A_{2u} case, we change the basis to the mirror-invariant eigenstates $\hat{\psi}_{\boldsymbol{k}}^{\dagger} = 1/\sqrt{2}(-\hat{c}_{-\boldsymbol{k},\uparrow} + \hat{c}_{-\boldsymbol{k},\downarrow}, -\hat{c}_{\boldsymbol{k},\uparrow}^{\dagger} + \hat{c}_{\boldsymbol{k},\downarrow}^{\dagger}, \hat{c}_{-\boldsymbol{k},\uparrow} + \hat{c}_{-\boldsymbol{k},\downarrow}, \hat{c}_{\boldsymbol{k},\uparrow}^{\dagger} + \hat{c}_{\boldsymbol{k},\downarrow}^{\dagger})$, and obtain the Hamiltonian

$$H_{\rm BdG}(\boldsymbol{k}, k_x = 0) = \begin{pmatrix} -\frac{k_y^2}{2m} - \frac{\xi k_z^2}{2m} + \mu & -i\beta_1 k_y - i\beta_2 k_z - \gamma_1 k_y - \gamma_2 k_z & 0 & 0 \\ i\beta_1 k_y + i\beta_2 k_z - \gamma_1 k_y - \gamma_2 k_z & \frac{k_y^2}{2m} + \frac{\xi k_z^2}{2m} - \mu & 0 & 0 \\ 0 & 0 & -\frac{k_y^2}{2m} - \frac{\xi k_z^2}{2m} + \mu & \gamma_1 k_y + \gamma_2 k_z - i\beta_1 k_y - i\beta_2 k_z \\ 0 & 0 & \gamma_1 k_y + \gamma_2 k_z + i\beta_1 k_y + i\beta_2 k_z & \frac{k_y^2}{2m} + \frac{\xi k_z^2}{2m} - \mu \end{pmatrix}. \tag{H9}$$

In each mirror subspace in the $k_x = 0$ plane, there exists a gapless point at $k_y = k_z = 0$ when the chemical potential $\mu = 0$. The nonzero chemical potential gaps out the system and $\mu < 0$ (> 0) makes the system topologically trivial (nontrivial). Therefore, the condition $\mu = 0$ is a topological phase transition point within the $k_x = 0$ plane. We can calculate the topological charge of the gapless point, according to which we can obtain the mirror Chern number. It turns out that the mirror Chern number contributed by the L_1 Fermi pocket is $\mathrm{sgn}(\det \mathcal{A}') = \mathrm{sgn}(\beta_1\gamma_2 - \beta_2\gamma_1)$. Since the L_1 and L_3 Fermi pockets (related by C_4^2) both cross M_a, both of the two Fermi pockets contribute to the mirror Chern number. Moreover, based on a similar analysis one can find that the mirror Chern number from the L_3 Fermi pocket is the same as that on the L_1 Fermi pocket. As a result, the $T_{2u,[001]}$ state carries the mirror Chern number $2\,\mathrm{sgn}(\beta_1\gamma_2 - \beta_2\gamma_1)$ in the M_a-invariant plane, which suggests the second-order topological superconductivity.

For the other states in the phase diagram, we do not show the analysis in detail since all these states can be analyzed in similar ways.

APPENDIX I: CALCULATION OF EDGE STATES

We consider the open boundary condition along the Z direction and treat k_Z as $-i\frac{\partial}{\partial Z}$. We write

$$-i\frac{\partial}{\partial Z}|Z, k_x, k_y, w\rangle = -i\frac{|Z + dZ, k_x, k_y, w\rangle - |Z - dZ, k_x, k_y, w\rangle}{2dZ}, \tag{I1}$$

where w is the pseudospin index. We first write the BdG Hamiltonian in the basis of $(|Z_1, k_x, k_y, w\rangle, |Z_2, k_x, k_y, w\rangle, \ldots, |Z_N, k_x, k_y, w\rangle)^{\intercal}$. We assume there are totally N sites in the Z direction and $Z_{i+1} - Z_i = dZ \to 0$. In the periodic boundary condition, we stick the Nth site with the first site. The operator $\hat{k}_Z$ can be written as

$$\hat{k}_Z = \frac{1}{2\,dZ}\begin{pmatrix} 0 & i & 0 & \cdots & 0 & -i \\ -i & 0 & i & \cdots & 0 & 0 \\ 0 & -i & 0 & \cdots & 0 & 0 \\ \vdots & \vdots & \vdots & \ddots & \vdots & \vdots \\ 0 & 0 & 0 & \cdots & 0 & i \\ i & 0 & 0 & \cdots & -i & 0 \end{pmatrix}. \tag{I2}$$

While, for the open boundary condition, we cut off the loop and remove the coupling between the Nth site and the first site in the matrix. Namely, in the open boundary condition, we have the operator $\hat{k}_Z$ as

$$\hat{k}_Z = \frac{1}{2\,dZ}\begin{pmatrix} 0 & i & 0 & \cdots & 0 & 0 \\ -i & 0 & i & \cdots & 0 & 0 \\ 0 & -i & 0 & \cdots & 0 & 0 \\ \vdots & \vdots & \vdots & \ddots & \vdots & \vdots \\ 0 & 0 & 0 & \cdots & 0 & i \\ 0 & 0 & 0 & \cdots & -i & 0 \end{pmatrix}. \tag{I3}$$

For the second-order derivation of Z, i.e., $\hat{k}_Z^2$, we have

$$\hat{k}_Z^2 = -\frac{\partial^2}{\partial Z^2}|Z, k_x, k_y, w\rangle = -\frac{|Z + dZ, k_x, k_y, w\rangle + |Z - dZ, k_x, k_y, w\rangle - 2|Z, k_x, k_y, w\rangle}{dZ^2}. \tag{I4}$$

In the periodic condition we have

$$\hat{k}_Z^2 = -\frac{1}{dZ^2}\begin{pmatrix} -2 & 1 & 0 & \cdots & 0 & 1 \\ 1 & -2 & 1 & \cdots & 0 & 0 \\ 0 & 1 & -2 & \cdots & 0 & 0 \\ \vdots & \vdots & \vdots & \ddots & \vdots & \vdots \\ 0 & 0 & 0 & \cdots & -2 & 1 \\ 1 & 0 & 0 & \cdots & 1 & -2 \end{pmatrix}. \tag{I5}$$

In the open boundary condition we have

$$\hat{k}_Z^2 = -\frac{1}{dZ^2}\begin{pmatrix} -2 & 1 & 0 & \cdots & 0 & 0 \\ 1 & -2 & 1 & \cdots & 0 & 0 \\ 0 & 1 & -2 & \cdots & 0 & 0 \\ \vdots & \vdots & \vdots & \ddots & \vdots & \vdots \\ 0 & 0 & 0 & \cdots & -2 & 1 \\ 0 & 0 & 0 & \cdots & 1 & -2 \end{pmatrix}. \tag{I6}$$

We substitute $\hat{k}_Z$ and $\hat{k}_Z^2$ in the open boundary condition in Eqs. (I3) and (I6) into the BdG Hamiltonian and diagonalize the Hamiltonian to obtain the surface modes.

[1] M. Z. Hasan and C. L. Kane, Rev. Mod. Phys. **82**, 3045 (2010).
[2] X.-L. Qi and S.-C. Zhang, Rev. Mod. Phys. **83**, 1057 (2011).
[3] A. Bansil, H. Lin, and T. Das, Rev. Mod. Phys. **88**, 021004 (2016).
[4] C.-K. Chiu, J. C. Y. Teo, A. P. Schnyder, and S. Ryu, Rev. Mod. Phys. **88**, 035005 (2016).
[5] N. P. Armitage, E. J. Mele, and A. Vishwanath, Rev. Mod. Phys. **90**, 015001 (2018).
[6] Y. Ando and L. Fu, Annu. Rev. Condens. Matter Phys. **6**, 361 (2015).
[7] B. J. Wieder, B. Bradlyn, J. Cano, Z. Wang, M. G. Vergniory, L. Elcoro, A. A. Soluyanov, C. Felser, T. Neupert, N. Regnault *et al.*, Nat. Rev. Mater. **7**, 196 (2022).
[8] Y. Ando, J. Phys. Soc. Jpn. **82**, 102001 (2013).
[9] M. König, S. Wiedmann, C. Brüne, A. Roth, H. Buhmann, L. W. Molenkamp, X.-L. Qi, and S.-C. Zhang, Science **318**, 766 (2007).
[10] D. Hsieh, D. Qian, L. Wray, Y. Xia, Y. S. Hor, R. J. Cava, and M. Z. Hasan, Nature (London) **452**, 970 (2008).
[11] Y. Tanaka, Z. Ren, T. Sato, K. Nakayama, S. Souma, T. Takahashi, K. Segawa, and Y. Ando, Nat. Phys. **8**, 800 (2012).
[12] Z. K. Liu, B. Zhou, Y. Zhang, Z. J. Wang, H. M. Weng, D. Prabhakaran, S.-K. Mo, Z. X. Shen, Z. Fang, X. Dai, Z. Hussain, and Y. L. Chen, Science **343**, 864 (2014).
[13] Z. Liu, J. Jiang, B. Zhou, Z. Wang, Y. Zhang, H. Weng, D. Prabhakaran, S. K. Mo, H. Peng, P. Dudin *et al.*, Nat. Mater. **13**, 677 (2014).
[14] B. Q. Lv, H. M. Weng, B. B. Fu, X. P. Wang, H. Miao, J. Ma, P. Richard, X. C. Huang, L. X. Zhao, G. F. Chen, Z. Fang, X. Dai, T. Qian, and H. Ding, Phys. Rev. X **5**, 031013 (2015).
[15] S.-Y. Xu, I. Belopolski, N. Alidoust, M. Neupane, G. Bian, C. Zhang, R. Sankar, G. Chang, Z. Yuan, C.-C. Lee, S.-M. Huang, H. Zheng, J. Ma, D. S. Sanchez, B. Wang, A. Bansil, F. Chou, P. P. Shibayev, H. Lin, S. Jia, and M. Z. Hasan, Science **349**, 613 (2015).
[16] L. Lu, Z. Wang, D. Ye, L. Ran, L. Fu, J. D. Joannopoulos, and M. Soljačić, Science **349**, 622 (2015).
[17] J. Ma, C. Yi, B. Lv, Z. Wang, S. Nie, L. Wang, L. Kong, Y. Huang, P. Richard, P. Zhang, K. Yaji, K. Kuroda, S. Shin, H. Weng, B. A. Bernevig, Y. Shi, T. Qian, and H. Ding, Sci. Adv. **3** (2017).
[18] G. Bian, T.-R. Chang, R. Sankar, S.-Y. Xu, H. Zheng, T. Neupert, C.-K. Chiu, S.-M. Huang, G. Chang, I. Belopolski *et al.*, Nat. Commun. **7**, 10556 (2016).
[19] F. Schindler, Z. Wang, M. G. Vergniory, A. M. Cook, A. Murani, S. Sengupta, A. Y. Kasumov, R. Deblock, S. Jeon, I. Drozdov *et al.*, Nat. Phys. **14**, 918 (2018).
[20] Z. Rao, H. Li, T. Zhang, S. Tian, C. Li, B. Fu, C. Tang, L. Wang, Z. Li, W. Fan *et al.*, Nature (London) **567**, 496 (2019).
[21] P. Zhang, Z. Wang, X. Wu, K. Yaji, Y. Ishida, Y. Kohama, G. Dai, Y. Sun, C. Bareille, K. Kuroda *et al.*, Nat. Phys. **15**, 41 (2019).
[22] J. Alicea, Rep. Prog. Phys. **75**, 076501 (2012).
[23] M. Sato and S. Fujimoto, J. Phys. Soc. Jpn. **85**, 072001 (2016).
[24] M. Sato and Y. Ando, Rep. Prog. Phys. **80**, 076501 (2017).
[25] S. Sasaki, M. Kriener, K. Segawa, K. Yada, Y. Tanaka, M. Sato, and Y. Ando, Phys. Rev. Lett. **107**, 217001 (2011).
[26] V. Mourik, K. Zuo, S. M. Frolov, S. R. Plissard, E. P. A. M. Bakkers, and L. P. Kouwenhoven, Science **336**, 1003 (2012).
[27] A. Das, Y. Ronen, Y. Most, Y. Oreg, M. Heiblum, and H. Shtrikman, Nat. Phys. **8**, 887 (2012).
[28] S. Nadj-Perge, I. K. Drozdov, J. Li, H. Chen, S. Jeon, J. Seo, A. H. MacDonald, B. A. Bernevig, and A. Yazdani, Science **346** (2014).
[29] J.-P. Xu, M.-X. Wang, Z. L. Liu, J.-F. Ge, X. Yang, C. Liu, Z. A. Xu, D. Guan, C. L. Gao, D. Qian, Y. Liu, Q.-H. Wang,

F.-C. Zhang, Q.-K. Xue, and J.-F. Jia, Phys. Rev. Lett. **114**, 017001 (2015).
[30] J.-X. Yin, Z. Wu, J. Wang, Z. Ye, J. Gong, X. Hou, L. Shan, A. Li, X. Liang, X. Wu *et al.*, Nat. Phys. **11**, 543 (2015).
[31] D. Wang, L. Kong, P. Fan, H. Chen, S. Zhu, W. Liu, L. Cao, Y. Sun, S. Du, J. Schneeloch *et al.*, Science **362**, 333 (2018).
[32] H. Ren, F. Pientka, S. Hart, A. T. Pierce, M. Kosowsky, L. Lunczer, R. Schlereth, B. Scharf, E. M. Hankiewicz, L. W. Molenkamp *et al.*, Nature (London) **569**, 93 (2019).
[33] A. Fornieri, A. M. Whiticar, F. Setiawan, E. Portolés, A. C. Drachmann, A. Keselman, S. Gronin, C. Thomas, T. Wang, R. Kallaher *et al.*, Nature (London) **569**, 89 (2019).
[34] A. Palacio-Morales, E. Mascot, S. Cocklin, H. Kim, S. Rachel, D. K. Morr, and R. Wiesendanger, Sci. Adv. **5**, eaav6600 (2019).
[35] S. Kezilebieke, M. N. Huda, V. Vaňo, M. Aapro, S. C. Ganguli, O. J. Silveira, S. Głodzik, A. S. Foster, T. Ojanen, and P. Liljeroth, Nature (London) **588**, 424 (2020).
[36] C. Chen, K. Jiang, Y. Zhang, C. Liu, Y. Liu, Z. Wang, and J. Wang, Nat. Phys. **16**, 536 (2020).
[37] S. Vaitiekenas, G. W. Winkler, B. van Heck, T. Karzig, M.-T. Deng, K. Flensberg, L. I. Glazman, C. Nayak, P. Krogstrup, R. M. Lutchyn, and C. M. Marcus, Science **367** (2020).
[38] T. Li, J. Ingham, and H. D. Scammell, Phys. Rev. Res. **2**, 043155 (2020).
[39] C. Nayak, S. H. Simon, A. Stern, M. Freedman, and S. Das Sarma, Rev. Mod. Phys. **80**, 1083 (2008).
[40] S. Vijay, T. H. Hsieh, and L. Fu, Phys. Rev. X **5**, 041038 (2015).
[41] B. Lian, X.-Q. Sun, A. Vaezi, X.-L. Qi, and S.-C. Zhang, Proc. Natl. Acad. Sci. USA **115**, 10938 (2018).
[42] L. Fu and C. L. Kane, Phys. Rev. Lett. **100**, 096407 (2008).
[43] H.-H. Sun, K.-W. Zhang, L.-H. Hu, C. Li, G.-Y. Wang, H.-Y. Ma, Z.-A. Xu, C.-L. Gao, D.-D. Guan, Y.-Y. Li, C. Liu, D. Qian, Y. Zhou, L. Fu, S.-C. Li, F.-C. Zhang, and J.-F. Jia, Phys. Rev. Lett. **116**, 257003 (2016).
[44] Y.-F. Lv, W.-L. Wang, Y.-M. Zhang, H. Ding, W. Li, L. Wang, K. He, C.-L. Song, X.-C. Ma, and Q.-K. Xue, Sci. Bull. **62**, 852 (2017).
[45] Y. Yuan, J. Pan, X. Wang, Y. Fang, C. Song, L. Wang, K. He, X. Ma, H. Zhang, F. Huang *et al.*, Nat. Phys. **15**, 1046 (2019).
[46] Y. Li, H. Zheng, Y. Fang, D. Zhang, Y. Chen, C. Chen, A. Liang, W. Shi, D. Pei, L. Xu *et al.*, Nat. Commun. **12**, 1 (2021).
[47] P. Zhang, K. Yaji, T. Hashimoto, Y. Ota, T. Kondo, K. Okazaki, Z. Wang, J. Wen, G. D. Gu, H. Ding, and S. Shin, Science **360**, 182 (2018).
[48] Q. Liu, C. Chen, T. Zhang, R. Peng, Y.-J. Yan, C.-H.-P. Wen, X. Lou, Y.-L. Huang, J.-P. Tian, X.-L. Dong, G.-W. Wang, W.-C. Bao, Q.-H. Wang, Z.-P. Yin, Z.-X. Zhao, and D.-L. Feng, Phys. Rev. X **8**, 041056 (2018).
[49] L. Kong, S. Zhu, M. Papaj, H. Chen, L. Cao, H. Isobe, Y. Xing, W. Liu, D. Wang, P. Fan *et al.*, Nat. Phys. **15**, 1181 (2019).
[50] S. Zhu, L. Kong, L. Cao, H. Chen, M. Papaj, S. Du, Y. Xing, W. Liu, D. Wang, C. Shen, F. Yang, J. Schneeloch, R. Zhong, G. Gu, L. Fu, Y.-Y. Zhang, H. Ding, and H.-J. Gao, Science **367**, 189 (2020).
[51] T. Machida, Y. Sun, S. Pyon, S. Takeda, Y. Kohsaka, T. Hanaguri, T. Sasagawa, and T. Tamegai, Nat. Mater. **18**, 811 (2019).
[52] W. Liu, L. Cao, S. Zhu, L. Kong, G. Wang, M. Papaj, P. Zhang, Y.-B. Liu, H. Chen, G. Li *et al.*, Nat. Commun. **11**, 1 (2020).
[53] L. Kong, L. Cao, S. Zhu, M. Papaj, G. Dai, G. Li, P. Fan, W. Liu, F. Yang, X. Wang *et al.*, Nat. Commun. **12**, 4146 (2021).
[54] G. Xu, B. Lian, P. Tang, X.-L. Qi, and S.-C. Zhang, Phys. Rev. Lett. **117**, 047001 (2016).
[55] Z. Wang, P. Zhang, G. Xu, L. K. Zeng, H. Miao, X. Xu, T. Qian, H. Weng, P. Richard, A. V. Fedorov, H. Ding, X. Dai, and Z. Fang, Phys. Rev. B **92**, 115119 (2015).
[56] A. Y. Kitaev, Phys. Usp. **44**, 131 (2001).
[57] A. P. Mackenzie and Y. Maeno, Rev. Mod. Phys. **75**, 657 (2003).
[58] Y. Maeno, S. Kittaka, T. Nomura, S. Yonezawa, and K. Ishida, J. Phys. Soc. Jpn. **81**, 011009 (2011).
[59] C. Kallin and J. Berlinsky, Rep. Prog. Phys. **79**, 054502 (2016).
[60] L. Jiao, S. Howard, S. Ran, Z. Wang, J. O. Rodriguez, M. Sigrist, Z. Wang, N. P. Butch, and V. Madhavan, Nature (London) **579**, 523 (2020).
[61] X.-L. Qi, T. L. Hughes, and S.-C. Zhang, Phys. Rev. B **82**, 184516 (2010).
[62] J. D. Sau, R. M. Lutchyn, S. Tewari, and S. Das Sarma, Phys. Rev. Lett. **104**, 040502 (2010).
[63] R. M. Lutchyn, J. D. Sau, and S. Das Sarma, Phys. Rev. Lett. **105**, 077001 (2010).
[64] Y. Oreg, G. Refael, and F. von Oppen, Phys. Rev. Lett. **105**, 177002 (2010).
[65] J. Alicea, Phys. Rev. B **81**, 125318 (2010).
[66] S. Sasaki and T. Mizushima, Phys. C (Amsterdam) **514**, 206 (2015).
[67] H. Zhang, C.-X. Liu, X.-L. Qi, X. Dai, Z. Fang, and S.-C. Zhang, Nat. Phys. **5**, 438 (2009).
[68] Y. Xia, D. Qian, D. Hsieh, L. Wray, A. Pal, H. Lin, A. Bansil, D. Grauer, Y. S. Hor, R. J. Cava *et al.*, Nat. Phys. **5**, 398 (2009).
[69] Y. L. Chen, J. G. Analytis, J.-H. Chu, Z. K. Liu, S.-K. Mo, X. L. Qi, H. J. Zhang, D. H. Lu, X. Dai, Z. Fang, S. C. Zhang, I. R. Fisher, Z. Hussain, and Z.-X. Shen, Science **325**, 178 (2009).
[70] D. Hsieh, Y. Xia, L. Wray, D. Qian, A. Pal, J. H. Dil, J. Osterwalder, F. Meier, G. Bihlmayer, C. L. Kane, Y. S. Hor, R. J. Cava, and M. Z. Hasan, Science **323**, 919 (2009).
[71] Y. S. Hor, A. J. Williams, J. G. Checkelsky, P. Roushan, J. Seo, Q. Xu, H. W. Zandbergen, A. Yazdani, N. P. Ong, and R. J. Cava, Phys. Rev. Lett. **104**, 057001 (2010).
[72] Z. Liu, X. Yao, J. Shao, M. Zuo, L. Pi, S. Tan, C. Zhang, and Y. Zhang, J. Am. Chem. Soc. **137**, 10512 (2015).
[73] Shruti, V. K. Maurya, P. Neha, P. Srivastava, and S. Patnaik, Phys. Rev. B **92**, 020506(R) (2015).
[74] Y. Qiu, K. N. Sanders, J. Dai, J. E. Medvedeva, W. Wu, P. Ghaemi, T. Vojta, and Y. S. Hor, arXiv:1512.03519.
[75] Z. Wang, A. A. Taskin, T. Frölich, M. Braden, and Y. Ando, Chem. Mater. **28**, 779 (2016).
[76] S. Yonezawa, K. Tajiri, S. Nakata, Y. Nagai, Z. Wang, K. Segawa, Y. Ando, and Y. Maeno, Nat. Phys. **13**, 123 (2017).
[77] K. Matano, M. Kriener, K. Segawa, Y. Ando, and G.-q. Zheng, Nat. Phys. **12**, 852 (2016).

[78] R. Tao, Y.-J. Yan, X. Liu, Z.-W. Wang, Y. Ando, Q.-H. Wang, T. Zhang, and D.-L. Feng, Phys. Rev. X **8**, 041024 (2018).
[79] T. Asaba, B. J. Lawson, C. Tinsman, L. Chen, P. Corbae, G. Li, Y. Qiu, Y. S. Hor, L. Fu, and L. Li, Phys. Rev. X **7**, 011009 (2017).
[80] G. Du, Y. Li, J. Schneeloch, R. Zhong, G. Gu, H. Yang, H. Lin, and H.-H. Wen, Sci. China Phys. Mech. Astron. **60**, 037411 (2017).
[81] Y. Pan, A. Nikitin, G. Araizi, Y. Huang, Y. Matsushita, T. Naka, and A. De Visser, Sci. Rep. **6**, 1 (2016).
[82] L. Fu and E. Berg, Phys. Rev. Lett. **105**, 097001 (2010).
[83] J. W. F. Venderbos, V. Kozii, and L. Fu, Phys. Rev. B **94**, 180504(R) (2016).
[84] T. H. Hsieh, H. Lin, J. Liu, W. Duan, A. Bansil, and L. Fu, Nat. Commun. **3**, 982 (2012).
[85] A. S. Erickson, J.-H. Chu, M. F. Toney, T. H. Geballe, and I. R. Fisher, Phys. Rev. B **79**, 024520 (2009).
[86] Y. Matsushita, H. Bluhm, T. H. Geballe, and I. R. Fisher, Phys. Rev. Lett. **94**, 157002 (2005).
[87] S. Sasaki, Z. Ren, A. A. Taskin, K. Segawa, L. Fu, and Y. Ando, Phys. Rev. Lett. **109**, 217004 (2012).
[88] H. Yang, Y.-Y. Li, T.-T. Liu, D.-D. Guan, S.-Y. Wang, H. Zheng, C. Liu, L. Fu, and J.-F. Jia, Phys. Rev. Lett. **125**, 136802 (2020).
[89] J. Hu and H. Ding, Sci. Rep. **2**, 381 (2012).
[90] A. P. Schnyder, S. Ryu, A. Furusaki, and A. W. W. Ludwig, Phys. Rev. B **78**, 195125 (2008).
[91] S. Ryu, A. P. Schnyder, A. Furusaki, and A. W. W. Ludwig, New J. Phys. **12**, 065010 (2010).
[92] X.-L. Qi, T. L. Hughes, and S.-C. Zhang, Phys. Rev. B **81**, 134508 (2010).
[93] G. E. Volovik, *The Universe in a Helium Droplet* (Oxford University Press, Oxford, 2003), Vol. 117.
[94] S. A. Yang, H. Pan, and F. Zhang, Phys. Rev. Lett. **113**, 046401 (2014).
[95] Y. Ueno, A. Yamakage, Y. Tanaka, and M. Sato, Phys. Rev. Lett. **111**, 087002 (2013).
[96] W. A. Benalcazar, B. A. Bernevig, and T. L. Hughes, Science **357**, 61 (2017).
[97] W. A. Benalcazar, B. A. Bernevig, and T. L. Hughes, Phys. Rev. B **96**, 245115 (2017).
[98] Z. Song, Z. Fang, and C. Fang, Phys. Rev. Lett. **119**, 246402 (2017).
[99] E. Khalaf, Phys. Rev. B **97**, 205136 (2018).
[100] S. Ono, H. C. Po, and H. Watanabe, Sci. Adv. **6** (2020).
[101] F. Schindler, A. M. Cook, M. G. Vergniory, Z. Wang, S. S. P. Parkin, B. A. Bernevig, and T. Neupert, Sci. Adv. **4**, eaat0346 (2018).
[102] J. Langbehn, Y. Peng, L. Trifunovic, F. von Oppen, and P. W. Brouwer, Phys. Rev. Lett. **119**, 246401 (2017).
[103] F. Zhang, C. L. Kane, and E. J. Mele, Phys. Rev. Lett. **110**, 046404 (2013).
[104] Z. Yan, F. Song, and Z. Wang, Phys. Rev. Lett. **121**, 096803 (2018).
[105] Q. Wang, C.-C. Liu, Y.-M. Lu, and F. Zhang, Phys. Rev. Lett. **121**, 186801 (2018).
[106] R.-X. Zhang, W. S. Cole, and S. Das Sarma, Phys. Rev. Lett. **122**, 187001 (2019).
[107] M. Geier, L. Trifunovic, M. Hoskam, and P. W. Brouwer, Phys. Rev. B **97**, 205135 (2018).
[108] H. D. Scammell, J. Ingham, M. Geier, and T. Li, arXiv:2111.07252.
[109] T. Li, M. Geier, J. Ingham, and H. Scammell, 2D Mater. (to be published).
[110] S. Qin, C. Fang, F.-C. Zhang, and J. Hu, Phys. Rev. X **12**, 011030 (2022).
[111] V. K. Maurya, Shruti, P. Srivastava, and S. Patnaik, Europhys. Lett. **108**, 37010 (2014).
[112] T. Hashimoto, K. Yada, M. Sato, and Y. Tanaka, Phys. Rev. B **92**, 174527 (2015).